VISUALLY LOSSLESS COMPRESSION OF VOLUMETRIC MEDICAL IMAGES

Thesis

Submitted in partial fulfillment of the requirements for the degree of

DOCTOR OF PHILOSOPHY

by

CHANDRIKA B. K.

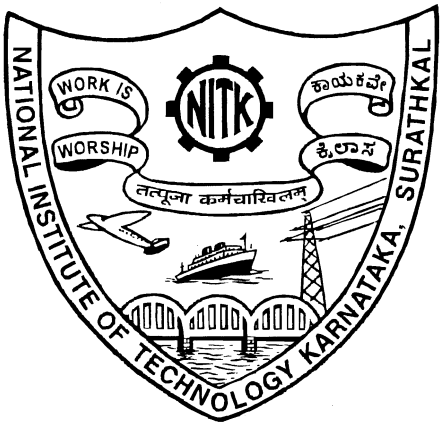

DEPARTMENT OF ELECTRONICS AND COMMUNICATION ENGINEERING,
NATIONAL INSTITUTE OF TECHNOLOGY KARNATAKA,
SURATHKAL, MANGALORE -575025

JUNE, 2016

DECLARATION

I hereby ***declare*** that the Research Thesis entitled **Visually lossless compression of volumetric medical images** which is being submitted to the ***National Institute of Technology Karnataka, Surathkal*** in partial fulfillment of the requirements for the award of the Degree of ***Doctor of Philosophy*** in **Electronics and Communication Engineering** is a ***bona fide report of the research work carried out by me***. The material contained in this thesis has not been submitted to any University or Institution for the award of any degree.

Chandrika B.K.
Register No.: EC11F01
Department of Electronics and Communication Engineering

Place: NITK - Surathkal

Date:

CERTIFICATE

This is to *certify* that the Research Thesis entitled **Visually lossless compression of volumetric medical images**, submitted by **Chandrika B.K.** (Register Number: EC11F01) as the record of the research work carried out by her, is *accepted* as the *Research Thesis submission* in partial fulfillment of the requirements for the award of degree of ***Doctor of Philosophy***.

Prof. Sumam David S.
Research Guide
Professor
Dept. Electronics and Communication Engg.
NITK Surathkal - 575025

Dr. Aparna P.
Research Guide
Assistant Professor
Dept. Electronics and Communication Engg.
NITK Surathkal - 575025

Chairman - DRPC
(Signature with Date and Seal)

This thesis is
dedicated to

my parents, family members and my teachers

ACKNOWLEDGEMENTS

I would like to express sincere and heartfelt gratitude to my research advisor Dr. Sumam David S. for providing consistent support and guidance during my research work. Her timely suggestions and valuable advice enabled the successful completion of this work. Also I express sincere and heartfelt gratitude to my co-research supervisor Dr. Aparna P. for her guidance and support throughout this research work. She has given me good amount of feedback for improving on my work.

I would like to thank Dr. U. Sripati, Head, Department of Electronics and Communication Engineering for the constant support and encouragement. I would always remember with gratitude Dr. Muralidhar Kulkarni, Dr. M. S. Bhat and Dr. Ramesh Kini for their support. My heartfelt thanks to Dr. Deepu Vijayasenan, and Dr. Jayalekshmi RPAC members for their valuable and helpful suggestions. I also take this opportunity to thank all the faculty and staff of E&C department, NITK Surathkal.

My heartfelt gratitude to Dr. Vinod V Thomas, Registrar Evaluation, Manipal University, for encouraging me to pursue this research in the first place and for his constant encouragement. I thank Manipal University for allowing me to come to NITK for pursuing PhD under quality improvement programme. I thank all my friends at NITK and colleagues at MIT Manipal for their support. I would like to thank the supporting staff of the DSP lab Mrs. Prabha, all the non-teaching staff of E&C department and Mrs. Surekha, technical staff at EEE department, MIT Manipal.

I thank Prof Bilgin A., University of Arizona, USA, Dr. Victor Sanchez, University of Warwick, UK, Dr. Tim Bruylants, Vrije University Brussel, Dr. Vijay Ballal, Ampalpady scan center, Udupi and Dr. Mohandas S Bhavikatti, Hubli scan center, Hubli for providing the medical image data sets. I thank Dr. Rajgopal K V, Radiologist, Department of Radio Diagnosis, KMC, Manipal for spending time to view the reconstructed image for quality check. Also I thank Mr Saharsh Oza, of E&C department for helping in my work.

Lastly, and most importantly, I would like to thank my parents, family members and all my teachers, to whom this thesis is dedicated. Their never ending support in all my endeavors has been invaluable.

(Chandrika B.K.)

ABSTRACT

Image compression techniques are broadly classified into two categories. One is lossless or reversible compression and another is lossy or irreversible compression. Lossless or reversible compression techniques are more preferred by medical professionals as every detail that can be perceived by a medical expert is very significant in the diagnosis of any pathological condition. However, lossless methods for compression of medical images don't promise good compression efficiency. On the other hand, a number of lossy methods have been proposed that provide high compression, but at the cost of quality degradation, which is unacceptable by the medical experts. In summary, medical image compression demands for high visual quality, close to that of lossless methods and good compression efficiency close to that of lossy methods. To achieve high visual quality with good compression performance, it is very important to utilize the Human Visual System (HVS) characteristics. Exploiting HVS characteristics guarantees the removal of visually insignificant data without altering any diagnostically significant data. Most of the medical images exhibit bilateral symmetry inherent in the human body. Additional compression can be achieved by exploiting the symmetry if present in images. Further compression can be achieved by means of Volume of Interest (VOI) based hybrid coding. In this method diagnostically important regions in all slices are losslessly coded while the rest of the image is coded using lossy methods. This could be beneficial in the area of tele-medicine with bandwidth limitations.

This thesis proposes five visually lossless compression methods (VLIC-1 to VLIC-5) for 3-D Magnetic Resonance Imaging (MRI) and Computed Tomography (CT) images that embeds Just Noticeable Distortion (JND) profile to remove visually redundant information. The first three algorithms are developed in spatial domain in which background luminance and texture based JND models are used to eliminate perceptually redundant information. The first algorithm is based on predictor and block matching

technique, while second and third algorithms are based on block matching technique. Symmetry nature of human anatomy reflected in medical images is exploited in all the three algorithms. The fourth algorithm is developed in transform domain using wavelets. Along with this, wavelet based vision model is utilized to remove visual redundancies. Final algorithm is a hybrid VOI based method, where in wavelet based visually lossless method is used in diagnostically important regions/volumes and Discrete Cosine Transform (DCT) based lossy technique is used in other regions.

Algorithms are tested on several sets of MRI, CT, x-ray angio images obtained from various sources. Results obtained with 3157 slices of CT images, 886 slices of MR images, 608 slices of x-ray angio slices and 587 slices of MRI brain images with tumor are documented to compare the performance. Compression Ratio (CR) and quality of the encoded images are compared with lossless and lossy algorithms.FEBRAURY HVS based quality metrics are also computed for the above algorithms. The obtained results show better bit per pixel against lossless compression techniques, without any degradation in visual quality. In case of Differential Pulse Code Modulation (DPCM) and symmetry based visually lossless compression technique (VLIC-1), average % reduction in bit per pixel is 11.8 compared to 3D context based Embedded coding of Zerotrees of Wavelet coefficients method (Bilgin *et al.* 1998). In case of symmetry based visually lossless compression technique (VLIC-3) average % reduction in bit per pixel is 6.29 compared to medical image lossless compression method (Ait Aoudia *et al.* 2006). Wavelet based visually lossless coder (VLIC-4) reduces the bit rate by 20.66% compared with DPCM, 28.24% compared with high efficiency video coding (Sanchez and Bartrina-Rapesta 2014), 14.60% compared with Joint Photographic Experts Group (JPEG)-2K, 13.28% compared with JPEG-LS, and 46.85% compared with JPEG-3D (Bruylants *et al.* 2015). The maximum variation in Structural SIMilarity index value for reconstructed images is from 1 to 0.99, indicating they are visually lossless. CR is found to be within the acceptable compression range as suggested by Royal College of Radiologists and European Society of Radiology. The subjective quality of the VOI scheme is validated by radiologist.

TABLE OF CONTENTS

LIST OF TABLES

LIST OF FIGURES

ABBREVIATIONS

CALIC	Context based Adaptive Lossless Image Coder
CR	Compression Ratio
CT	Computed Tomography
CB EZW	Context Based EZW
DICOM	Digital Imaging and Communications in Medicine
DCT	Discrete Cosine Transform
DPCM	Differential Pulse Code Modulation
DR	Digital Radiography
DWT	Discrete Wavelet Transform
EBCOT	Embedded Block Coding with Optimized Truncation
EZW	Embedded coding of Zerotrees of Wavelet coefficients
GAP	Gradient Adjusted Predictor
HEVC	High Efficiency Video Coding
HVS	Human Visual System
IWT	Integer Wavelet Transform
JND	Just Noticeable Distortion
JPEG	Joint Photographic Experts Group
JPEG-LS	Lossless Joint Photographic Experts Group
J2K	Joint Photographic Experts Group-2000
KLT	Karhunen Loeve Transform
MAD	Mean Absolute Difference
MILC	Medical Image Lossless Compression
MRI	Magnetic Resonance Imaging
MSE	Mean Squared Error
NMSE	Normalized Mean Square Error

OECD	Organization for Economic Co-operation and Development
PACS	Picture Archiving and Communication System
PET	Positron Emission Tomography
PSNR	Peak Signal to Noise Ratio
RMSE	Root Mean Square Error
ROC	Receiver Operating Characteristic
ROI	Region Of Interest
SAD	Sum of Absolute Difference
SPECT	Single Photon Emission Computed Tomography
SPIHT	Set Partitioning in Hierarchical Trees
SSIM	Structural SIMilarity index
VIF	Visual Information Fidelity
VLC	Visually Lossless Coder
VLIC	Visually Lossless Image Compression
VOI	Volume of Interest
VSNR	Visual Signal to Noise Ratio

CHAPTER 1

INTRODUCTION

Medical imaging is the non-invasive process of generating the visual picture of inner parts of the human body. Innovations by physicists in the field of medical imaging modalities have made lots of revolution in health care around the world. Advancements in digital signal processing have made it possible to generate digital filmless medical images for diagnosis and surgical planning. Also, evolution in integrated circuit technology and information technology has facilitated improvement in the quality and efficiency of health care systems. Medical imaging represents an increasingly important and indispensable component of modern medical practice, because early and accurate diagnosis can substantially influence patient treatment strategies.

Non-invasive medical imaging technologies such as ultrasound, Magnetic Resonance Imaging (MRI), Computed Tomography (CT), Positron Emission Tomography (PET) and Single Photon Emission Computed Tomography (SPECT) are capable of producing multiple cross-sectional slices of a body with axial, sagittal and coronal views (Ammari 2008). They generate a large volume of digital image data. Such medical images with different resolutions up to 16 bit give the detailed information of the health condition. Moreover, digital images are durable and portable. They can be stored longer time without losing the information since they are immune to external effects such as moisture or heat.

1.1 MOTIVATION

The number of MRI and CT scans performed is continuously increasing year after year throughout the world. The growth in the number of MRI and CT tests carried out per

1,000 population, in selected member countries associated with Organization for Economic Co-operation and Development (OECD), is shown respectively in Figure 1.1 and Figure 1.2 (OECD 2016). So it is apparant that the growing demand for medical image acquisition systems creates the need for efficient storage, archival and transmission of images across health care centers. Therefore compression of medical images is essential.

Advantages of compression of medical image data are two-fold. First one is reduction in image file size, thus accommodating more files in given memory. The second one is the decrease in the time required for transmission of the image file. If one could reduce the file size by 50 %, the transmission time is also theoretically reduced by 50%. Thus compression will save both additional costs for memory and time for transmission.

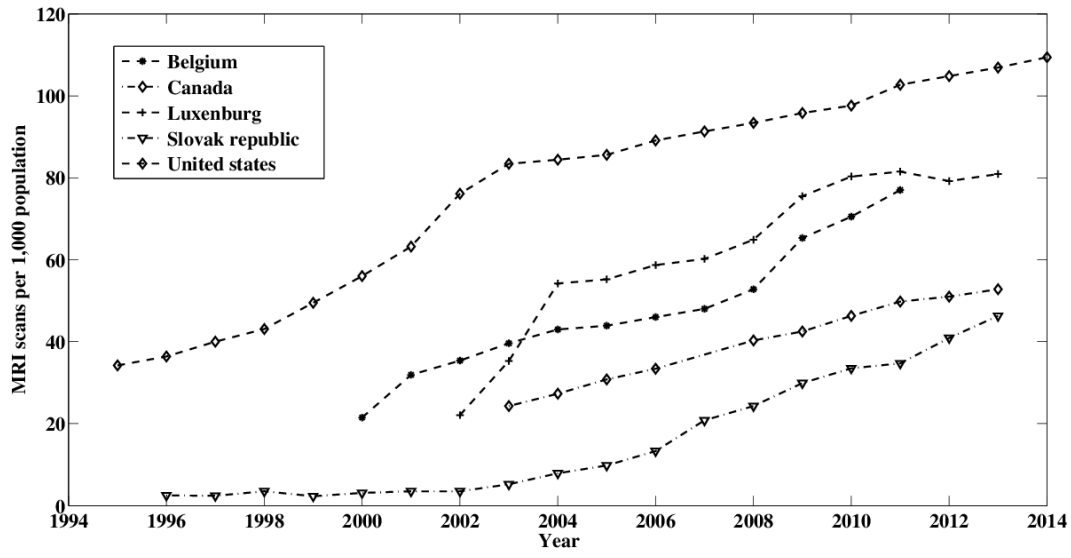

Figure 1.1: Number of MRI tests per 1,000 population in selected OECD countries. The graph is obtained from OECD Health Data, 2016 (OECD 2016).

1.2 BACKGROUND

Image compression techniques are broadly classified into two categories. One is lossless or reversible compression and another is lossy or irreversible compression. Re-

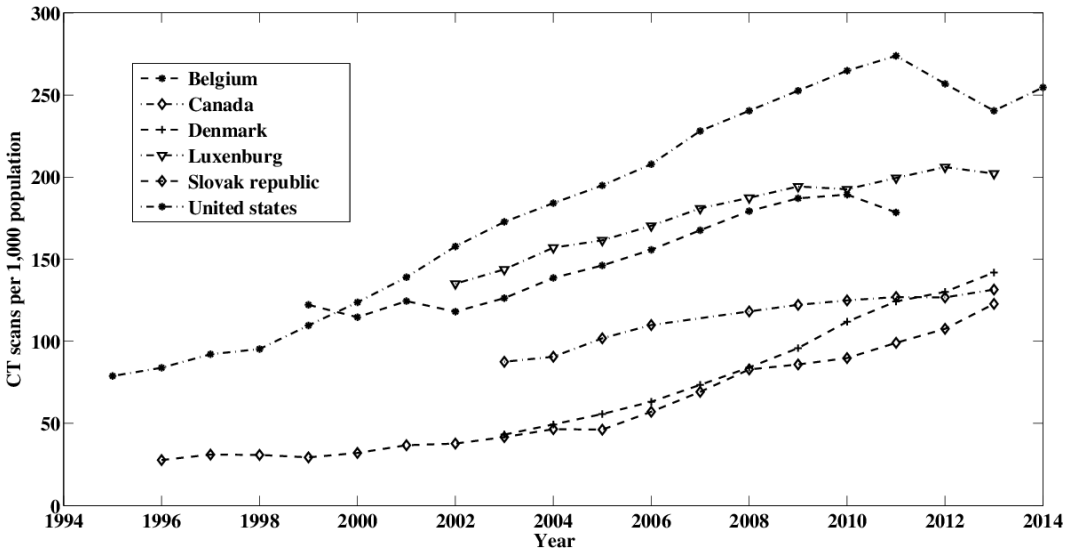

Figure 1.2: Number of CT scans per 1,000 population in selected OECD countries. The graph is obtained from OECD Health Data, 2016 (OECD 2016).

versible compression schemes are more acceptable in the medical field as information is not lost during encoding and decoding operation. But, the available lossless compression techniques can achieve compression ratios only in the range 2:1 to 4:1. This makes the lossless compression techniques unsuitable when data volume is large. In lossy compression, information lost during encoding cannot be recovered. Lossy compression techniques have reported higher compression ratios up to 1:20 without losing diagnostic information. Visible distortions can be minimized by accurately monitoring and controlling the information integrity.

Many compression techniques have been proposed by researchers to compress volumetric medical images. Digital medical imaging techniques became common in the late 1980s, and data compression techniques were also extensively used to compress medical images. Compression algorithms in the early 1990s, assumed that there is no correlation among adjacent image slices and each image slice was compressed independently. In other words, the correlation among adjacent slices (inter-slice correlation), was not exploited. Later compression algorithms used for still images were modified, or new algorithms were developed to exploit inter-slice correlation (Nosratinia *et al.* 1996; Klappenecker *et al.* 1998; Dajun and Chong 2000) to improve the compression ratio.

Lee et al. (Lee *et al.* 1993) developed a coding technique for three-dimensional medical image data sets using displacement estimated inter-frame and block based Discrete Cosine Transform (DCT). In this approach, slice redundancy is exploited, by taking the difference between successive sequences of two-dimensional image slices as there is a small variation between adjacent slices in human body anatomy. Resulting displacement compensated residual image is coded with a block DCT. The performance of the coder is improved, by modeling the distributions of coefficients in difference image to design the quantizer which is optimal for the DCT coefficients. The difference image coefficients are modeled, by Gaussian, Laplacian, and generalized Gaussian probability density function. The improvement in Compression Ratio (CR) with this algorithm is about 5% compared to two-dimensional DCT when slice thickness is 5 mm, and CR is improved by 10% when slice thickness is decreased to 3 mm.

In general, transform coding employs only one transform. Ramaswamy and Mikhael reported that (Ramaswamy and Mikhael 1996) it is possible to improve the performance of the compression algorithm with a mixed transform approach with the fact that all spectral features in an image cannot be represented efficiently with a single transform. In their lossless and lossy compression implementation, the image is resolved first into sub-images such that each sub-image is represented effectively by the dominant components in a certain transform domain. This procedure is followed by representing the entire image with superimposition of different subsets from various domains, which are non-orthogonal to each other. They demonstrated that the combination of Walsh and DCT mixed transform representation is likely to provide higher CR compared to Walsh or DCT alone. By adding residual error (the difference between original signal and reconstructed signal) to quantized and coded coefficients, they extended the lossy technique to a lossless one.

Context-based Adaptive Lossless Image Coder (CALIC) use Gradient Adjusted Predictor (GAP) which is a nonlinear prediction scheme. In GAP, prediction coefficients based on local gradients. By proper modeling of prediction errors and feedback of expected errors, the prediction is made context sensitive and adaptive (Wu and Memon 1996).

Embedded Zerotree Wavelet (EZW) coding was introduced by Shapiro (Shapiro 1993). This algorithm is based on the observation that if the magnitude of a coefficient is smaller than a threshold, then all its descendants are likely to be small. The method of ordering of bits of the wavelet coefficients is efficient for transmission. The extension of EZW method is 3D EZW (Bilgin *et al.* 1998). The performance of 3D EZW is improved to develop context-based EZW (CB EZW) by using context-based adaptive arithmetic coding to exploit dependencies between symbols. Integer Wavelet Transform (IWT) based algorithm presented by Bilgin et al. (Bilgin *et al.* 1998) for 3D medical image compression, use EZW scheme with context-based arithmetic coding. Average CR obtained for 8 bit MRI is 3.81 and that for CT image is 5.81. Ait-Aoudia et al. (Ait Aoudia *et al.* 2006) employed the prediction technique used in lossless compression of video sequences to compress 3D medical image. In this case, CR was found to be better. 4.20 and 6.77 for MRI and CT respectively.

Menegaz et al. (Menegaz and Thiran 2002) developed, a fully 3D object based coding technique to independently decode different objects based on diagnostic relevance in volumetric data. They decorrelated the input data with 3D Discrete Wavelet Transform (DWT), providing a provision for lossless coding. In the coding procedure, different objects are encoded with disjoint segments of the bit stream to independently access and reconstruct the objects up to lossless quality. EZW and multidimensional layered zero coding are used to encode the objects independently. Border artifacts are avoided by encoding additional coefficients.

Tzannes et al. (Tzannes 2003) used Part-2 of Joint Photographic Experts Group (JPEG) 2000 to compress volumetric medical image data sets by exploiting the correlation between adjacent images to achieve better compression than when the images were compressed independently. For lossless compression of 3D data sets, they applied 1D reversible 5/3 wavelet transform across the sequence of 2D image slices in a medical image volume followed by application of JPEG 2000 on resulting transformed slices to improve the compression ratio by 15-18%. For lossy compression of volumetric medical data set they used irreversible 9/7 wavelet transform instead of reversible 5/3 wavelet transform.

Lossy to lossless compression technique provides the option of lossless image decoding or lossy image decoding for quick browsing of the volumetric database. In the case of lossy image decoding, embedded bitstream is truncated. Zixiang Xiong et al. (Xiong *et al.* 2003) applied wavelet transform technique for lossy to lossless compression of 3D medical data. They selected transforms that are unitary to achieve good lossy coding performance. Demonstrated system used a general 3D integer wavelet transform (IWT) frame to approximate a 3D unitary transformation, so that bit plane coding leads to good rate-distortion performance. At the back end, two entropy coding techniques namely, 3D Set Partitioning in Hierarchical Trees (SPIHT) and 3D embedded subband coding with optimal truncation are applied to compress medical volumetric data.

Menegaz et al. (Menegaz and Thiran 2003) focused on the development of a fully 3D wavelet based coding method to enable 3D encoding and 2D decoding functionality. Since fast decoding is of prime importance in medical application for the efficient access to the data, they adopted 2D decoding by encoding every 2D subband image independently. This module allows fast access to 2D image sequences by decoding only the corresponding information, thus avoiding the reconstruction of the entire volume.

T. Vijayaraghavan and K. Rajan also developed an algorithm for fast access to any 2D image (Thirumalai and Kanhirodan 2006). They have used *daub4* filter along x (row) and y (column) directions and Haar filter along the z (slice) direction to exploit inter-slice and intra-slice correlations respectively while using 3D wavelet transform for compression. For easier recognition of coefficients from each subband, they included additional preprocessing stage before wavelet transform.

Schelkens et al. (Schelkens *et al.* 2003) proposed a new compression method which exploits quadtree and block-based coding concepts, layered zero coding principles and context-based arithmetic coding to meet quality and resolution scalability.

Srikanth and Ramakrishnan (Srikanth and Ramakrishnan 2005) considered lossless mesh based inter-frame coding scheme for 3D MRI of brain images. In this scheme, they eliminated clinically insignificant background by meshing only the brain part in the medical image. With the help of spatial edges and optical flow between two consec-

utive slices, they achieved content based (adaptive) mesh generation to avoid multiple motions within each element. Also, they applied context-based entropy coding after motion compensation to exploit the intra-frame and inter-frame correlations. In terms of performance, adaptive mesh based schemes performed marginally better than the uniform mesh-based methods, at the expense of increased complexity.

Although 3D JPEG 2000 exploits the redundancies present in 3D image space, it fails to efficiently recognize the correlation in fourth dimension (time) of 4D data sets. Sanchez et al. (Sanchez *et al.* 2006) proposed an algorithm to compress sequences of three-dimensional medical images captured in time. In the proposed method, standard H.264/AVC video coding based two encoding schemes namely H.264-VOL and H.264-TIME developed for the lossless compression of 4D medical image. Here H.264-VOL is used to exploit the redundancy present among image slices within image volume, whereas H.264-TIME to exploit the redundancies among the sequence of image slices in the time dimension. In H.264-VOL, H.264 is applied along the slice direction to compress each set of volumes of 4D medical image. In H.264-TIME, H.264 is applied along the time direction after selecting all similar image slices across all image volumes. Among the two methods, with H.264-TIME they could achieve 70% improvement in CR.

In Yodchanan (2008), inter-slice correlation is exploited by applying reversible Karhunen Loeve Transform (KLT) to all MRI slices. Spatial redundancy in each KLT slice is removed, with Joint Photographic Experts Group Lossless (JPEG-LS) image coder. Even though inter-slice redundancy can be exploited using 3D context based prediction methods and 3D wavelet transform, they are expensive in terms of computational complexity. Suboptimal approximation of the reversible KLT instead of ordinary reversible KLT is used to reduce the computational complexity involved in calculating the KLT matrices when a large number of slices are present.

Since most of the medical image slices are relatively symmetrical, V. Sanchez et al. (Sanchez *et al.* 2009*b*) implemented a compression algorithm which exploits the anatomical symmetry present in the structure of medical images. They used 2D IWT to decor-

relate the data, an intraband prediction method to reduce the energy of the subbands exploiting the inherent symmetry of the medical image and an embedded block coder to achieve high lossless compression gain, resolution and quality scalability. This algorithm was modified by adding an inter-slice Differential Pulse Code Modulation (DPCM) scheme to identify the correlation between slices (Sanchez *et al.* 2009*a*).

Amraee et al.(Amraee *et al.* 2011) eliminate both intra-slice and inter-slice correlations with block matching routines considering symmetrical characteristics of these images. To eliminate inter-slice correlation, the authors have first predicted the pixels in one-half of the image, using the corresponding pixels in the other half and symmetric nature of the medical image. Successive slices are paired to exploit inter-slice correlations, and the above same method is applied.

Coding scheme presented by Yann Gaudeau et al. (Gaudeau and Moureaux 2009) is based on 3D dyadic wavelet transform and entropy coded code book with lattice vector quantization. The main contribution of their work is the design of a new codebook which takes care of correlations between neighbor voxels. At high compression ratios, it outperforms other methods regarding rate-distortion trade-off.

A novel scalable 3D medical image compression method with Volume of Interest (VOI) coding is proposed by Sanchez et al. (Sanchez *et al.* 2010) for interactive telemedicine applications. This particular compression technique provides random access of VOI as well as resolution and quality scalability to the compressed 3D medical image data with the ability to decode any section of the compressed image without decoding entire data set. They generated a scalable layered bit stream with 3D IWT and Embedded Block Coding with Optimized Truncation (EBCOT).

Sanchez et al. (Sanchez and Nasiopoulos 2011) have extended the above work with channel protection for transmission over error-prone wireless networks to support Picture Archiving and Communication Systems (PACS). PACS used for storage and distribution of 3D medical images, allow quick diagnosis at any time and any place.

Resolution scalability is a desired feature in compression of the medical image. 3D DCT fails to offer lossless coding with quality and resolution scalability. Jonathan

Taquet et al. (Taquet and Labit 2012) proposed a new hierarchical approach to resolution scalable lossless and near lossless compression. Here they combined DPCM schemes with hierarchical oriented predictors to provide resolution scalability.

Pizzolante et al. (Pizzolante and Carpentieri 2013) developed low-complexity compression algorithms for 3D medical images that exploit redundancies present in 3D space using 3D linear prediction and arithmetic coding. In this Medical Images Lossless Compression (MILC) algorithm, for each pixel 3D prediction context is determined to predict the current pixel value. Here CR for MRI is 2.85, and that for CT is 4.48. Sanchez et al. (Sanchez and Bartrina-Rapesta 2014) proposed High Efficiency Video Coding (HEVC) based intra coding for reversible compression of 3-dimensional medical images. Algorithms tested on volume of 8 bit MRI images and 12 bit CT images. CR in the case of MRI is 3.16. CR obtained with CT is 2.38. In 2015, Bruylants et al. (Bruylants *et al.* 2015) presented wavelet based volumetric medical image compression algorithm which supports the volumetric extension of JPEG 2000 standard. CR obtained for both 12 bit MRI, and CT images was 2.69.

An alternative to lossless and lossy compression schemes is visually lossless image coding. The visually lossless compression algorithm gives higher compression gain through the removal of visually redundant information without inducing any perceivable distortions. David Wu et al. (Wu *et al.* 2006) proposed a simple perceptual based compression algorithm to compress MRI, CT and Computed Radiography medical image data sets. They developed an innovative scheme for visual pruning function based on the JPEG 2000 coding structure. The vision model is merged with an improved model of the Human Visual System (HVS) to identify and to remove visually insignificant information.

1.3 OBJECTIVES OF THE THESIS

The majority of the compression algorithms available for medical image data are either lossless or lossy which do not completely fulfill the quality-compression requirement.

Hence there is a need to have an intermediate system with compression efficiency close to that of lossy and quality close to that of the lossless compression system. This can be achieved easily by exploiting HVS characteristics to remove visually insignificant data without loosing any diagnostically significant data. But vision based compression of medical images, is still a major challenge and this thesis attempts to develop image compression algorithms for 3D medical images considering the unique characteristics of medical images and human vision.

Secondly, most of the medical image compression technologies have not explored the spatial redundancies due to symmetry across or within the slices. It has been observed that better compression can be achieved without any loss by exploiting the inherent anatomical bilateral symmetry in the medical images.

Thirdly, most of the medical image compression algorithms do not have an automatic segmentation block to search for ROI/VOI. In medical images diagnostically pertinent area is small. Better compression can be achieved for compression algorithms with ROI/VOI.

With this background, objectives of the thesis can be framed as:

1. To propose and analyze the performance of novel compression algorithm in spatial domain for volumetric medical images, exploiting bilateral symmetric nature of human anatomy retained in the medical images and features of human vision.
2. To propose and analyze the performance of novel compression algorithm in wavelet domain for volumetric medical images, exploiting features of human vision.
3. To develop VOI based compression algorithm for MRI brain images.

1.4 ORGANIZATION OF THE THESIS

In this thesis, five Visually Lossless Image Compression (VLIC) algorithms for volumetric medical images are implemented, and their performance analyzed. Thesis is organized into six chapters.

Chapter 2, provides a brief overview of medical imaging and medical image coding.

Initially, a few of the medical image acquisition techniques used in PACS and Digital Imaging and Communications in Medicine (DICOM) standard are discussed. Further brief review of compression techniques for medical images is given. Also conventional and perceptual based image quality metrics are discussed and the medical image test data sets used to evaluate the algorithms are tabulated.

Chapter 3, presents implementation and analysis of visually lossless coder in the spatial domain. Three distinct algorithms are developed, and in all the three algorithms spatial domain vision model is embedded. In the first algorithm, DPCM and block matching techniques are used, while second and third algorithms are based on block matching technique. A modified vision model is used in the third algorithm. Symmetric nature of human anatomy reflected in medical images is exploited in all the three algorithms. The performance of all the three algorithms is analyzed and compared.

In chapter 4, wavelet based visually lossless coder is presented, and the performance of this algorithm is compared with pixel-based algorithms.

In chapter 5, VOI based coder is presented. Symmetry-based tumor detection technique is used to identify the volume, which is diagnostically important. This volume is coded with wavelet based visually lossless scheme, and the remaining volume in the 3D image is coded with DCT based lossy technique. Objective and subjective evaluations are considered to evaluate the algorithm.

Chapter 6 concludes with the contribution of the thesis. This chapter also presents possible extensions and further work.

CHAPTER 2

MEDICAL IMAGING AND CODING

Evolution in integrated circuit technology and information technology has brought in tremendous improvement in the quality and efficiency of health care systems. In addition to this, digital signal processing has contributed towards the development of medical imaging modalities like MRI, CT, and PET etc., that have a great impact on diagnosis and treatment of various diseases. Early detection and accurate diagnosis of a medical condition calls for improved quality and increase in image resolution, data volume and improved inter-slice distance results in an enormous volume of image data. Analysis and diagnosis requires storage of data. For applications such as tele-medicine and tele-radiology, it is often required to transmit the data over long distance communication channel in shortest possible time. Thus, it is very crucial to compress these huge volume of medical image data for storage and/or transmission.

2.1 INTRODUCTION TO IMAGE COMPRESSION

Image compression, in general, is a process of minimizing the digital image data volume to attain required low bit rate (bit per pixel) for a given image quality. This is generally achieved by eliminating the redundancies in digital image data. Redundancy is the resemblance of symbols or pixel values when they are scanned one after another or close to one another. Most of the image or video compression algorithms are based on the removal of various kinds of redundancies like spatial, temporal and statistical redundancies.

Spatial redundancy represents the similarity between the adjacent pixel values within the image. Natural images have spatial redundancy due to slow variations in the luminance intensity except at the edges. Temporal or slice redundancy is the statistical

interrelation among adjacent pixels of consecutive frames or slices. Statistical redundancy is related to the representation of information. It depends on the entropy of the source (Cover and Thomas 2012) which indicates the minimum number of bits required to represent information.

Image compression algorithms are classified broadly into two groups, information lossless (reversible) and information lossy (irreversible) compression. In reversible compression, information is not lost during encoding and decoding operation. This is an essential requirement in the case of non-invasive medical diagnostic techniques for the detection of abnormalities in a standard clinical procedure. Lossy compression offers higher CR compared to lossless scheme due to quantization of pixel values. Lossy compression is not usually preferred by radiologists and healthcare technology group due to the distortion of clinically critical information.

A general lossy compression algorithm has three functional blocks namely, redundancy reduction, quantization, and coding as shown in Figure 2.1. The base for the quantization of information is to reduce data entropy. Reducing entropy allows more compression. Quantization stage converts a wide range of input values into a limited number of output values. Since it is a many to one mapping, original data cannot be retrieved accurately. Therefore the design of quantizer is critical, and it should selectively quantize the coefficients to preserve the image quality. Quantized values are normally converted into a fixed length binary code. Entropy coding stage reduces the number of bits assigned to each quantized value compared to the number of bits used to represent the original digital information.

A substitute for lossless and lossy coding techniques is VLIC. VLIC provides higher CR compared to lossless algorithms at the same time ensures the visual quality in decoded images. That is, it permits greater compression through the removal of visually redundant information without inducing any perceivable distortion. Here information is quantized in such a way that the observer doesnot perceive distortion introduced in the process of quantization since the human eye is not a perfect sensor. Since visually lossless scheme has higher compression performance and also guarantees the visual quality

in decoded image, this scheme can be an intermediate solution for digital medical image data compression.

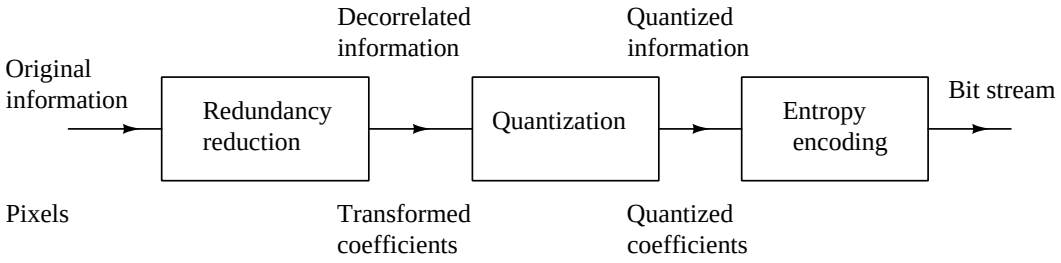

Figure 2.1: General lossy compression scheme

2.2 MEDICAL IMAGING

There have been enormous technological developments in the field of medical imaging after the discovery of x-rays by Roentgen (Rontgen 1896) in 1895. This has made tremendous changes in clinical diagnosis to get critical clinical information without the need for surgery. Also medical imaging-based diagnosis is fast. Modern medical image acquisition systems produce a stack of digital images of different anatomical cross sections for detecting the diseases more accurately throughout the body. Combined with the inventions in digital technology, medical images carrying clinical data can be saved indefinitely, without losing information and can be transmitted or shared in applications like telemedicine and teleradiology. This stimulated the need for a universal standard for the interchange of clinical information.

2.2.1 Medical Image Acquisition Systems

Medical imaging includes the techniques and procedures involved in the generation of images of human body/parts for clinical diagnosis. Even though x-rays were invented a century ago, they are still being used in hospitals. x-ray tests are normally made for the diagnosis of broken bone, dislocation of bone, to examine joint, bone or chest condition and to detect foreign objects. An x-ray source emits a small amount of radiation and is

passed through the organ/bone being examined. An imaging device or x-ray detector captures the x-rays transmitted through the organ/bone. The imaging device may be a photographic plate to generate analog 2D images or detectors that directly capture digital 2D images. A sample of chest x-ray image is shown in Figure 2.2. Among many

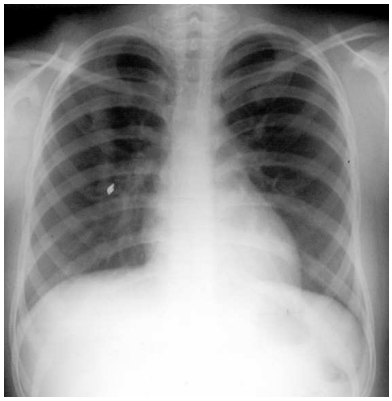

Figure 2.2: An x-ray medical image of the chest (A.J. Chandrasekhar 2016)

modern medical image acquisition systems (Acharya *et al.* 1995), few of the important ones are:

- Computed Tomography
- Magnetic Resonance Imaging
- Ultrasound
- Mammography
- Computed Radiography
- Nuclear Medicine
- Positron Emission Tomography (PET)
- Single Photon Emission Computed Tomography (SPECT)

Among these imaging modalities, x-ray angio, MRI and CT images are used to test the algorithms developed in this thesis.

Computed Tomography (CT):- A basic CT image acquisition system comprises of x-ray source and an image data acquisition system (Acharya *et al.* 1995). Pictorial

representation of a CT scanning unit is shown in Figure 2.3. x-ray source rotates around the patient producing a narrow beam of x-rays. As it passes through a section of the patient body, they are absorbed or attenuated. Detectors present on the opposite side of the x-ray source, register the x-rays exiting the patient body being irradiated as an x-ray snapshot. In one complete rotation of x-ray unit around the patient, many snapshots are taken at different angles. From each rotation of x-ray unit, a cross section image slice of the internal organ is reconstructed with the data collected from each snapshot. Such one cross-sectional image slice is shown in Figure 2.4.

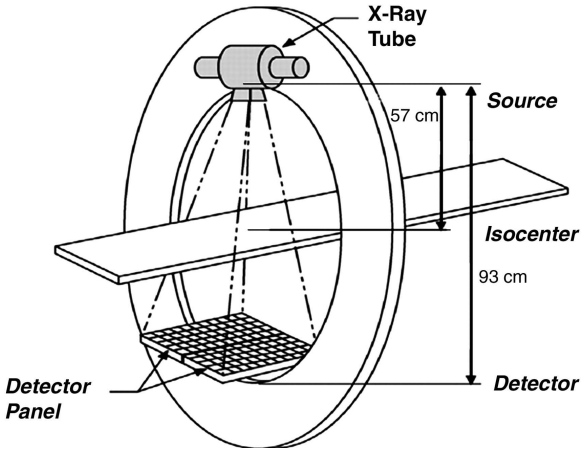

Figure 2.3: CT scanning system (Acharya *et al.* 1995)

Figure 2.4: CT medical image slice from the medical image database (Bruylants *et al.* 2015)

Magnetic Resonance Imaging (MRI): MRI generates image slices of body structure, giving details that help in diagnosis and interpretation of the behavior of the tumor (Hanson 2009). MRI scanner has a powerful main magnet. Electromagnetic waves with a precise resonate frequency, polarizes and excites hydrogen nuclei of water molecules present in human tissue. The resonate frequency is proportionate to the magnetic field enforced (In most of the scanners it is 1.5 Tesla). Another gradient magnet placed within the main magnet is turned ON and OFF to change the main magnetic field. Radio frequency pulses which are perpendicular to the main magnetic field, directed towards tissues under diagnosis, making protons within the hydrogen atoms spin in various directions. When radio frequency pulse is withdrawn, hydrogen atoms come back to their original alignment, emitting energy in the form of radio waves. These radio waves are received by radio frequency antenna and then converted into an image slice.

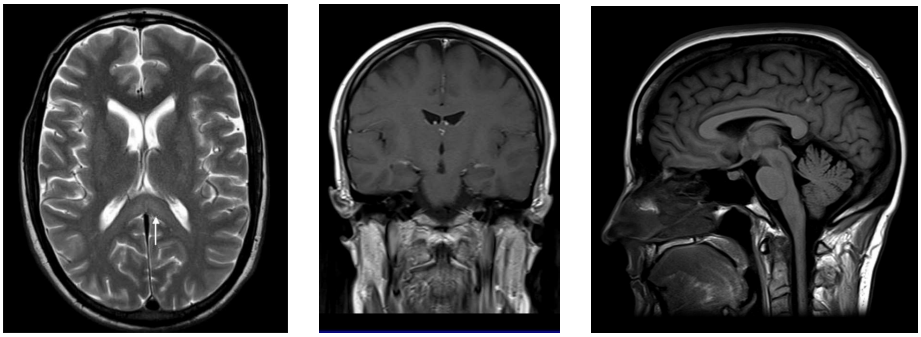

Figure 2.5: Axial, coronal and sagittal view of MRI brain

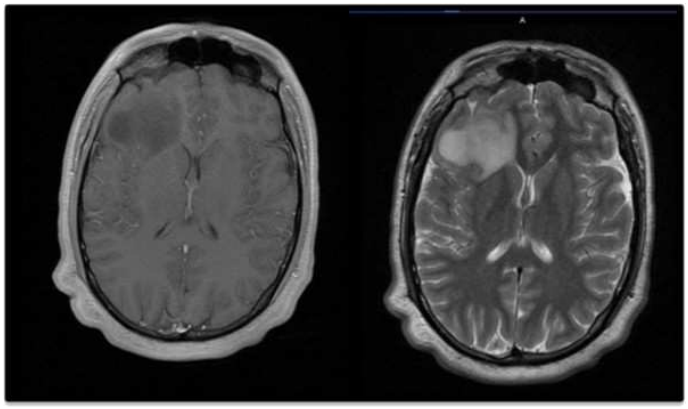

Figure 2.6: T1 and T2 weighted MRI brain images

Axial, coronal and sagittal view of MRI brain images is shown in Figure 2.5. In T1

weighted MRI, white matter is brighter than gray matter, whereas in T2 weighted MRI white matter is darker than gray matter. In MRI, hydrogen protons are signal source. T1 relaxation and T2 relaxation properties contribute to image contrast. The T1 and T2 relaxation times denote the way the protons come back to their original state. T1 and T2 weighted MRI brain image slices are shown in Figure 2.6. In MRI scanning, the patient is not exposed to unsafe radiation. Table 2.1 summarizes different imaging modalities giving details about their imaging features, advantages, and risks. The development from analog film based process to digital multi-slice imaging techniques kindled the need for faster and durable network structure, efficient storage and image management system resulting in the development PACS and DICOM.

2.2.2 PACS and DICOM standard

PACS (Hecht 2008) and teleradiology are two major applications of image compression. PACS is the part of the health-care system to acquire, store, examine and share all types digital images. The major components of PACS system are image acquisition systems, a fast network for distribution of diagnostically critical images, mobile instruments for viewing and processing of the images and efficient storage and retrieving of image systems. This resulted in a need for an universal standard for the exchange of information between different systems involved in health-care management.

DICOM standard: Since noninvasive medical imaging systems have become part of the health-care system, there are many medical image acquisition system manufacturers. A standard format is required for exchange of images produced by different imaging equipment of different manufacturers across and within hospitals. DICOM standard enables easy exchange of medical images independent of imaging equipment manufacturer (Mustra *et al.* 2008). DICOM standard committee develops and maintains an international standard for the exchange of digital medical data generated by different imaging equipment and file formats. A DICOM image file holds image data and a header giving information such as patient name, age, position, dimensions and

Table 2.1: Comparison of imaging modalities (NPS MedicineWise 2016)

Modality	Characteristic		Advantages	Disadvantages
	Main features	Radiation		
x-rays	Imaging of bones, dense matter	x-rays (ionizing)	Quick	Can not pass through bone
PET	Injecting or swallowing a radioactive tracer	Positron (ionizing)	Can distinguish between benign and malignant lesions; can check areas of cancer spread and progress in treatment	Involves exposure to ionizing radiation; radioactive element can be used for limited times
SPECT	Uses a radioactive substance and a special camera to create 3D pictures	Photons (ionizing)	Images free of background, confirm neurodegenerative diseases (Alzheimers, Parkinsons)	Blurring effect is produced
MRI	Uses electromagnetic signals to generate images	Electric & Magnetic fields (Non-ionizing)	Variable thickness; any plane	Lengthy and noisy procedure; Slight movement can ruin the image, requiring retesting
CT	Multiple x-rays to produce cross-sectional layers	x-rays (ionizing)	Can detect presence of more serious problems	Small increased risk of cancer in future
US	High frequency sound waves to produce moving images	Sound waves (Non-ionizing)	Does not require injection of a contrast medium	Quality and interpretation of the image highly depends on the skill of the person doing the scan

type of image. The volume of DICOM images generated per patient per test is huge and are stored in the uncompressed raw data format increasing the storage size. The typical image file features available in DICOM format is given in Table 2.2. Details of image slice size, number of slices per test obtained with different imaging modalities for different organs is tabulated in Table 2.3.

Table 2.2: Typical DICOM image file properties (DICOM Library 2016)

Image modality	Image resolution	bits per pixel
Color flow Doppler	768×576	8
Computed Radiography	3520×4280	12
Digital Radiography	2048×2048	12
Digital Subtraction angiography	512×512	8
CT	512×512	16
MRI	256×256	16
Mammography	4608×5200	14
Ultrasound	512×512	8
X-Ray angiography	512×512	16

Table 2.3: Typical properties of image files obtained with different methods for various organs (Nait-Ali and Cavaro-Menard 2008).

Image modality	Organ	Image resolution	bits per pixel	Number of slices	File size
Radiography	Thorax	2060×2060	16	—-	8 MB
PET	Whole body	128×128	16	350	10 MB
	Heart	128×128	16	47×16 slices *	24 MB
	Brain	256×256	16	47	6 MB
MRI	Brain	512×512	16	20×6 sets *	60 MB
	Abdomen	512×512	16	30	15 MB
	Abdomen 3D	512×512	16	104	50 MB
	Heart	256×256	16	20×20 slices *	50 MB
CT	Brain	512×512	16	300	150 MB
	Abdomen	512×512	16	500	250 MB
	Heart	512×512	16	126×16 slices *	1 GB
US	Standard	512×512	8	50 images/sec	12.5MB/sec
	Doppler	512×512	(RGB) 3×8	50 images/sec	37.5MB/sec

$*$ In the case of heart images, 15-30 slices are taken in one second.

2.3 VOLUMETRIC MEDICAL IMAGE COMPRESSION TECHNIQUES

Medical imaging devices produce numerous image slices in a single medical investigation. Each slice generated represents the separate cross section of the human body being imaged. Hence the increase in image data volume reveal the need for compression techniques with higher CR so that the there is a reduction in storage cost and improvement in transmission rate across low bandwidth channels (e.g. teleradiology applications). Also, fast encoding and decoding algorithms are beneficial to minimize the waiting time of radiologists. This has initiated the development of effective image compression methods.

Any medical image compression technique should have following beneficial properties:

- High lossless CR
- Quality scalability i.e. the capability to construct the compressed image at different image quality
- Resolution scalability i.e. the capability to construct the compressed image data at different resolutions

Compressing image volume with numerous image slices is essential in radiology. One image slice normally represents a cross section of the human body part. Consecutive image slices are also cross sections, which are parallel to the image slice under consideration. Such multiple images generated, normally have structural similarity between one another. It is possible to improve the CR by considering the correlation even between slices instead of compressing images independently.

Coding redundancy is more pertinent to the representation of information. Claude Shannon defined the term entropy (Cover and Thomas, 2006) of the source as the minimum number of bits required to represent information. Efficiently representing information within the limit of entropy corresponds to lossless compression. Although this retains the quality, the amount of compression attained is marginal.

Image coding algorithms achieve compression by exploiting the correlation between neighbouring pixels in 3D space. In most of the techniques, pixel values are initially decorrelated followed by the lossless encoding of resulting data with variable length coders such as arithmetic or Huffman coding. Broadly, decorrelating methods for medical images can be categorized into two classes: intraframe decorrelation and interframe decorrelating methods. Some of the decorrelation techniques are

- Predictive techniques
- Transform methods
- Multiresolution decorrelating methods
- Block match routines

Among various schemes available for lossless compression, predictive methods are simpler and efficient.

2.3.1 Predictive compression techniques

One of the ways to improve the compression performance is by changing the probability spread of the information. Predictive coding is based on this principle. Predictive coding considers the local features of the image. Usually, a predictive coder scans the image in raster scan sequence. Here a pixel value is predicted from the pixels that are already encoded, especially from pixels that are spatially adjacent to the current pixel. If prediction scheme is reasonably accurate, then prediction error generates a probability distribution function which is efficient for entropy coding, thus providing good lossless CR. Let $p(x, y)$ be the selected pixel value and $\hat{p}(x, y)$ is the corresponding predicted pixel value. Then prediction error defined as $e(x, y) = p(x, y) - \hat{p}(x, y)$ is encoded.

Lossless JPEG (JPEG-LS) compression:- Lossless JPEG is an international standard for lossless still image compression (Weinherger *et al.* 2000). Eight different predictor modes are used in lossless JPEG as listed in Table 2.4. In these eight predictor modes, N, W, and NW the causal neighboring pixels of the current pixel $p(x, y)$ as

labelled in Figure 2.7 are used to predict the pixel value. Modes 1, 2 and 3 are one dimensional predictors and modes 4, 5, 6, and 7 are two dimensional predictors.

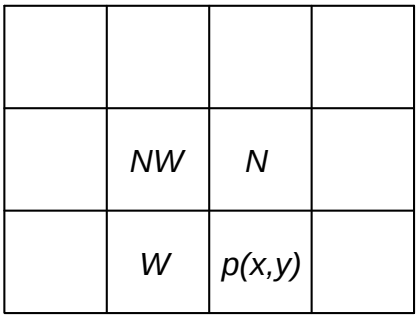

Figure 2.7: Labelling of neighboring pixels

Table 2.4: JPEG predictors for lossless coding

Mode	$\hat{p}(x, y)$
0	0 (No prediction)
1	N
2	W
3	NW
4	$N + W - NW$
5	$N + (N - NW)/2$
6	$N + (W - NW)/2$
7	$(N + W)/2$

To predict the pixel values accurately, each pixel is assigned a context. The context value represents the local gradient, thus representing the type of texture such as smooth region or edge region around the current pixel. Residual values are encoded with Golomb code.

2.3.2 Transform based compression

Components of transform-based encoder and decoder are shown in Figure 2.8. In this, information is transformed from one domain to another, mostly spatial domain to another form of representation to exploit interpixel correlation. Then the decorrelated coefficients are encoded. For the compression of medical images, orthogonal transforms are used so that there is one to one relation between the two domains, and the process is reversible, i.e. entire image can be retrieved by the inverse transform. It facilitates decorrelating the information in the transformed domain, where most of the information is packed in a few coefficients. The rest of the coefficients with very low information can be discarded after quantization.

Various types of transformations used for the compression of medical images are

- Karhunen-Loeve Transform
- Walsh-Hadamard Transform
- Discrete Cosine Transform (DCT)
- Discrete Wavelet Transform (DWT)

Among them, DCT and DWT techniques are discussed in detail.

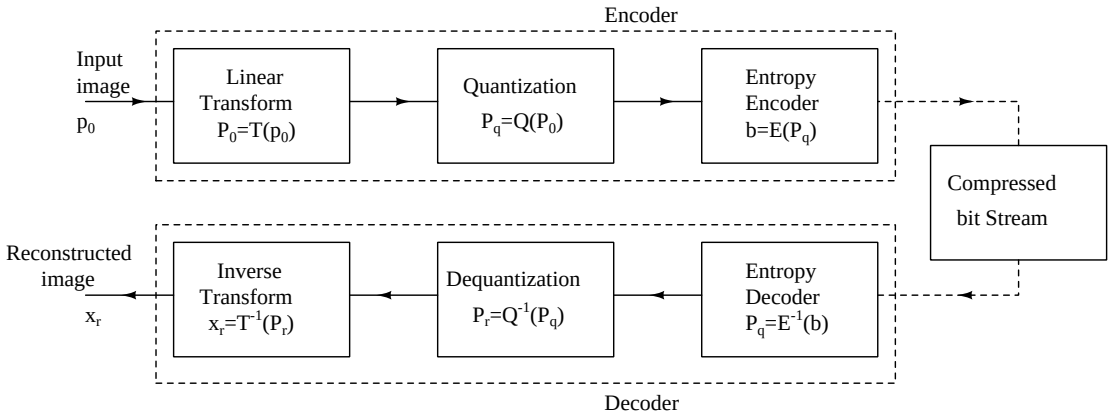

Figure 2.8: Block diagram of transform-based encoder and decoder

Discrete Cosine Transform:- Energy compaction of DCT is better than any other orthogonal transform. DCT transforms the information in spatial domain into frequency domain and is an orthogonal transform. In the case of an image, DCT of the image represents the sum of sinusoids of varying magnitudes and frequencies. Usually, visually relevant information is characterized by a few coefficients of DCT.

2D DCT of an $N \times N$ image is given by

$$P(k,l) = \alpha_k \alpha_l \sum_{x=0}^{N-1} \sum_{y=0}^{N-1} p(x,y) cos\left(\frac{(2x+1)k\pi}{2N}\right) cos\left(\frac{(2y+1)l\pi}{2N}\right) \tag{2.1}$$

where $k, l = 0, 1, ...(N-1)$

Inverse 2D DCT of an $N \times N$ image is given by

$$p(x,y) = \sum_{k=0}^{N-1} \sum_{l=0}^{N-1} \alpha_k \alpha_l P(k,l) cos\left(\frac{(2x+1)k\pi}{2N}\right) cos\left(\frac{(2y+1)l\pi}{2N}\right) \tag{2.2}$$

where $\alpha_k = \alpha_l = \sqrt{\frac{1}{N}}$ for $k = l = 0$ and $\alpha_k = \alpha_l = \sqrt{\frac{2}{N}}$ for $k \neq l \neq 0$.

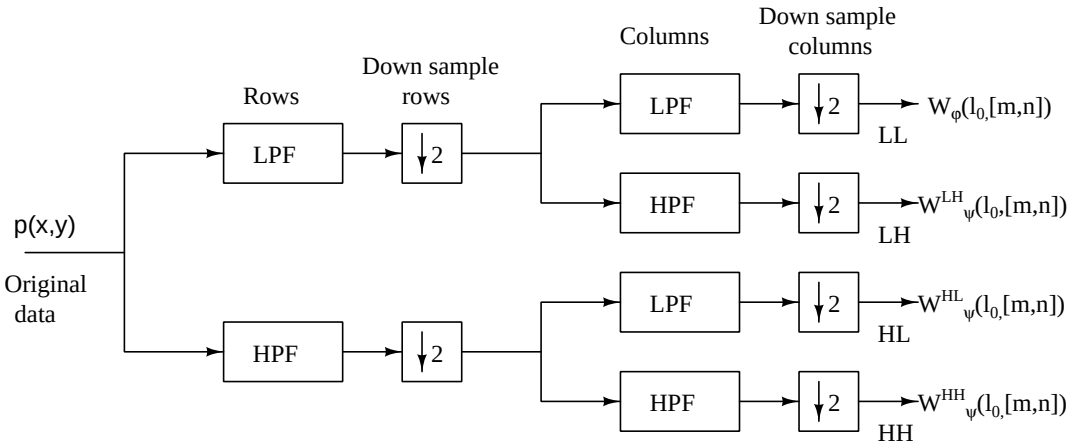

Figure 2.9: Block diagram of 2D DWT with l_0 as a starting scale

Discrete Wavelet Transform:- DWT is also a linear transform that segregates data into different frequency bands. DWT is computed with the set of low pass and high

pass filters followed by subsampling. As DWT has inherent multiresolution quality, they are suitable for medical applications where resolution and quality scalability are necessary. Block diagram of 2D DWT is shown in Figure 2.9. $\downarrow 2$ indicates down sampling. Filter bank method is used to split the image into several frequency bands. Analysis and synthesis bank are the two components of filter bank structure. Analysis bank has low and high pass filters. When the image is passed through the low and high pass filters and down-sampled by a factor of 2, it decomposes into LL, HL, LH and HH bands. L and H denote low pass and high pass filtering respectively. Low pass filter gives approximate coefficient, and high pass filter gives detail coefficient.

DWT of 2D image $p(x, y)$ with resolution of $N \times N$ is given by

$$W_{\varphi}(l_0, [m, n]) = \frac{1}{N} \sum_{x=0}^{N-1} \sum_{y=0}^{N-1} p(x, y) \varphi_{l_0,m,n}(x, y) \tag{2.3}$$

$$W_{\psi}^{i}(l_0, [m, n]) = \frac{1}{N} \sum_{x=0}^{N-1} \sum_{y=0}^{N-1} p(x, y) \psi_{l_0,m,n}^{i}(x, y) \tag{2.4}$$

where $i = HL, LH$ and HH are directional bands. l_0 is starting scale. φ and ψ are expansion functions. $N \times N$ is the number of rows and columns in the 2D image. Equation 2.3 defines the approximated signal, and Equation 2.4 defines the signals with horizontal, vertical and diagonal details for $i = HL, LH$ and HH respectively.

JPEG2000 standard uses DWT. Using DWT, an image can be decomposed into subbands by passing the rows and column of the image through low and high pass filters. The generated structure with one level of decomposition of transform coefficients has four subbands indicated as LL, HL, LH and HH. This procedure is repeated for LL subband to generate multi levels of decomposition. Let l denote the number of DWT decomposition levels, where first levels of decomposition gives four subbands namely LL_1, HL_1, LH_1 and HH_1. The second level decomposition of LL_1 subband generates four more subbands LL_2, HL_2, LH_2 and HH_2 so on as shown in Figure 2.10.

Block diagram of inverse 2D DWT is shown in Figure 2.11. $\uparrow 2$ indicates upsampling. The process of analysis filtering is lossless. It is therefore possible to have a

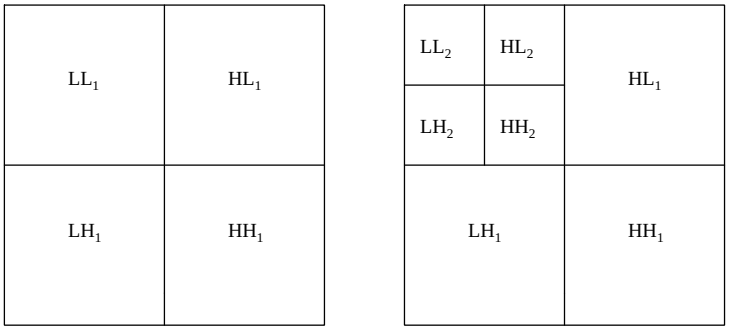

Figure 2.10: First and second level of DWT

perfect reconstruction of the original 2D image by a reverse process of synthesis filtering, as shown in Figure 2.11, which is just the mirror of Figure 2.9. The synthesis filter banks along the rows and columns are associated with upsampling by a factor of two so that the reconstructed image is at the original resolution. The synthesis filter banks therefore perform the IDWT, which is also lossless, like the DWT. 2D image $p(x, y)$ with resolution of $N \times N$ is reconstructed through inverse 2D DWT and is given by

$$\begin{aligned} p(x,y) = &\frac{1}{N}\sum_{m}\sum_{n} W_{\varphi}(l_0,[m,n])\varphi_{l_0,m,n}(x,y) \\ &+\frac{1}{N}\sum_{i}\sum_{l}\sum_{m}\sum_{n} W^{i}_{\psi}(l,[m,n])\psi^{i}_{l,m,n}(x,y) \end{aligned} \tag{2.5}$$

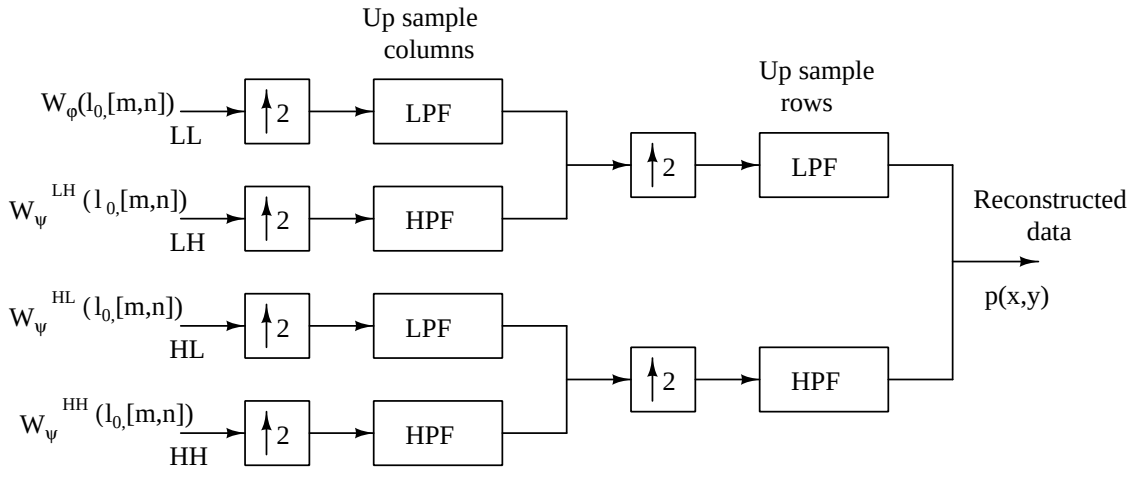

Figure 2.11: Block diagram of 2D inverse DWT with l_0 as a starting scale

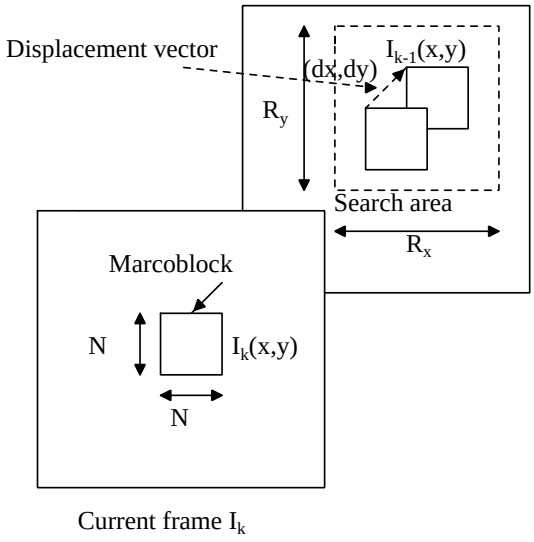

Figure 2.12: Block match algorithm

2.3.3 Block matching algorithm

In the basic temporal prediction technique, previous image slice (reference frame) is used as the predictor for current image slice. A lot of energy is still left out in the residual slice due to the presence of structural correlation between the two slices. Better prediction and hence compression is possible if the similarity between the two slices can be estimated. This technique is called the block matching algorithm.

The current slice is subdivided into nonoverlapping blocks called the macro blocks, and the best match for this block in the reference frame is found as shown in Figure 2.12. Displacement vectors for these blocks are determined after finding the best match in reference image slice defined within the search window. The best match for the macroblock is evaluated based on the matching criteria.

Among the various matching criteria, Mean Squared Error (MSE), Mean Absolute Difference (MAD) and Sum of Absolute Difference (SAD) are the most commonly used. Consider an $N \times N$ macroblock, where $I_k(x, y)$ represent the pixels of the macroblock of current frame and $I_{(k-1)}(x, y)$ represent the pixels of the macroblock of

reference frame. MSE is given by

$$MSE = \frac{1}{N^2} \sum_{x=0}^{N-1} \sum_{y=0}^{N-1} (I_k(x,y) - I_{k-1}(x,y))^2 \tag{2.6}$$

MAD is given by

$$MAD = \frac{1}{N^2} \sum_{x=0}^{N-1} \sum_{y=0}^{N-1} |I_k(x,y) - I_{k-1}(x,y)| \tag{2.7}$$

SAD is given by

$$SAD = \sum_{x=0}^{N-1} \sum_{y=0}^{N-1} \mid I_k(x,y) - I_{k-1}(x,y) \mid \tag{2.8}$$

The macroblock size and the search region size decides the complexity and computational intensity of the process. With smaller block size, approximation is more accurate and hence more will be the displacement vectors that need to be coded. This increases the computation, at the same time increasing the information that has to be delivered to the decoder thus reducing compression. Once the best match for the current macroblock is found in the reference slice, the difference between the two locations gives the displacement vectors. The matching block is identified with this displacement vectors to obtain the predicted block. Now the residual energy between the macroblock and the predicted block is low. This process of block matching routine is simple but computationally intensive.

2.3.4 Region of interest (ROI) based coding

Medical imaging devices produce a large volume of image data per patient for diagnosis and surgical planning which are to be stored for a long time and transmitted within the hospital or across hospitals. The majority of compression techniques available in the literature, compress the entire 2D image. Most of the medical image slices contain large background which are not considered in the diagnosis. Usually, the diagnostically pertinent area is small and need to be compressed losslessly. The remaining area of the

image can be coded with lossy techniques to improve the overall performance of the coding scheme.

Based on this logic ROI based compression approaches were applied on medical images. A medical image with ROI and remaining area is shown in Figure 2.13. In ROI based coding, a medical image slice is segmented into two regions based on clinical importance. They are a region in the image representing the body part or organ and the remaining image region is usually a background with no diagnostic information. The image segmentation process to identify ROI can be manual or automatic. Segmentation can be carried out by identifying regions with different gray level characteristics or texture.

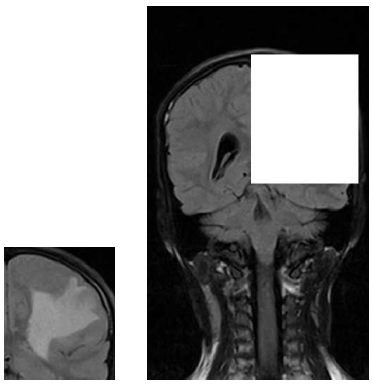

(a) (b)

Figure 2.13: A medical image with ROI and remaining area

ROI based techniques are irreversible. Cosman (Strom and Cosman 1997) developed ROI based coder in which different quality levels were used for different segmented regions through subband compression scheme. Also, more DCT coefficients are used to encode diagnostically important region. In a codebook based technique developed by Andrew (Czihó *et al.* 1998), a large codebook was designed for regions of higher importance, and a smaller codebook was used for lesser important regions. ROI based encoding is also tried by scaling only diagnostically lesser important regions by Skodras (Anastassopoulos and Skodras 2002). Such hybrid techniques give better CR compared to lossless methods. However ROI based techniques are not preferred by radiologists because of complexity, loss of information and problem in correctly recognizing the ROI.

2.3.5 Recommended CR for diagnostic imaging

Compression ratio (CR) is defined as

$$CR = \frac{Bits\ per\ pixel\ of\ the\ original\ image}{Bits\ per\ pixel\ of\ the\ compressed\ image} \tag{2.9}$$

As of now the accepted algorithms for the lossless compression of medical images are DICOM JPEG (ISO 10918-1) and DICOM JPEG-2000 part 1 (ISO/IEC 15444-1). DICOM JPEG is applied for the compression of 8 and 12 bit medical images. DICOM JPEG-2000 Part 1 supports progressive transmission and bit depth compared to DICOM JPEG. At present, this algorithm is considered as a standard for medical applications (Canadian Association of Radiologists June 2008). Clinical evaluation studies on the impact of DICOM JPEG and DICOM JPEG-2000 irreversible compression on medical images generated by various modalities demonstrated that the appropriate use of irreversible CR has no effect on diagnostic accuracy (Canadian Association of Radiologists June 2008), (Koff *et al.* 2009). The recommended CR by Canadian Association of Radiologists for medical imaging modalities such as Computed Radiography / Digital Radiography, CT, US, MRI and Nuclear Medicine after applying irreversible DICOM JPEG and DICOM JPEG-2000 compression are given in Table 2.5 and Table 2.6 respectively.

Recommendations on the use of lossy compression by Royal College of Radiologists (UK) and German Rontgen Society (Germany) for various medical imaging modalities are given in Table 2.7 (Royal College of Radiologists 2016; Loose *et al.* 2009; European Society of Radiology (ESR and others) 2011).

2.3.6 Human vision models for image compression

The physiology of human vision includes eyes, retina, visual pathways and visual cortex. The vision is initiated in eyes. Retina encodes the visual information before transmitting through optical nerve as this channel has a limited capacity. As the number of receptors in the retina and the number of fibers in the optical channel are not same,

Table 2.5: CR for medical imaging modalities with DICOM JPEG compression (Canadian Association of Radiologists June 2008)

Modality	angio-graphy	Breast imaging	Body imaging	Chest imaging	Skeletal imaging	Neuro-radiology	Pediatric imaging
Computed Radiography/ Digital Radiography	—	25:1	30:1	30:1	30:1	—	30:1
CT; slice thickness >5mm	15:1	—	15:1	15:1	15:1	12:1	15:1
CT; slice thickness <5mm	—	—	12:1	12:1	12:1	12:1	—
US	—	12:1	12:1	—	12:1	—	12:1
MRI	24:1	24:1	24:1	24:1	24:1	24:1	24:1
Nuclear Medicine	11:1	11:1	11:1	11:1	11:1	11:1	11:1

Table 2.6: CR for medical imaging modalities with DICOM JPEG-2000 compression (Canadian Association of Radiologists June 2008)

Modality	angio-graphy	Breast imaging	Body imaging	Chest imaging	Skeletal imaging	Neuro-radiology	Pediatric imaging
Computed Radiography/ Digital Radiography	—	25:1	30:1	30:1	20:1	—	30:1
CT; slice thickness >5mm	15:1	—	10:1	15:1	15:1	8:1	15:1
CT; slice thickness <5mm	—	—	12:1	12:1	12:1	12:1	—
US	—	12:1	12:1	—	12:1	—	12:1
MRI	24:1	24:1	24:1	24:1	24:1	24:1	24:1
Nuclear Medicine	11:1	11:1	11:1	11:1	11:1	11:1	11:1

there is compression of information. This is possible because retina can adapt their sensitivity to the input signal. So a wide range of light intensities with some quantization levels can be handled. Hence HVS models developed based on human vision should be incorporated to improve the CR. Vision models identify and measure the redundant perceptual information either in the spatial domain or the transform domain. Vision

Table 2.7: Medically acceptable compression ratios (Royal College of Radiologists 2016; Loose *et al.* 2009; European Society of Radiology (ESR and others) 2011)

Modality	UK	Germany
Radiography - chest	10:1	10:1
Radiography - skeletal	10:1	10:1
Radiography - body	10:1	10:1
Radiography - mammo	20:1	15:1
CT - head	5:1	5:1
CT skeleton/chest/lung	5:1	8:1
MRI	5:1	7:1

models used in our work are discussed in detail in chapter 3 and chapter 4.

2.3.7 Metrics for evaluating compression algorithms

To evaluate lossy compression algorithms objective and subjective metrics are used (Lin and Kuo 2011; Ebrahimi Moghadam and Mohammadi 2015; Engelke and Zepernick 2007). Most of the lossy compression algorithms are evaluated by objective metrics such as Root Mean Square Error (RMSE) (Wang and Bovik 2009) or Normalized Mean Square Error (NMSE) and Peak Signal to Noise Ratio (PSNR), even though many a time they do not correlate well with subjective quality sensed by the HVS. They are defined as:

$$RMSE = \sqrt{\frac{\sum_{x=0}^{N-1}\sum_{y=0}^{N-1}[p(x,y) - g(x,y)]^2}{NXN}} \tag{2.10}$$

$$NMSE = \frac{\sum_{x=0}^{N-1}\sum_{y=0}^{N-1}[p(x,y) - g(x,y)]^2}{\sum_{x=0}^{N-1}\sum_{y=0}^{N-1}[p(x,y)]^2} \tag{2.11}$$

where $p(x, y)$ is the original image pixel, and $g(x, y)$ is the corresponding processed or distorted image pixel.

Subjective measures include Receiver Operating Characteristic (ROC) (Wong *et al.* 1995) analysis. ROC provides a measure of the difference in perceived quality between the original and compressed images. In this analysis, the radiologist reviews a series of compressed diagnostically important images with predetermined CR. For each image, the radiologist gives the confidence rating based on the information provided by the compressed image from their diagnosis on the possibility of the presence of disease. These ratings are compared with the diagnosis made with the original image. A smaller difference in the ratings between the original and the reconstructed image can denote an acceptable level of CR for the image with specified disease. Normally ROC analysis procedure needs several images and many radiologists as observers. Although this procedure is time-consuming and tedious, it is a trusted and accepted method in the medical field to certify the image quality.

Visual Signal to Noise Ratio (VSNR), Visual Information Fidelity (VIF) and Structural SIMilarity index (SSIM) are some of the HVS based quantitative performance metrics available in the literature to assess the quality of the reconstructed medical images (Razaak *et al.* 2014; Kowalik-Urbaniak *et al.* 2015; Al-Ameen and Sulong 2015). The proposed VLIC use VSNR, VIF, SSIM along with PSNR to evaluate the quality of the reconstructed image.

PSNR: Most of the lossy compression codecs use PSNR metric to measure the quality of the reconstructed image. This quality metric is an approximation to visual perception. Therefore in some instances, the reconstructed image with lower PSNR value may look closer to the original than another image with higher PSNR value. The high value of PSNR indicates that there is less difference between the original and processed image. PSNR is defined via the MSE.

For two monochrome images with a resolution of $N \times N$ where $g(x, y)$ is the noisy approximation (or processed image in lossy compression) of original image pixel $p(x, y)$, MSE is given by:

$$MSE = \frac{1}{N^2} \sum_{x=0}^{N-1} \sum_{y=0}^{N-1} [(p(x,y) - g(x,y)]^2 \tag{2.12}$$

PSNR is determined as:

$$PSNR = 10log_{10} \left(\frac{MAX_p^2}{MSE} \right) \tag{2.13}$$

where MAX_p is the maximum possible pixel value in the image.

VSNR: VSNR is a simpler method. VSNR (Chandler and Hemami 2007) calculation involves two stages. In the first stage, image distortion is computed. For this contrast detection threshold is computed with visual masking and visual summation to check for the visibility of distortion in the reconstructed image. If the distortions are below the threshold of detection, the reconstructed image is of perfect visual quality. If the distortions are above the threshold, perceived contrast of the distortions d_{pc} and disruption of global precedence d_{gp} are computed to determine VSNR.
VSNR is defined as:

$$VSNR(p,g) = 20log_{10} \left(\frac{C(p)}{\alpha d_{pc} + (1-\alpha)\frac{d_{gp}}{\sqrt{2}}} \right) \tag{2.14}$$

where $C(p)$ is the contrast of the original image p, $d_{pc} = C(E)$ is the perceived contrast of the distortions, $E = p - g$ is the distortion, d_{gp} is the global precedence and $\alpha \in [0,1]$ determines the relative contribution of d_{pc} and d_{gp}.

SSIM: Bovik and Wang introduced SSIM index (Wang *et al.* 2004). This quality index is based on the assumption that HVS is sensitive to structural information and there is structural dependency among neighbouring pixels in the image. SSIM metric estimates the similarity/difference between two images by combining three components of HVS such as brightness, contrast, and structure. SSIM index between two $N \times N$ images p and g is given by the following expressions (Wang *et al.* 2004):

$$SSIM(p,g) = I(p,g)c(p,g)s(p,g) \tag{2.15}$$

where $I(p,g)$ is luminance component, $c(p,g)$ is the contrast component and $s(p,g)$ is the structural component. So

$$SSIM(p,g) = \left(\frac{2\mu_p\mu_g + C_1}{\mu_p^2 + \mu_g^2 + C_1}\right)\left(\frac{2\sigma_p\sigma_g}{\sigma_p^2 + \sigma_g^2 + C_2}\right)\left(\frac{\sigma_{pg} + 0.5C_2}{\sigma_p\sigma_g + 0.5C_2}\right) \tag{2.16}$$

where μ is the average intensity, σ^2 is the variance and σ_{pg} is the covariance.
Average intensity μ_p of 2D image $p(x,y)$ is given by

$$\mu_p = \frac{1}{N^2}\sum_{x=0}^{N-1}\sum_{y=0}^{N-1} p(x,y) \tag{2.17}$$

Variance σ_p^2 of 2D image $p(x,y)$ is given by

$$\sigma_p^2 = \frac{1}{(N^2-1)}\sum_{x=0}^{N-1}\sum_{y=0}^{N-1}(p(x,y) - \mu_p^2) \tag{2.18}$$

Covariance σ_{pg} is given by

$$\sigma_{pg} = \frac{1}{(N^2-1)}\sum_{x=0}^{N-1}\sum_{y=0}^{N-1}(p(x,y) - \mu_p)(g(x,y) - \mu_g) \tag{2.19}$$

SSIM yields the best performance indicator of image quality, and it gives the closest match to the subjective quality (Kowalik-Urbaniak *et al.* 2014). If images p and g are identical, the value of $SSIM(p,g) = 1$ and if the images are similar to each other, the value of $SSIM(p,g) \approx 1$.

VIF: VIF index is based on nonstructural distortions, unlike SSIM metric. Components considered in the calculation of VIF (Sheikh and Bovik 2006) quality metric are correlation distortion, luminance distortion, and contrast distortion. In this quality estimation, information that can be extracted from the original image is computed. Later loss of same information in the processed (distorted) image is measured.
VIF between two images $p(x,y)$ and $g(x,y)$ is given by

$$VIF(p,g) = \frac{Distorted\ \ image\ \ information}{Reference\ \ image\ \ information} \tag{2.20}$$

VIF value calculated between the original image and its copy is exactly one. For contrast-enhanced images, VIF value is more than one. For blurred or compressed images VIF value lies between 1 and 0.

Range of quality metric: Range of quality metrics discussed are tabulated as shown in Table 2.8.

Table 2.8: Range of quality metrics

Quality index	Range	Value for perfect quality
PSNR (dB)	0 to ∞	∞
VSNR (dB)	0 to ∞	∞
SSIM	0 to 1	1
VIF	0 to 1	1

2.4 MEDICAL IMAGE TEST DATA SETS

In this section, details of medical image test data sets used to evaluate the performance of the algorithms developed in this thesis are given. Table 2.9 lists 176, 8 bit MR image slices and 557, 8 bit CT image slices from Mallinckrodt Institute of Radiology, Image Processing Laboratory (Bilgin *et al.* 1998).

Table 2.9: Details of medical image data set 1 used in the thesis (Bilgin *et al.* 1998)

Volume Number	Image	History	Number of slices	Image data size
1.	CT Skull	Tripod fracture	192	256×256×8
2.	CT Wrist	Healing scaphoid dissection	176	256×256×8
3.	CT Carotid	Internal carotid dissection	64	256×256×8
4.	CT Aperts	Aperts syndrome	96	256×256×8
5.	MRI Liver T1	Normal	48	256×256×8
6.	MRI Liver T2	Normal	48	256×256×8
7.	MRI Sag head	Left exophthalmos	16	256×256×8
8.	MRI Ped chest	Congenital heart disease	64	256×256×8

Table 2.10: Details of medical image data set 2 used in the thesis (Sanchez and Bartrina-Rapesta 2014)

Volume Number	Image	Number of slices	Image data size
1.	x-ray angio-1	151	512×512×12
2.	x-ray angio-2	271	512×512×12
3.	x-ray angio-3	186	512×512×12
4.	CT-1 Human Thorax	596	512×512×12
5.	CT-2 Human Thorax	637	512×512×12
6.	CT-3 Human Thorax	82	512×512×12
7.	MRI Brain	100	256×256×8
8.	MRI Cord	10	512×512×8
9.	MRI Knee	50	512×512×8

Table 2.11: Details of medical image data set 3 used in the thesis (Bruylants *et al.* 2015)

Volume Number	Image	Number of slices	Image data size
1.	CT-1 Lung scan	201	512×512×12
2.	CT-2 Lung scan	242	512×512×12
3.	CT-3 Spiral Arterial scan	75	512×512×12
4.	CT-4 Female cadaver	100	512×512×12
5.	CT-5 Human cadaver	672	512×512×12
6.	CT-6 Chest	44	512×512×12
7.	MRI Brain	250	432×432×12
8.	MRI Brain	200	256×256×12
9.	MRI Brain	100	256×256×12

The second data set used to evaluate the algorithms is listed in Table 2.10 and consists of 608 slices of 12 bit x-ray angio images, 1315 slices of 12 bit CT images and 8 bit 160 slices of MRI (Sanchez and Bartrina-Rapesta 2014). Volumes 1-3 are x-ray images of a vascular study of a human heart. Volumes 4-6 are axial view CT scan images of the human thorax. Volume 7 is axial view MRI scan of human brain and volumes 8-9 is the sagittal view of MRI scan of human spinal cord and knee.

Table 2.12: Details of MRI brain images used in the study

Volume Number	Image	Number of slices	Image data size
1.	Volume-1	100	$256 \times 176 \times 12$
2.	Volume-2	18	$512 \times 304 \times 12$
3.	Volume-3	18	$256 \times 180 \times 12$
4.	Volume-4	47	$256 \times 192 \times 12$
5.	Volume-5	100	$256 \times 168 \times 12$
6.	Volume-6	18	$512 \times 304 \times 12$
7.	Volume-7	18	$512 \times 304 \times 12$
8.	Volume-8	18	$384 \times 210 \times 12$
9.	Volume-9	18	$256 \times 180 \times 12$
10.	Volume-10	19	$256 \times 232 \times 12$
11.	Volume-11	54	$256 \times 168 \times 12$
12.	Volume-12	30	$512 \times 336 \times 12$
13.	Volume-13	18	$512 \times 304 \times 12$
14.	Volume-14	18	$384 \times 210 \times 12$
15.	Volume-15	18	$512 \times 280 \times 12$
16.	Volume-16	18	$512 \times 304 \times 12$
17.	Volume-17	18	$512 \times 360 \times 12$
18.	Volume-18	19	$512 \times 376 \times 12$
19.	Volume-19	20	$384 \times 282 \times 12$
20.	Volume-20	18	$256 \times 256 \times 12$

The third medical image data set is listed in Table 2.11 and consists of 12 bit images generated with CT and MRI scanners (Bruylants *et al.* 2015). This data set has 1334 CT image slices and 550 MRI slices.

Fourth test data set consists of 12 bit T1 and T2 weighted volumetric MRI brain images with tumor obtained from 1.5 Tesla MRI scanner from Hubli scanning center, Hubli, India. Details of these image data sets are summarized in Table 2.12.

2.5 SUMMARY

In this chapter, an overview of medical imaging techniques, in particular, working of CT and MRI are provided. Also, PACS and DICOM standards were included. They facilitate ease saving and transmission of medical images and providing a structure for the exchange of clinical information through images generated from various modalities. Such images generated in health-care systems can be large in volume, demanding the need for image compression. Also, few of the image compression techniques employed in medical image compression are discussed. Various redundancies available in volumetric medical images and the possible way to exploit them to improve the CR of medical images are also discussed. Since the measurement of quality of reconstructed images related to clinical information is very crucial, few of the HVS based image quality metrics is reviewed. Details of medical test data sets used to evaluate the algorithms are listed.

CHAPTER 3

VISUALLY LOSSLESS CODER FOR 3D MEDICAL IMAGES IN PIXEL DOMAIN

A large number of lossless and lossy compression techniques for volumetric medical images have been reported in the literature. They exploit the correlation among adjacent slices and adjacent pixels through prediction techniques, DCT, DWT or block matching techniques. But most of the techniques do not completely utilize the basic symmetry present in medical images. Almost all medical images retain inherent symmetric nature of human anatomy. Sanchez *et al.* (2009*a*); Amraee *et al.* (2011) developed volumetric lossless compression methods based on structural symmetry present in medical images.

In this chapter, three VLIC techniques developed in the spatial domain, for volumetric medical images are discussed. All the algorithms remove visually redundant information present in each image slice. Statistical, as well as structural redundancy present within and across image slices, are also considered to improve the performance. The VLIC algorithm discussed in section 3.1, eliminates redundant visual information through Just Noticeable Distortion (JND) dependent quantizer embedded into DPCM technique. In other two VLIC algorithms discussed in section 3.2, JND dependent quantizer is combined with block match algorithm. All the three approaches discussed in this chapter exploit inherent symmetry feature of medical images.

3.1 DPCM AND SYMMETRY BASED VISUALLY LOSSLESS COMPRESSION

In this section visually lossless compression technique VLIC-1 is proposed for volumetric MRI and CT data. In the proposed method, spatial redundancy present in the image,

symmetric nature of human anatomy and human visual characteristics are considered to compress the volumetric image data. JND profile is also combined with lossless symmetry based medical image compression. DPCM prediction is used to decorrelate the adjacent image pixels. Proposed method uses block matching techniques to reveal inter-slice and intra-slice symmetry based correlations. A simple pixel based JND estimation model is incorporated with DPCM to further improve the compression efficiency. Quantizer in DPCM is dependent on JND value and removes visually insignificant information.

Figure 3.1 shows the block diagram of the proposed method. The important components of the compression system are JND profile estimator, symmetry detector, DPCM predictor, symmetry based inter-slice and intra-slice block matching methods and arithmetic encoding. A detailed explanation of each of these blocks is given in the following subsections.

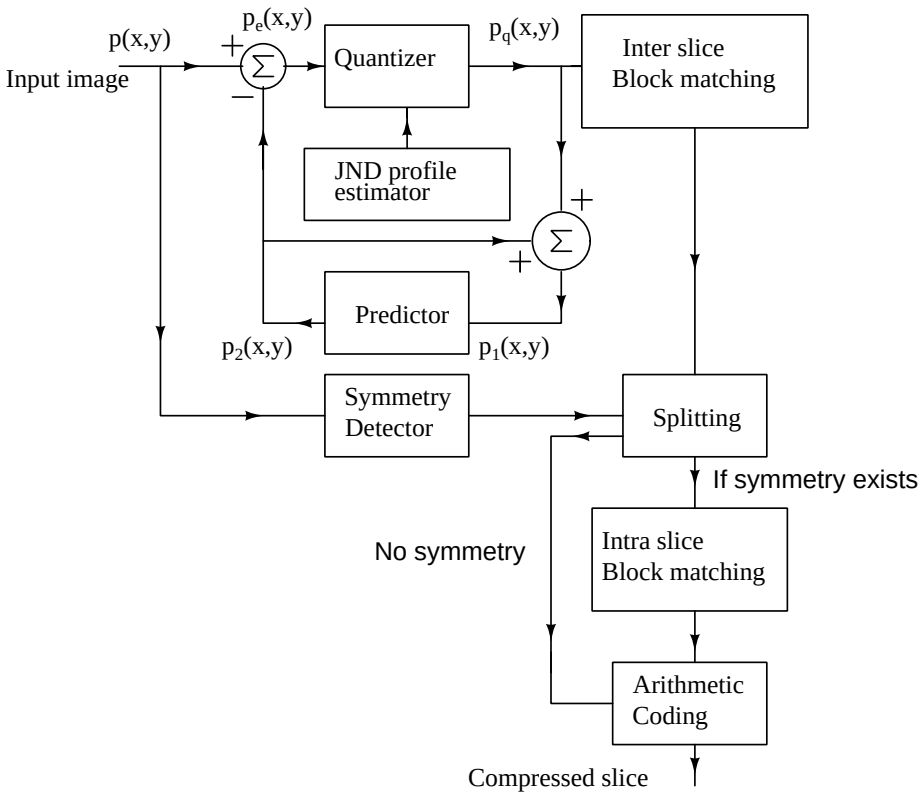

Figure 3.1: Block diagram of the proposed method

3.1.1 DPCM Based predictor

DPCM coding concept is based on the fact that the majority of source signals exhibit significant correlation among adjacent samples. While realizing this basic concept, the current pixel value is predicted based on the previous pixel values to eliminate the redundant information. The difference between actual pixel value and predicted value are encoded to reduce the bit rate. Block diagram of DPCM based encoder is shown in Figure 3.2, where

$p(x, y)$ is the input pixel,
$p_2(x, y)$ is the predicted pixel,
$p_1(x, y)$ is the reconstructed pixel,
$p_e(x, y)$ is the prediction residual,
$p_q(x, y)$ is the quantized prediction residual.

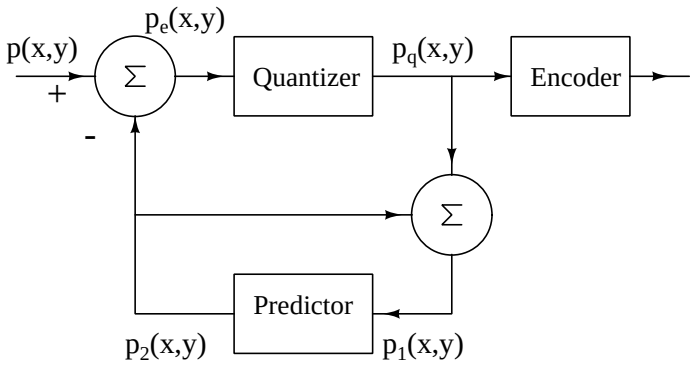

Figure 3.2: Block diagram of DPCM method

DPCM block exploits the spatial correlation. Predicted residual is quantized based on the value of perceptual redundancy present which is provided by JND profile estimator block. Since there is a high magnitude of correlation among adjacent pixels, GAP (Wu and Memon 1996) is applied to each slice of the medical image to decorrelate them. In GAP current pixel value $p(x, y)$ is approximated by the linear combination of

seven neighboring pixels as labelled in Figure 3.3.

Gradient of the intensity function is defined as (Wu and Memon 1996):

$$\begin{cases} d_h(x,y) = |W - WW| + |N - NW| + |NE - N| \\ d_v(x,y) = |W - NW| + |N - NN| + |NE - NNE| \end{cases} \tag{3.1}$$

A prediction is made by the following procedure (Wu and Memon 1996):

Procedure for prediction:

IF $(d_v(x,y) - d_h(x,y) > 80)$ *(sharp horizontal edge)*

$p(x,y) = W;$

ELSE IF $(d_v(x,y) - d_h(x,y) < -80)$ *(sharp vertical edge)*

$p(x,y) = N;$

ELSE $\{$

$p(x,y) = \frac{W+N}{2} + \frac{NE-NW}{4};$

IF $(d_v(x,y) - d_h(x,y) > 32)$ *(horizontal edge)*

$p(x,y) = \frac{p(x,y)+W}{2};$

ELSE IF $(d_v(x,y) - d_h(x,y) > 8)$ *(weak horizontal edge)*

$p(x,y) = \frac{3p(x,y)+W}{4};$

ELSE IF $(d_v(x,y) - d_h(x,y) < -32)$ *(vertical edge)*

$p(x,y) = \frac{p(x,y)+N}{2};$

ELSE IF $(d_v(x,y) - d_h(x,y) < -8)$ *(weak vertical edge)*

$p(x,y) = \frac{3p(x,y)+N}{4};$

$\}$

A sample of original and prediction residual image are shown in Figure 3.4, and the symmetry present in the original image is clearly visible in the residual image.

		NN	NNE
	NW	N	NE
WW	W	p(x,y)	

Figure 3.3: Labelling of neighboring pixels

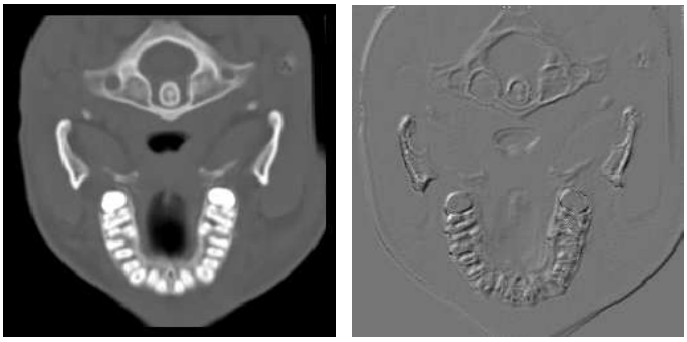

(a) (b)

Figure 3.4: An example of CT skull image:(a) Original image, (b) Predictor residual image

3.1.2 Pixel based JND model

Image compression algorithm should eliminate both spatial redundancies and visually insignificant information from the image data to reconstruct an image of high visual quality with good CR. JND profile is employed to assess the perceptual redundancy by considering features of HVS, and it provides a visibility threshold of distortion for each pixel in an image below which reconstruction errors are unnoticeable. Among the available spatial domain and transform domain JND models in the literature (Nadenau *et al.* 2000), two spatial domain JND models are used in algorithms proposed. Visibility threshold in the first model (JND model-1) is dependent on average background luminance around the pixel and spatial gradient in the background luminance. Visibility threshold in the second model (JND model-2) is dependent on average background luminance, spatial luminance gradient, and texture masking.

JND Model-1

Perceptual redundancies present in images are primarily due to the disparity in sensitivity of the HVS to the differing levels of contrast and luminance variation in the spatial domain. While applying the characteristics of HVS to image coding, the visibility threshold is the most important measure for expressing perceptual redundancy. Visibility threshold of coding deformity is the magnitude of the stimulus at which degradation becomes just visible or just unnoticeable.

The visibility threshold for the grayscale image depends on many factors. Two main factors are average background luminance around the pixel to be encoded and the spatial variations in the background luminance. Regarding the first factor, human visual perception is more sensitive to luminance contrast than the absolute luminance value (Jain 1989). Due to the presence of ambient illumination surrounding the display the distortion in very dark regions tend to be less visible than that present in regions of better luminance.

According to Weber's law, with lower background luminance, the Weber fraction (the ratio of just noticeable luminance difference to stimulus luminance) increases as the background luminance decreases or if the background luminance is high, the Weber fraction remains constant as the background luminance is increased. So high perceptibility threshold are assigned to either very bright or dark areas and low values in regions of medium gray values (Safranek and Johnston 1989). The second factor indicates that the increase in the spatial heterogeneity in the background luminance reduces the visibility of stimuli which is referred as spatial masking. It is computed for every pixel.

In VLIC-1, pixel based perceptual model (Chou and Li 1995) has been selected to measure the perceptual redundancy. This JND model is dependent on two important properties of HVS as specified previously and it evaluates JND value coupled with every pixel of the image from the information in the spatial domain.

Average background luminance $bl(x, y)$ and maximum weighted gradient of average background luminance $w_g(x, y)$ surrounding the pixel $p(x, y)$ are defined as follows:

$$bl(x,y) = \frac{1}{32}\sum_{a=1}^{5}\sum_{b=1}^{5} p(x-3+a, y-3+b)L(a,b) \tag{3.2}$$

$$grad_k(x,y) = \frac{1}{16}\sum_{a=1}^{5}\sum_{b=1}^{5} p(x-3+a, y-3+b)G_k(a,b) \tag{3.3}$$

$$w_g(x,y) = max(|grad_k(x,y)|), \;\; k = 1,2,3,4 \tag{3.4}$$

for $1 \leqslant x < M$ and $1 \leqslant y < N$ where M and N are respectively height and width of the image.

1	1	1	1	1
1	2	2	2	1
1	2	0	2	1
1	2	2	2	1
1	1	1	1	1

Figure 3.5: Operator L for calculating average background luminance

0	0	0	0	0
1	3	8	3	1
0	0	0	0	0
-1	-3	-8	-3	-1
0	0	0	0	0

(a) Operator G_1

0	0	1	0	0
0	8	3	0	0
1	3	0	-3	-1
0	0	-3	-8	0
0	0	-1	0	0

(b) Operator G_2

0	0	1	0	0
0	0	3	8	0
-1	-3	0	3	1
0	-8	-3	0	0
0	0	-1	0	0

(c) Operator G_3

0	1	0	-1	0
0	3	0	-3	0
0	8	0	-8	0
0	3	0	-3	0
0	1	0	-1	0

(d) Operator G_4

Figure 3.6: Operator for calculating the weighted gradient $w_g(x,y)$ in four directions

A weighted low pass operator $L(a,b)$, $a,b = 1,...5$, as given in Figure 3.5 is used to evaluate average background luminance in 5×5 window. The maximum weighted gradient of background luminance $w_g(x,y)$ around the pixel in four directions is found in the same 5×5 window using operator $G_k(a,b)$ as shown in Figure 3.6 for $k = 1,..4$ and $a,b = 1,...5$

Visual model developed from $bl(x,y)$ and $w_g(x,y)$ for the calculation of JND profile is summarized by the following equations (Chou and Li 1995):

$$s_m(bl(x,y), w_g(x,y)) = w_g(x,y)\alpha(bl(x,y)) + \beta(bl(x,y)) \tag{3.5}$$

$$\alpha(bl(x,y)) = 0.0001bl(x,y) + 0.115 \tag{3.6}$$

$$\beta(bl(x,y)) = \lambda - 0.01bl(x,y) \tag{3.7}$$

$$v_{th}(bl(x,y)) = \begin{cases} T_0(1 - (bl(x,y)/127)^{0.5})) + 3 \\ \quad \text{for } bl(x,y) \leq 127 \\ \gamma(bl(x,y) - 127) + 3 \\ \quad \text{for } bl(x,y) > 127 \end{cases} \tag{3.8}$$

$$JND_1(x,y) = max(s_m(bl(x,y), w_g(x,y)), v_{th}(bl(x,y))) \tag{3.9}$$

where $\alpha(bl(x,y))$ and $\beta(bl(x,y))$ are background luminance dependent functions. s_m in equation (3.5) calculates the spatial masking effect. v_{th} in equation (3.8) calculates the visibility threshold due to the background luminance. Maximum value of s_m and v_{th} gives the distortion threshold value $JND_1(x,y)$ in JND model-1 for the pixel at (x,y) position. The constants T_0, γ and λ are taken as 17, $\frac{3}{128}$ and 0.5 respectively (Chou and Li 1995).

3.1.3 Symmetry detection

Symmetry being an inseparable quality of anatomical structure of human body is retained in most of the image slices. Symmetry detector block finds the dominant axis of symmetry if it exists in the image plane. It is carried out by comparing the symmetric pair of feature points (Loy and Eklundh 2006) present in medical image slice. Using scale invariant feature transform (Lowe 2004), a set of feature points a_i are determined, where $a_i = (x_i, y_i, \theta_i)$ describes its location and orientation. First, a descriptor d_i is generated for each feature point and later set of reflected descriptors r_i corresponding to d_i are generated. It is achieved by reflecting the image about x (or y) axis.

Every reflected feature point has equivalent feature point in the current image, and hence r_i is the reflected version of d_i. The best matching points p_j and p_k in the descriptor d_i and the reflected descriptor r_i respectively are then grouped together to form a set of potentially symmetric points. Each pair of matching point p_j and p_k decides a possible symmetry axis. This axis of symmetry passes perpendicularly through the midpoint of the line joining those pair of matching points. If there are many such potential axes of symmetry, one common axis of symmetry is selected as the predominant axis of symmetry. In Figure 3.7 the major axis of symmetry present in one slice of a medical image is illustrated.

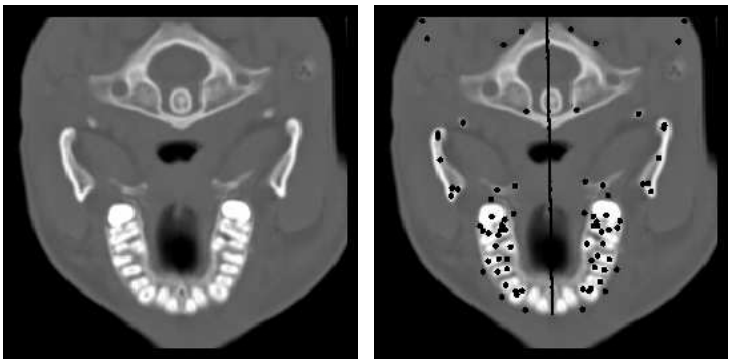

(a) (b)

Figure 3.7: Symmetry detection: (a) Original image, (b) Image with predominant axis of symmetry

3.1.4 Block matching:

Two distinct block matching stages are used in the proposed compression scheme and are discussed below.

Inter-slice block matching

There is a structural correlation between the neighbouring medical image slices because each slice generated is usually a cross section of the human body and is parallel to adjacent slices. CR can be improved by exploring the correlation in the slice direction. The inter-slice block matching is used to estimate the predicted residual image R_i of the current slice using the previous predicted residual image R_{i-1}.

The predicted residual image of current slice R_i is split into non-overlapped blocks of size 8x8. Search window of size 16x16 is defined in the previous predicted residual image R_{i-1}. Since there is a resemblance between the two residual images, there must be the best match for each block in previous predicted residual image. For blocks with all sample values zero, block matching algorithm is not applied. A unique displacement vector is chosen to indicate to the decoder about this particular case while reconstructing the image. Here the blocks with zero values are saved instead of block matching error image.

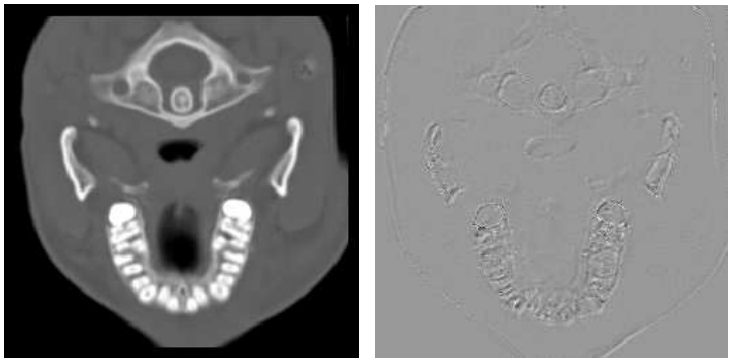

(a) (b)

Figure 3.8: An example of CT skull image: (a) Original CT skull image, (b) Inter-slice block matching error image

A block with minimum SAD is selected as the best match and the corresponding displacement vector, and the block matching error is taken for further processing. A sample of original and inter-slice block matching error image are shown in Figure 3.8.

Intra-slice block matching

If the symmetry detector predicts symmetry in the current image plane, inter-slice block matching error is split along the axis of symmetry. Intra-slice block matching routine is applied on inter-slice block matching error else this step is bypassed. Intra-slice block matching process is performed in the current image plane similar to inter-slice block matching.

3.1.5 Entropy Coding

Arithmetic coding is one of the entropy coding methods used in lossless data compression. In entropy coding, frequently occurring symbols are encoded with fewer bits and not so frequently occurring symbols are encoded with more bits. Huffman code translates each symbol of the message into a series of bits, while arithmetic code overcomes this disadvantage by encoding the entire message into one number. Arithmetic coding tries to evaluate the probability with which certain characters appear and optimizes the length of the code. Another advantage of arithmetic coding over other entropy coders is the convenience of adaptation, i.e. update of probability tables as the data is processed. Hence, context adaptive binary arithmetic coding is used to encode image residuals obtained after applying block matching algorithm.

3.1.6 DPCM based quantizer

DPCM block exploits the spatial correlation. Predicted residual is quantized based on the value of perceptual redundancy present, which is provided by JND profile estimator block. Referring to the block diagram in Fig. 3.1,

$$p_e(x,y) = p(x,y) - p_2(x,y) \tag{3.10}$$

$$p_q(x,y) = Q[p_e(x,y)] = p_e(x,y) - q(x,y) \tag{3.11}$$

where $q(x,y)$ is the quantization error.

$$p_1(x,y) = p_2(x,y) + p_q(x,y) \tag{3.12}$$

and reconstruction error

$$r_e(x,y) = p(x,y) - p_1(x,y) \tag{3.13}$$

The reconstruction error should be within the JND value.

The following procedure is used to quantize the prediction residual value. The $JND_1(x, y)$ value is multiplied by a factor. If the absolute value of prediction residual value $p_e(x, y)$ is lesser than $w_1 * JND_1(x, y)$, $p_e(x, y)$ is multiplied by a factor of q_1. Otherwise it is multiplied another factor q_2. This procedure is repeated for various value of w_1, q_1, and q_2 to get the best possible CR. A JND dependent scheme is developed to quantize the prediction residual by removing visually irrelevant information as:

$$\begin{cases} \text{if } \mid p_e(x,y) \mid \leq w_1 * JND_1(x,y) \\ \qquad p_q(x,y) = q_1 * p_e(x,y) \\ \text{else} \\ \qquad p_q(x,y) = q_2 * p_e(x,y) \end{cases} \tag{3.14}$$

where w_1, q_1 and q_2 are optimally chosen weighting factors.

As mentioned in Equation 3.14, for different weighting factors of w_1, q_1 and q_2, CR and corresponding VIF values are determined. Using different values for the weighting factors of the quantizer w_1 in the range 30 to 60, q_1 in range 0.2 to 0.8 and q_2 in range 0.25 to 0.85. The achieved compression ratio and corresponding VIF was computed for six sets of 3D medical image data. The relationship between CR and VIF for different weighting factors in the case of 3 medical image data sets is shown in Figure 3.9. The value of w_1, q_1 and q_2 for each point Q_n in Figure 3.9 is given in Table 3.1. It can be observed that the optimum set to achieve maximum CR was Q_4 where $w_1 = 50$, $q_1 = 0.6$ and $q_2 = 0.65$

Table 3.1: Range of quantization weighting factors

	w_1	q_1	q_2
Q_1	50	0.2	0.25
Q_2	50	0.2	0.45
Q_3	50	0.5	0.55
Q_4	50	0.6	0.65
Q_5	50	0.7	0.75
Q_6	50	0.8	0.85

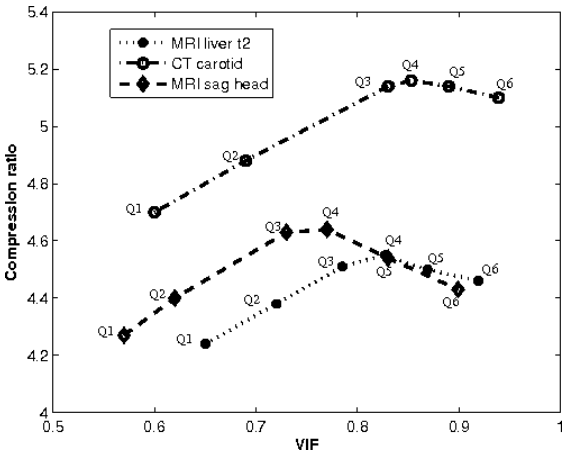

Figure 3.9: Selection of optimum value of quantizer

3.1.7 Simulation results

In this section, simulation result for perceptually lossless CR is compared with the results obtained with lossless methods. Developed algorithm is simulated using Matlab® 8.2 on an Intel® i7 Core processor. The proposed method is tested on four 3D CT data sets and four 3D MRI data sets maintained by Image Processing Lab, Mallinckrodt Institute of Radiology Bilgin *et al.* (1998). The details of these 3D test images are given in Table 2.9 (Medical image data set 1). Information about presence or absence of symmetry in each image has to be supplied to the receiver along with compressed data to reconstruct the compressed image. So CR is calculated as

$$CR = \frac{Bits\ per\ pixel\ of\ the\ original\ image}{S_o + Bits\ per\ pixel\ of\ the\ compressed\ image} \tag{3.15}$$

where S_o is the side information in bits per pixel. Side information is encoded as 8 bits per slice. Also additional six bytes of overhead is required as side information for arithmetic coding.

MSE and PSNR are widely used to evaluate the quality of the reconstructed image, even though they are poor at predicting image quality. Along with PSNR, we have used other two metrics, VSNR (Chandler and Hemami 2007) and VIF (Sheikh and Bovik 2006) which takes into account the properties of HVS to measure the quality of the reconstructed image.

Table 3.2: Comparison of bit per pixel (bpp) of proposed coder VLIC-1 with other lossless compression methods

Image	CALIC	3D EZW	3D CB EZW	VLIC-1
CT Skull	2.725	2.357	2.200	2.028
CT Wrist	1.691	1.394	1.272	1.131
CT Carotid	1.654	1.601	1.527	1.406
CT Aperts	1.047	1.060	0.987	0.903
MRI Liver T1	3.047	2.545	2.398	1.921
MRI Liver T2	2.243	1.944	1.822	1.766
MRI Sag head	2.585	2.322	2.227	1.669
MRI Ped chest	2.810	2.176	2.022	1.742

Table 3.3: Evaluation quality metrics of VLIC-1 with corresponding bit rate

Image	PSNR (dB)	VSNR (dB)	VIF	bit rate
CT Skull	39.10	39.18	0.770	2.028
CT Wrist	47.05	51.69	0.915	1.131
CT Carotid	42.90	45.11	0.853	1.406
CT Aperts	47.45	52.49	0.908	0.903
MRI Liver T1	44.26	45.38	0.875	1.921
MRI Liver T2	39.93	43.80	0.817	1.766
MRI Sag head	40.94	44.22	0.769	1.669
MRI Ped chest	44.02	49.01	0.867	1.742

The obtained bit rates for eight sets of 3D medical images are shown in Table 3.2, and the corresponding evaluation metrics such as PSNR, VSNR, and VIF are given in Table 3.3. Obtained bit rate with VLIC-1 for all image volumes in data set-1 is compared with lossless compression algorithms such as CALIC (Wu and Memon 1996), EZW (Bilgin *et al.* 1998), and CB EZW (Bilgin *et al.* 1998). In the case of lossless technique, reconstructed images will have quality metric PSNR=∞, VSNR=∞, VIF=1, and SSIM=1. As the human eye is not a perfect sensor slight deviation from these ideal values will not be perceived.

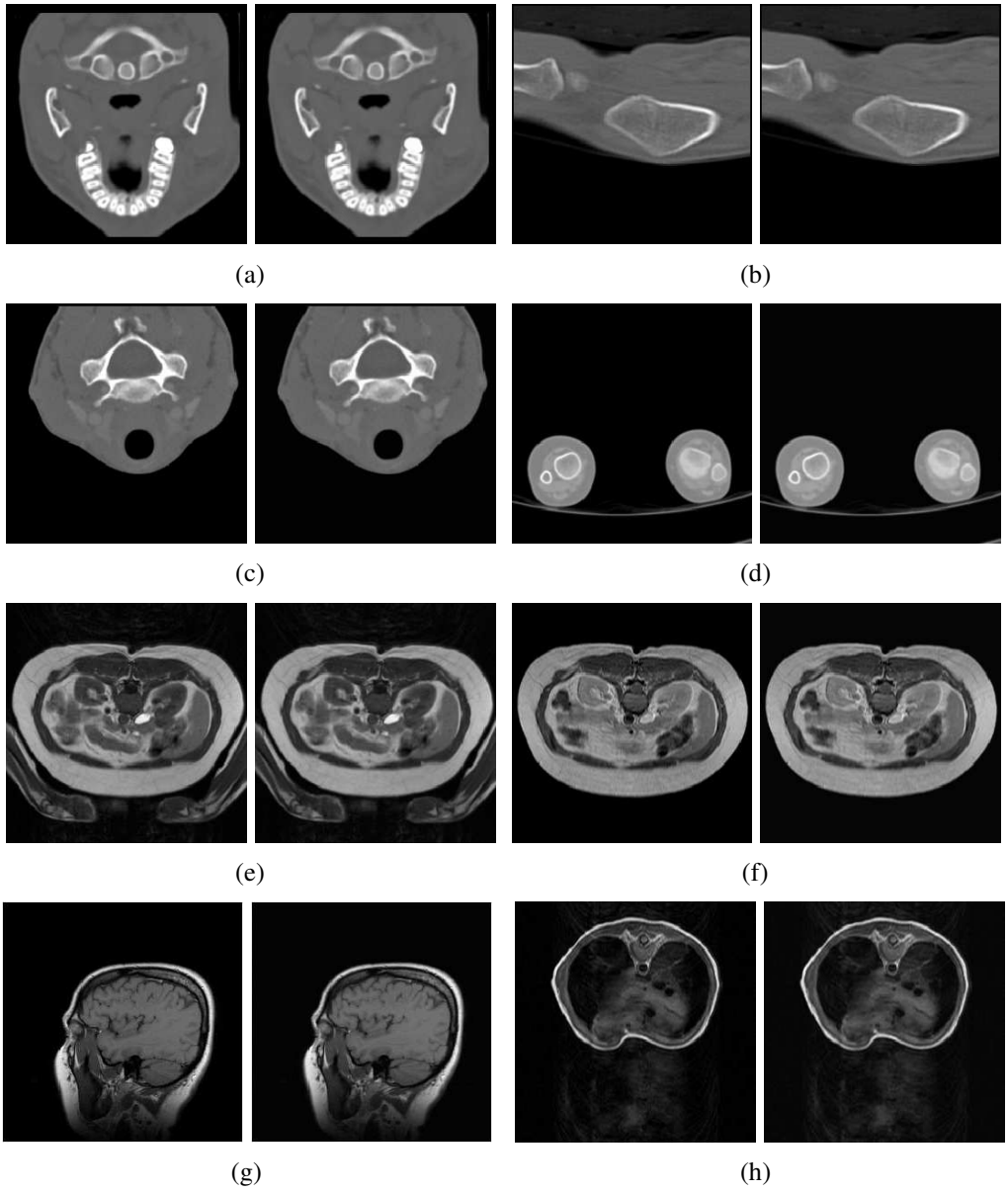

Figure 3.10: Original Image and reconstructed image: (a) CT Skull, (b) CT Wrist, (c) CT Carotid, (d) CT Aperts, (e) MRI Liver T1, (f) MRI Liver T2, (g) MRI Sag head, (h) MRI Ped chest

As these results confirm, the proposed VLIC-1 coder gives improved performance for all eight data sets without any perceivable visual distortion. The average reduction in bit per pixel is 11.8 % with VLIC-1 compared to 3D CB EZW method. A sample of original medical image slice from each of the data sets and corresponding reconstructed image are shown in Figure 3.10.

3.2 SYMMETRY BASED VISUALLY LOSSLESS COMPRESSION

In the proposed symmetry based algorithm, slice redundancy present in the image, symmetric nature of human anatomy and human visual characteristics are considered to compress the volumetric image data. Block diagram of the proposed symmetry based method is illustrated in Figure 3.11. With the symmetry based structure, two different types of visually lossless compression algorithms (VLIC-2 and VLIC-3) are presented in this section. Referring to Figure 3.11, in VLIC-2 algorithm, basic spatial based vision model (JND model-1) is used whereas in the case of VLIC-3, a modified vision model (JND Model-2) is used to measure the visibility threshold. Visibility threshold value is calculated first using spatial domain based JND model for all image slices. Presence of symmetry in each image slice is also determined. Based on the visibility threshold value, perceptually redundant information is removed using quantizer. Block matching is performed on the resulting image slices to remove inter-slice and intra-slice redundancies.

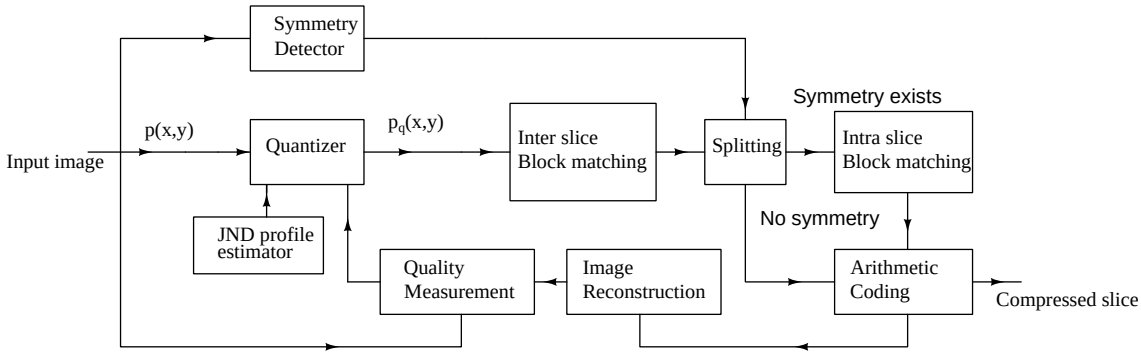

Figure 3.11: Block diagram of the proposed method

3.2.1 JND Model-2

The perceptual model discussed in section 3.1.2 considered only the luminance part in an image to determine JND profile. In this perceptual model, along with effects of luminance adaptation, edge accommodative texture masking in the spatial domain

is also added to better model the HVS characteristic (Yang *et al.* 2005). An increase in the texture heterogeneity in the background will reduce the visibility of distortion and is referred as texture masking. Accordingly, the textured area can mask more deformity than smooth regions. Also, error inserted in edge regions is more prominent compared to non-edge areas since edge texture drags more attention in a classic HVS. So this modified model explores both edge and non-edge regions along with luminance masking and texture masking.

Perceptual model reflecting the above stated factors is expressed as:

$$JND_2(x,y) = v_{th}(bl(x,y)) + t_m(x,y) - C_g \times min(v_{th}(bl(x,y)), t_m(x,y)) \quad (3.16)$$

where $JND_2(x,y)$ is the distortion threshold value in JND model-2 at pixel position (x,y), $v_{th}(bl(x,y))$ is visibility threshold due to background luminance as defined earlier, $t_m(x,y)$ is texture masking and C_g is the gain reduction component due to overlapping effect in masking of two basic masking factors for the gray level image. The value of C_g is set to 0.3.

Texture masking which considers edge information is defined as:

$$t_m(x,y) = \varepsilon w_g(x,y) W(x,y) \quad (3.17)$$

where $w_g(x,y)$ denotes maximum weighted average of background luminance gradient around the pixel at position (x,y). ε is a control parameter and is set as 0.117 (Yang *et al.* 2005). $W(x,y)$ is the edge related weight of the pixel at position (x,y) and it is computed by Canny edge detector followed by a Gaussian low-pass filter as:

$$W(x,y) = E(x,y) * g, \quad (3.18)$$

$E(x,y)$ is edge map of image $p(x,y)$ and is obtained with Canny detector with a threshold of 0.5. g is a 7×7 kernel size Gaussian low pass filter with a standard deviation of 0.8 to remove noise (Canny 1986).

Intra-slice block matching is done on residual data of each slice to improve compression if symmetry is detected in the image slice. The residual image generated by the block matching algorithm and displacement vectors are encoded using arithmetic coding.

3.2.2 Quantizer

Initially, perceptually redundant information is eliminated from the image through JND profile dependent quantizer. Referring to block diagram in Figure 3.11, $p(x, y)$ is the pixel value of input image at position (x, y) and $p_q(x, y)$ the corresponding reconstructed pixel value is given by:

$$p_q(x, y) = q_o \times JND(x, y) \times r(x, y) \tag{3.19}$$

$$r(x, y) = round\left(\frac{p(x, y)}{q_o \times JND(x, y)}\right) \tag{3.20}$$

q_o is quantization weighting factor $0 < q_0 < 1$. $JND(x, y)$ is either $JND_1(x, y)$ or $JND_2(x, y)$. For the first few slices in a data volume, the image slices are reconstructed and the quality of the decoded image slice is measured using VIF to determine the quantization weighting factor q_o as discussed in section 3.3.3.

3.2.3 Implementation

The proposed method has been simulated using Matlab®8.2 on an Intel® i7 Core. Simulation results for the two JND models discussed in section 3.1.2 and section 3.2.1 are evaluated. The algorithm using JND Model-1 is named VLIC-2 and the algorithm using JND Model-2 is named VLIC-3. The MRI and CT data sets have dimensions of 256×256 with 8 bits per pixel. Table 2.9 (Medical image data set 1) gives the details of MRI and CT test image database selected from Mallinckrodt Institute of Radiology, Image processing lab (Bilgin *et al.* 1998).

3.3 RESULTS AND DISCUSSIONS

3.3.1 Compression Efficiency with Modifications in Block Matching Algorithm

Block matching algorithm mentioned in section 3.1.4 is modified to improve the performance of the compression algorithm. Current image slice I_i is split into nonoverlapped blocks of 8×8 and a 16×16 search window is defined in the previous image slice I_{i-1}. Most of the medical images have clinically irrelevant background with pixel values of zero. This particular case is considered to improve the efficiency of the compression algorithm by checking values in 8×8 block. If there is no symmetry in the current image plane and all values within 8×8 block are zero, block match routine is not applied. A unique displacement vector is assigned to inform the decoder about this particular case while reconstructing the image. If all pixel values are not zero in 8×8 blocks, block match routine is applied to search for the best match in the search window.

Minimum SAD value is used to locate the best match. In the case of minimum SAD value is greater than the sum of all pixel values in the current 8×8 block, pixel values in the 8×8 block are saved instead of saving the difference between pixel values in reference window and search window. This particular case is represented by a different displacement vector to assist decoder while reconstructing the image. The same procedure is repeated in the case of intra-slice block matching also.

Simulation results for the lossless compression of all eight test data sets of medical images without including perceptual JND model and quantizer in Figure 3.11 is given in Table 3.4. Column 2 and 4 in Table 3.4 gives the average bit rate after applying only inter-slice block match algorithm without and with modifications in the conventional method. There is a reduction of 10.92% in average bit rate with only inter-slice block matching algorithm. Column 3 and 5 in Table 3.4 gives the average bit rate after applying inter-slice and intra-slice block match without and with modifications in the conventional method. There is an average reduction of 12.18% in average bit rate in lossless compression with modifications in block match routine.

Table 3.4: Bit rates (bpp) of lossless compression algorithm with and without modifications in block match routine

Image	Without modification in block match		With modification in block match	
	Inter-slice block match	Inter-slice & Intra-slice block match	Inter-slice block match	Inter-slice & Intra-slice block match
CT Skull	2.020	1.983	1.783	1.766
CT Wrist	1.370	1.360	1.163	1.152
CT Carotid	2.158	2.112	1.683	1.654
CT Aperts	1.228	1.207	1.035	0.989
MRI Liver T1	2.402	2.391	2.383	2.353
MRI Liver T2	1.946	1.916	1.795	1.794
MRI Sag head	1.894	1.884	1.868	1.775
MRI Ped chest	1.628	1.618	1.645	1.592

3.3.2 Comparison of performance of VLIC-2 and VLIC-3

The efficiency of the VLIC-2 and VLIC-3 coding schemes has been examined by comparing bit rate with that of other 3D lossless compression techniques available in the literature- namely CALIC (Wu and Memon 1996), 3D JPEG (Ait Aoudia *et al.* 2006), 3D EZW (Bilgin *et al.* 1998), 3D CB EZW (Bilgin *et al.* 1998), MILC (Pizzolante and Carpentieri 2013) and VLIC-1. Table 3.5 lists the bit rates of the 8 compression techniques. Comparison of CR of spatial-based VLIC algorithms with lossless techniques is given in Table 3.6. Obtained CR of all the three spatial based VLIC are within the acceptable compression ratios as suggested by Royal College of Radiologists and European Society of Radiology (Table 2.7) for almost all the data volumes. Figure 3.12 shows the percentage reduction in bit rate of the reference method compared to the algorithm yielding the minimum bit rate for each of the test data sets.

The results show that elimination of perceptual redundancy and slice redundancy significantly improves the performance. The proposed methods show better performance than CALIC, EZW, CB EZW, 3D JPEG and MILC for most of the test data sets. The performance of algorithms VLIC-1 to VLIC-3 are dependent on presence of sym-

Table 3.5: Comparison of bit rates (bpp) of VLICs with other lossless compression methods

Image	CALIC	3D EZW	3D CB EZW	3D JPEG	MILC	VLIC-1	VL1C-2	VLIC-3
CT Skull	2.725	2.357	2.200	3.112	2.030	2.028	1.767	1.652
CT Wrist	1.691	1.394	1.272	1.652	1.066	1.131	1.150	1.137
CT Carotid	1.654	1.601	1.527	1.965	1.358	1.406	1.544	1.508
CT Aperts	1.047	1.060	0.987	1.238	0.819	0.903	0.783	0.777
MRI Liver T1	3.047	2.545	2.398	3.125	2.196	1.921	2.286	2.282
MRI Liver T2	2.243	1.944	1.822	2.622	1.759	1.766	1.841	1.791
MRI Sag head	2.585	2.322	2.227	2.758	2.097	1.669	1.572	1.558
MRI Ped chest	2.810	2.176	2.022	2.768	1.655	1.742	1.336	1.336

Table 3.6: Comparison of CR of VLICs with other lossless compression methods

Image	CALIC	3D EZW	3D CB EZW	3D JPEG	MILC	VLIC-1	VL1C-2	VLIC-3
CT Skull	2.935	3.394	3.636	2.570	3.940	3.944	4.527	4.842
CT Wrist	4.730	5.738	6.289	4.842	7.504	7.073	6.956	7.036
CT Carotid	4.836	4.996	5.239	4.071	5.891	5.689	5.181	5.305
CT Aperts	7.640	7.547	8.105	6.462	9.768	8.859	10.217	10.296
MRI Liver T1	2.625	3.143	3.336	2.56	3.642	4.164	3.499	3.505
MRI Liver T2	3.566	4.115	4.390	3.051	4.548	4.530	4.345	4.466
MRI Sag head	3.094	3.445	3.592	2.900	3.814	4.793	5.089	5.134
MRI Ped chest	2.846	3.676	3.956	2.890	4.833	4.592	5.988	5.988

metry in the medical images. The details of slices with structural symmetry in medical data set-1 is given in Table 3.7. It can be observed that VLIC 1 to 3 outperform the other methods for data sets with higher percentage of slices that are symmetric. The bit rate is decreased by 46.44% and 49.06% on average in the case of VLIC-2 and VLIC-3 respectively compared to 2D based CALIC. If one takes the VLIC-2 as the reference for average reduction in percentage bit rate, VLIC-1 yields an almost similar result, since the difference between the two is 2.25%. VLIC-3 and MILC coder provide results with an average difference in the bit rate of 8.12%. The average difference increases up to 19.83% and 63.47% for 3D CB EZW and 3D JPEG coder. Percentage reduction in bit rate with VLIC-3 compared to VLIC-2 is 2.15.

Table 3.7: Slices with bilateral symmetry in data set-1

Volume number	Image	Number of slices with symmetry	Number of slices	% of slices with symmetry
1	CT Skull	188	192	97.71
2	CT Wrist	21	176	11.93
3	CT Carotid	7	64	10.93
4	CT Aperts	37	96	38.54
5	MRI Liver T1	14	48	29.16
6	MRI Liver T2	8	48	16.66
7	MRI Sag head	6	16	37.5
8	MRI Ped chest	24	64	37.5

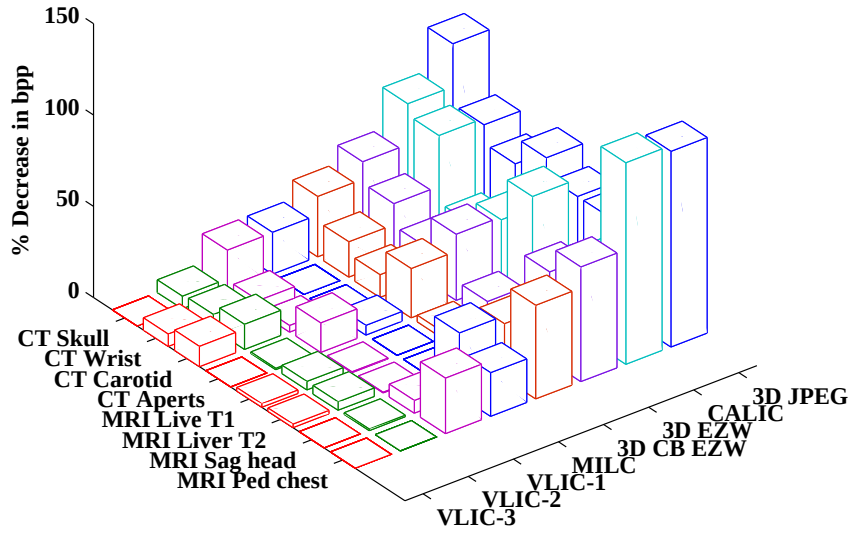

Figure 3.12: Percentage decrease in bit rate with reference method against the algorithm yielding the best bit-rate for each test data set

3.3.3 Quality Metric Based Performances

The algorithm is evaluated for different values of quantization weighting factor q_o ranging from 0.2 to 1 with steps of 0.1. It demonstrates that as the value of q_o increases,

quality of reconstructed image decreases and compression gain increases. Corresponding maximum and minimum value of bit rate and VIF are tabulated in Table 3.8. By measuring the quality of the reconstructed image, value of q_o can be adjusted. Normalized Compression Ratio (CR) and VIF are plotted for a range of q_o values from 0.2 to 1 is shown in Figure 3.13, where normalization/rescaling of CR or VIF is carried out with the equation:

$$x_{new} = \frac{x - x_{min}}{x_{max} - x_{min}} \tag{3.21}$$

Table 3.8: Bit rate and VIF for minimum and maximum value of q_o ($q_o = 0.2$ and $q_o = 1$)

Image set	VLIC-2				VLIC-3			
	bpp_{max}	bpp_{min}	VIF_{max}	VIF_{min}	bpp_{max}	bpp_{min}	VIF_{max}	VIF_{min}
CT Skull	1.8131	1.7311	0.9750	0.8498	1.7652	1.6121	0.9811	0.8824
CT Wrist	1.2294	1.1339	0.9598	0.8192	1.1586	1.1112	0.9600	0.7986
CT Carotid	1.7382	1.3294	0.9881	0.8776	1.7362	1.2973	0.9900	0.8903
CT Aperts	0.8810	0.8056	0.9757	0.8719	0.8777	0.7984	0.9770	0.8771
MRI Liver T1	2.3992	2.2752	0.9537	0.7789	2.4006	2.2658	0.9539	0.7825
MRI Liver T2	1.9894	1.7907	0.9800	0.8679	1.9483	1.7625	0.9866	0.8852
MRI Sag head	1.6166	1.5339	0.9281	0.7331	1.6223	1.5414	0.9287	0.7137
MRI Ped chest	1.5076	1.1476	0.9540	0.6350	1.5110	1.1431	0.9540	0.6365

As the value of q_o increases, CR increases and VIF decreases. Nearest value of q_o where CR and VIF curves meet is considered as the best value to get both good bit rate and visual quality. The optimal value of q_o is found to be 0.5 for all data sets except for MRI Ped chest, to have good bit rate and visual quality as shown in Figure 3.13. For MRI Ped chest which is a more noisy image the optimal value of q_o is 0.4 as shown in Figure 3.13. Hence while compressing the medical images, optimal quantization weighting factor of $q_o = 0.5$ is chosen, in the case of noisy images $q_o = 0.4$ is used.

Quality of reconstructed image is measured with PSNR, VSNR, VIF and SSIM metrics. The evaluation metrics for the reconstruction quality such as PSNR, VSNR, VIF and SSIM with corresponding bit rate are given in Table 3.9. SSIM yields the best performance indicator of image quality, and it gives the closest match to the subjective

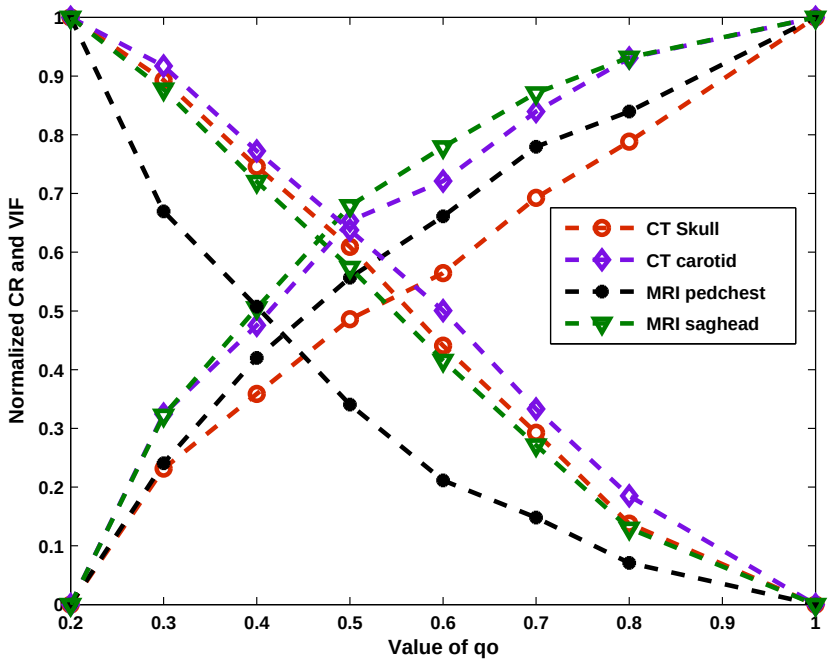

(a)

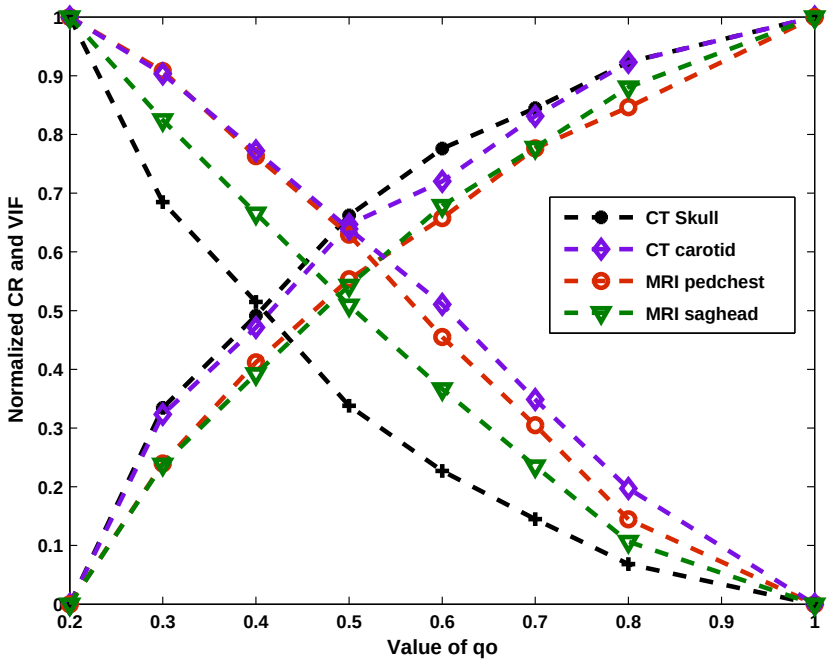

(b)

Figure 3.13: Selection of q_o: (a) VLIC-2 compression technique (b) VLIC-3 compression technique

Table 3.9: Quality metrics of reconstructed image for optimal q_o

Image set	VLIC-2					VLIC-3				
	PSNR (dB)	VSNR (dB)	VIF	SSIM	bit rate	PSNR (dB)	VSNR (dB)	VIF	SSIM	bit rate
CT Skull	50.15	46.29	0.9426	1	1.767	51.42	47.94	0.9565	1	1.652
CT Wrist	48.98	53.53	0.9145	1	1.150	49.05	53.56	0.9169	1	1.137
CT Carotid	52.89	50.88	0.9700	1	1.544	53.46	50.89	0.9710	1	1.508
CT Aperts	52.14	56.37	0.9481	0.9994	0.783	52.28	56.42	0.9503	0.9994	0.777
MRI Liver T1	42.64	46.69	0.8927	0.9947	2.286	42.67	46.69	0.8937	0.9947	2.282
MRI Liver T2	50.53	46.98	0.9508	1	1.841	51.20	47.04	0.9597	1	1.791
MRI Sag head	46.39	55.32	0.8543	1	1.572	46.42	55.35	0.8550	1	1.575
MRI Ped chest	43.30	54.29	0.8334	0.9914	1.336	43.32	54.28	0.8337	0.9914	1.336

Table 3.10: Comparison of PSNR obtained with JPEG-2K Part 1, JPEG-2K Part 2, VLIC-2 and VLIC-3

Image set	J2K-P1		J2K-P2		VLIC-2		VLIC-3	
	bpp	PSNR (dB)	bpp	PSNR (dB)	bpp	PSNR (dB)	bpp	PSNR (dB)
CT Skull	1.664	49.17	1.684	49.17	1.654	50.87	1.648	50.59
CT Wrist	1.261	53.78	1.281	52.89	1.229	52.93	1.224	53.01
CT Carotid	1.702	55.99	1.707	55.97	1.7384	58.23	1.736	59.24
CT Aperts	0.914	56.85	0.901	56.97	0.881	56.50	0.877	56.62
MRI Liver T1	1.957	49.20	1.977	49.30	2.399	47.23	2.400	47.28
MRI Liver T2	2.240	55.96	2.260	55.84	1.790	55.12	1.762	55.89
MRI Sag head	1.590	48.23	1.592	48.86	1.616	50.13	1.622	50.15
MRI Ped chest	1.559	48.46	1.579	48.52	1.507	48.66	1.511	48.68

quality (Kowalik-Urbaniak *et al.* 2014). As these results confirm, the proposed method gives the improved performance on most of the data sets without any perceivable visual distortion.

Also, the performance of the algorithms is compared with lossy state-of-the-art coders like JPEG2000 Part 1 and JPEG2000 Part 2. Kakadu 7.4 version software is used for the implementation of JPEG-2KP1 and JPEG-2KP2 (KAKADU 2016). The rate-distortion values for each of the dataset and the methods is given in Table 3.10, Table 3.11 and Table 3.12. From the values in the table, it is clearly seen that VLIC-2

Table 3.11: Comparison of SSIM obtained with JPEG-2K Part 1, JPEG-2K Part 2, VLIC-2 and VLIC-3

Image set	J2K-P1		J2K-P2		VLIC-2		VLIC-3	
	bpp	SSIM	bpp	SSIM	bpp	SSIM	bpp	SSIM
CT Skull	1.664	0.99001	1.684	0.99002	1.654	1	1.648	1
CT Wrist	1.261	0.9977	1.281	0.9976	1.229	1	1.224	1
CT Carotid	1.702	0.9976	1.707	0.9986	1.7384	1	1.736	1
CT Aperts	0.914	0.9963	0.901	0.9970	0.881	1	0.877	1
MRI Liver T1	1.957	0.9926	1.977	0.9937	2.399	1	2.400	1
MRI Liver T2	2.240	0.9988	2.260	0.9979	1.790	1	1.762	1
MRI Sag head	1.590	0.9967	1.592	0.9983	1.616	1	1.622	1
MRI Ped chest	1.559	0.9918	1.579	0.9918	1.507	1	1.511	1

Table 3.12: Comparison of VIF obtained with JPEG-2K Part 1, JPEG-2K Part 2, VLIC-2 and VLIC-3

Image set	J2K-P1		J2K-P2		VLIC-2		VLIC-3	
	bpp	VIF	bpp	VIF	bpp	VIF	bpp	VIF
CT Skull	1.664	0.9151	1.684	0.9151	1.654	0.9405	1.648	0.9489
CT Wrist	1.261	0.9704	1.281	0.99703	1.229	0.9767	1.224	0.9825
CT Carotid	1.702	0.9780	1.707	0.9784	1.7384	0.9881	1.736	0.99
CT Aperts	0.914	0.9784	0.901	0.9792	0.881	0.9757	0.877	0.9770
MRI Liver T1	1.957	0.9528	1.977	0.9535	2.399	0.9537	2.400	0.9539
MRI Liver T2	2.240	0.9863	2.260	0.9841	1.790	0.98	1.762	0.9866
MRI Sag head	1.590	0.9199	1.592	0.9207	1.616	0.9281	1.622	0.9287
MRI Ped chest	1.559	0.9170	1.579	0.9170	1.507	0.954	1.511	0.9540

and VLIC-3 give a better quality either at nearly same or lower bit rates. Table 3.11 and Table 3.12 show that the quality of the reconstructed image of our coder has better quality in terms of HVS metrics without any perceivable visual distortion.

A sample of original medical image slice from each data sets and corresponding reconstructed image with VLIC-2 and VLIC-3 compression techniques are shown in Figure 3.14 and Figure 3.15 respectively.

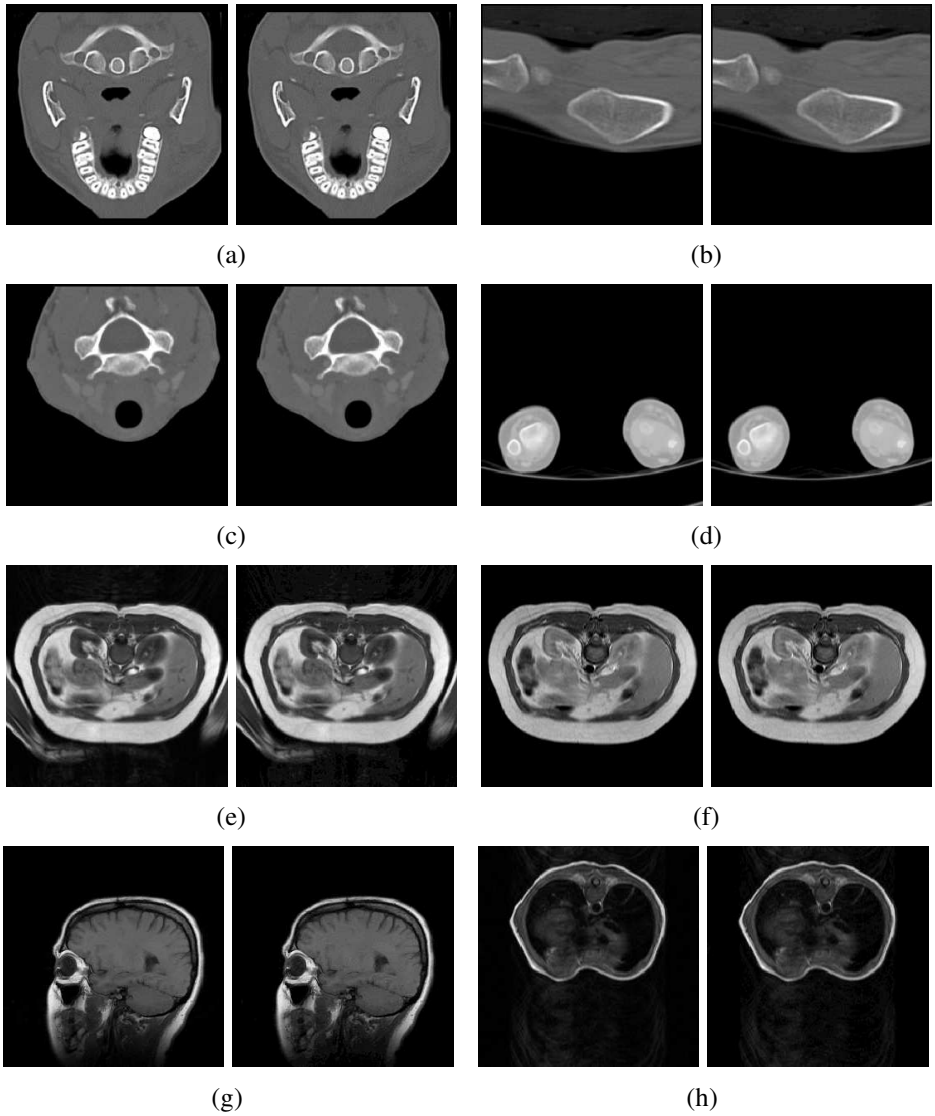

Figure 3.14: Visual clip of original and reconstructed images with VLIC-2 compression technique (Slice number of image is 12).
(a) CT Skull: original; Reconstructed image (PSNR=49.20 dB)
(b) CT Wrist: original; Reconstructed image (PSNR=48.90 dB)
(c) CT Carotid: original; Reconstructed image (PSNR=53.14 dB)
(d) CT Aperts: original; Reconstructed image (PSNR=53.82 dB)
(e) MRI Liver T1: original; Reconstructed image (PSNR=42.66 dB)
(f) MRI Liver T2: original; Reconstructed image (PSNR=50.65 dB)
(g) MRI Sag head: original; Reconstructed image (PSNR=46.39 dB)
(h) MRI Ped chest: original; Reconstructed image (PSNR=43.33 dB)

3.3.4 Analysis of impact of adding various blocks in VLIC-3 coder

Block diagram of lossless and visually lossless compression technique without symmetry and with symmetry are shown in Figure 3.16, Figure 3.17, Figure 3.18 and Fig-

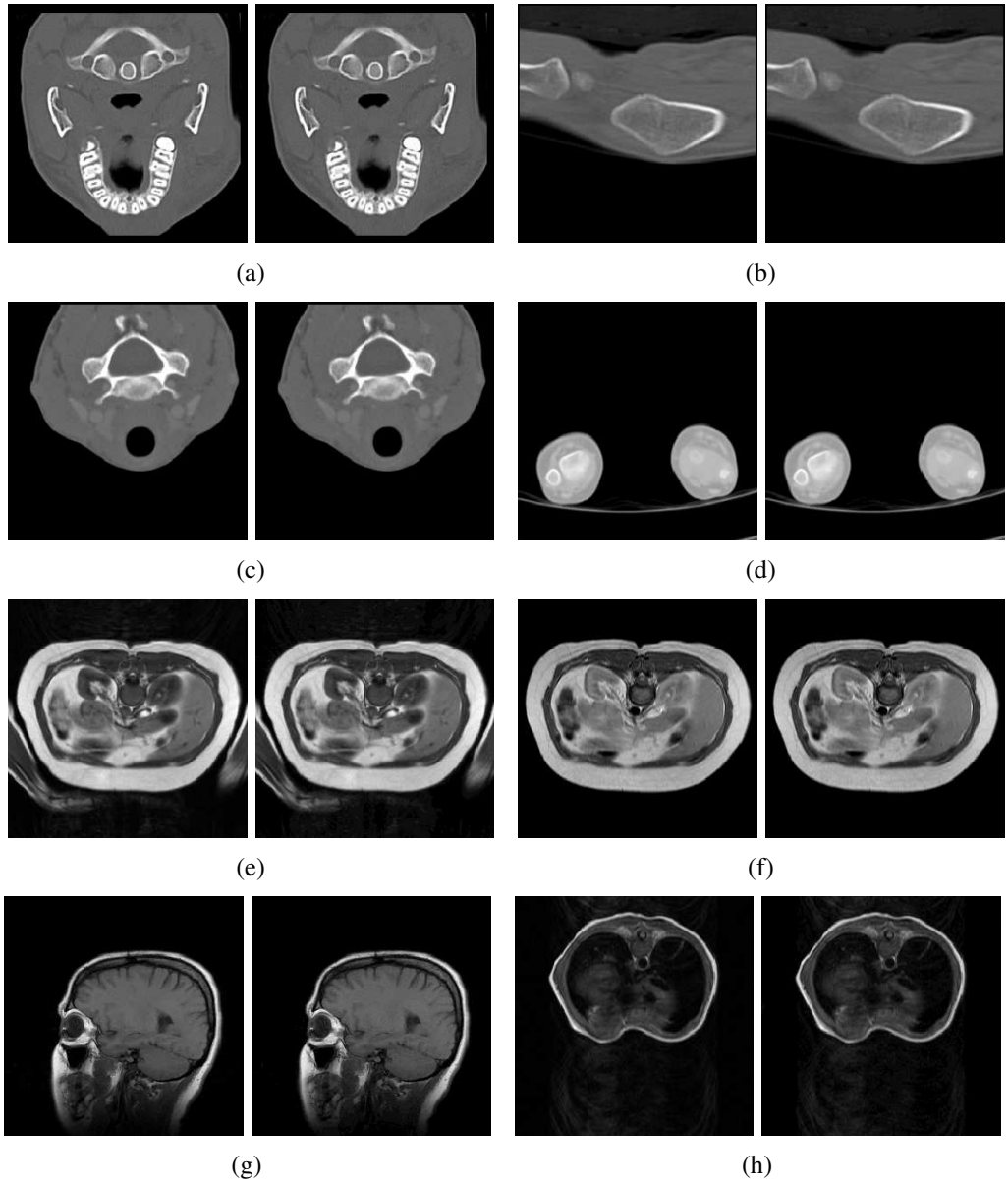

Figure 3.15: Visual clip of original and reconstructed images with VLIC-3 compression technique (Slice number of image is 12).
(a) CT Skull: original; Reconstructed image (PSNR=51.12 dB)
(b) CT Wrist: original; Reconstructed image (PSNR=48.99 dB)
(c) CT Carotid: original; Reconstructed image (PSNR=53.81 dB)
(d) CT Aperts: original; Reconstructed image (PSNR=53.97 dB)
(e) MRI Liver T1: original; Reconstructed image (PSNR=42.69 dB)
(f) MRI Liver T2: original; Reconstructed image (PSNR=51.31 dB)
(g) MRI Sag head: original; Reconstructed image (PSNR=46.41 dB)
(h) MRI Ped chest: original; Reconstructed image (PSNR=43.54 dB)

ure 3.19. JND model-2 is used to identify the redundant visual information.

Basic lossless coding system shown in Figure 3.16 removes inter-slice redundancy

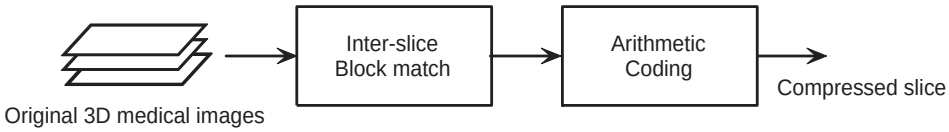

Figure 3.16: Block diagram of lossless image coder (Coder-1).

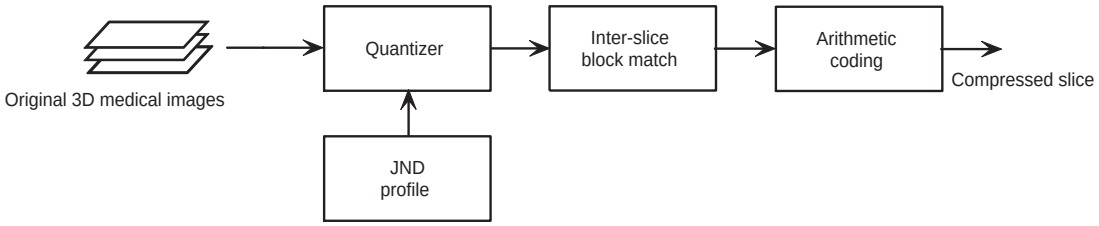

Figure 3.17: Block diagram of visually lossless image coder (Coder-2).

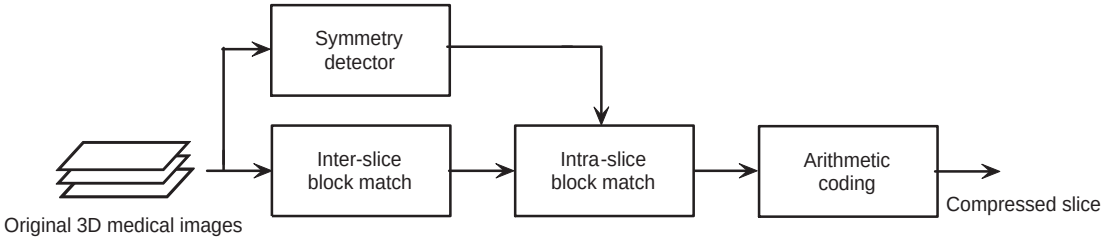

Figure 3.18: Block diagram of lossless image coder with symmetry (Coder-3).

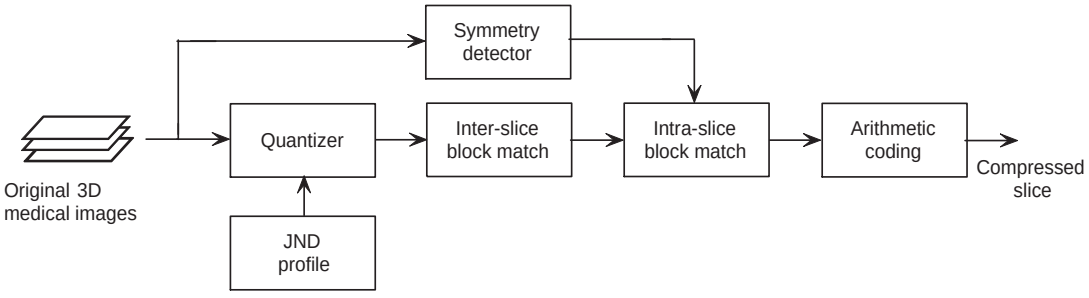

Figure 3.19: Block diagram of visually lossless image coder with symmetry (Coder-4).

using block matching routine. To remove the redundancy within the image slice due to the symmetric structural feature of medical images symmetry detector and intra-slice block matching blocks are added as shown in Figure 3.18. JND model-2 block is added to basic compression system to implement basic VLIC technique as shown

in Figure 3.17. Figure 3.19 is the basic VLIC technique with symmetry detector and intra-slice block matching blocks.

Table 3.13 tabulates the bit rates obtained for each of the coders as shown in Figure 3.16, Figure 3.18, Figure 3.17 and Figure 3.19. Basic lossless compression method (Coder-1) removes only the redundancy between slices of volumetric medical data. The achieved lower bit rate in the case of symmetry based lossless compression (Coder-2) compared to basic lossless technique is due to the removal of intra-slice redundancy.

Table 3.13: Bit per pixel (bpp) of volumetric image compression algorithms

Image	Coder-1 Figure 3.16	Coder-3 Figure 3.18	Coder-2 Figure 3.17	Coder-4 Figure 3.19
CT Skull	1.783	1.766	1.728	1.652
CT Carotid	1.683	1.654	1.601	1.508
MRI Liver T1	2.383	2.353	2.310	2.282
MRI Liver T2	1.795	1.794	1.792	1.791
MRI Ped chest	1.645	1.592	1.386	1.336

Even though symmetry property of medical images is not considered in the case of Coder-2, compression efficiency is better than lossless methods (Coder-1 and Coder-3) due to improved quantization of pixel values. Degradation in the perceivable visual quality is avoided by using a JND dependent quantizer, instead of the uniform quantizer. JND model decides the amount of distortion that can be introduced at each pixel position of each image slice. Symmetry-based visually lossless algorithm (Coder-4) gives the best performance among all the four techniques since it considers symmetry based redundancy, redundancy between slices and perceptual redundancy. Results obtained are compared among different cases as follows:

Case-1: Lossless compression without and with symmetry:- Bit rate is reduced by 1.76% on an average in the case of lossless compression with symmetry compared to lossless compression without symmetry.

Case-2: Visually lossless compression without and with symmetry:- Obtained percentage reduction in bit per pixel is 2.88% on an average in the case of visually lossless compression with symmetry compared to visually lossless compression without symmetry.

Case-3: Lossless and visually lossless compression without symmetry:- An average 7.37% reduction in bit rate is observed in the case of visually lossless compression without symmetry compared to lossless compression without symmetry.

Case-4: Lossless and visually lossless compression with symmetry:- Maximum reduction in bit rate is obtained as symmetry based visually lossless compression method exploits static, symmetry and perceptual redundancies. The bit rate is reduced by 8.47% on an average in the case of visually lossless compression with symmetry compared to lossless compression with symmetry.

3.4 SUMMARY

This chapter, introduced three types of VLC (VLIC-1, VLIC-2, VLIC-3) exploiting symmetry characteristic present in medical images and characteristics of human vision system. The compression methods developed use pixel based visual model. JND model is embedded into symmetry based lossless compression technique to identify, measure and eliminate the visually redundant information. JND model-1 is dependent on background luminance, and JND model-2 is dependent on background luminance and edge accommodative texture masking. VLIC-1 is based on DPCM and symmetry based algorithm. JND model-1 is embedded in DPCM. In VLIC-2, JND model-1 is used to identify the redundant visual information and JND model-2 is used in VLIC-3 algorithm. VLIC-3 algorithm proves to be efficient compared to VLIC-2. Proposed visually lossless coders are tested on standard medical data sets and compression performance is compared with lossless compression techniques.

The proposed methods show better performance when compared to CALIC, EZW, CB EZW, 3D JPEG and MILC for most of the test data sets. The bit rate is decreased

by 46.44% and 49.06% on average in the case of VLIC-2 and VLIC-3 respectively compared to 2D based CALIC. The performance of VLIC-1 and VLIC-2 is almost similar. VLIC-3 and MILC coder provide results with an average difference in the bit rate of 8.12%. The average difference increases up to 19.83% and 63.47% for 3D CB EZW and 3D JPEG coder. Percentage reduction in bit rate with VLIC-3 compared to VLIC-2 is 2.15. The reduction in bit rate is 8.47% on an average in the case of visually lossless compression with symmetry compared to lossless compression with symmetry. HVS based quality metrics are used to measure the quality of the reconstructed image.

All the three algorithms discussed in chapter 3, are developed in the spatial domain. The spatial domain based vision models are used to remove visually irrelevant information. Spatial based compression techniques fail to decorrelate and identify high frequency contents present in the image. Hence, a wavelet based compression algorithm is proposed in chapter 4 to improve the performance.

CHAPTER 4

WAVELET BASED VISUALLY LOSSLESS COMPRESSION OF MEDICAL IMAGES

The wavelet transform is a novel computational based multi-resolution analysis tool used to decompose complex signals. It is capable of conveying detailed spatial and temporal information. DICOM standard which is used in the field of medical imaging supports wavelet based JPEG 2000. Wavelet based compression techniques provide superior rate-distortion performance for three-dimensional medical data sets. Also, it supports resolution scalability and lossy to lossless coding. In this chapter, wavelet based visually lossless coder for volumetric medical data is discussed. Wavelet based vision model calculates JND value to eliminate redundant visual information and block matching routine to eliminate slice redundancy.

4.1 WAVELET BASED VISUALLY LOSSLESS CODER

The block diagram of the proposed wavelet based visually lossless compression technique VLIC-4 for volumetric medical data is illustrated in Figure 4.1. The slice redundancy and human visual characteristics are considered to compress the volumetric image data. Each image is first decomposed with 2D DWT for l scales. A wavelet based vision model is used to measure the JND followed by a JND dependent quantizer to remove visually irrelevant information. On the resulting image slices, block matching algorithm is applied to remove inter-slice redundancy. The image residue generated by the block matching algorithm and displacement vectors are compressed using arithmetic coding.

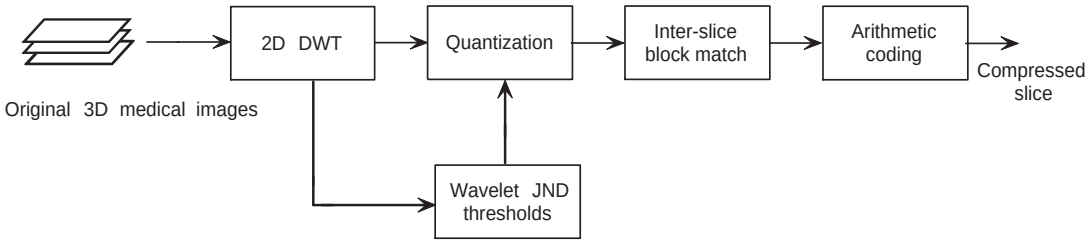

Figure 4.1: Block diagram of Wavelet based visually lossless coder

4.1.1 2D Discrete Wavelet Transform

The basic principle of the 2D DWT is to represent a 2D signal as a superposition of a wavelet basis. The coefficients of the basis can then be utilized to reconstruct the original information. The 2D DWT gives frequency and spatial representation of 2D signals. Each scale of the transform decomposes its input into four spatial frequency subbands denoted as LL, LH, HL and HH. The orientations are indexed as 1, 2, 3, 4 corresponding to the LL, HL, HH and LH subbands, respectively. The approximation low pass subband LL, is a coarser version of the original signal, while the other subbands represent the high frequency details in the horizontal, vertical and diagonal directions, respectively. The decomposition is usually iterated on the approximation low pass subband, which for natural images contains most of the energy. The wavelet transform has many features that make it suitable for our application, such as the representation of an image at different resolutions and packing of most of the energy in few wavelet coefficients.

4.1.2 JND thresholds for wavelet coefficients

The perceptual redundancy present in an image is measured through JND profile. The visual model uses one JND threshold, $v_{JND}(l, \theta, [m, n])$ for every DWT coefficient at location $[m, n]$ in subband (l, θ), where l is the scale and θ is the orientation. In this work, three important visual characteristics namely contrast sensitivity, luminance masking or light adaption and contrast masking are modeled to determine the JND thresholds (Liu *et al.* 2006). The JND threshold $v_{JND}(l, \theta, [m, n])$ is thus computed as:

$$v_{JND}(l,\theta,[m,n]) = JND_{(l,\theta)}a_l(l,\theta,[m,n])a_c(l,\theta,[m,n]) \tag{4.1}$$

where $JND_{(l,\theta)}$ is the base detection threshold of a subband (l,θ), $a_l(l,\theta,[m,n])$ is the light adaptation adjustment and $a_c(l,\theta,[m,n])$ is the contrast masking adjustment.

The base detection threshold $JND_{(l,\theta)}$ for each subband (l,θ) provides the relative variation in the visible signal over a background with uniform intensity. Contrast is an essential theory in vision science because the response of the HVS depends on the variation of the signal relative to the surrounding background instead of the absolute luminance value.

A mathematical representation of JND threshold is given by (Liu *et al.* 2006)

$$JND_{(l,\theta)} = \frac{a10^{k\left\{log\left(\frac{g_\theta f 2^l}{r}\right)\right\}^2}}{A_{l,\theta}} \tag{4.2}$$

where *a*, *k*, *f*, *r*, and g_θ are constants. Values of these constants are listed in Table 4.1. $A_{l,\theta}$ is the amplitude of the DWT 9/7 kernel basis function. Its value depends on frequency level l, orientation θ and visual resolution of the display in pixels/degree r. Table 4.2 lists the $A_{l,\theta}$ values for a 5-level 9/7 DWT decomposition (Liu *et al.* 2006).

Table 4.1: Parameters for the DWT threshold model (Liu *et al.* 2006)

a	*k*	*f*	g_{LL}	$g_{HL,LH}$	g_{HH}	*r* (pixels/degree)
0.495	0.466	0.401	1.501	1.0	0.534	35

The base detection threshold value change with the background intensity levels. Hence mean luminance of the local image region needs to be considered when calculating detection threshold. Therefore to account for this variation, a luminance masking correction factor must be applied to the contrast sensitivity function. The luminance masking adjustment is approximated as:

$$a_l(l,\theta,[m,n]) = \left(\frac{c(l_{max},LL,[m',n'])}{c_{mean}}\right)^{a_T} \tag{4.3}$$

Table 4.2: Basis function amplitude $A_{l,\theta}$ for a 6 level 9/7 DWT (Liu *et al.* 2006)

Orientation	DWT					
	1	2	3	4	5	6
LL	0.62171	0.34537	0.18004	0.09140	0.045943	0.023013
LH,HL	0.67234	0.413177	0.22727	0.11792	0.059758	0.030018
HH	0.72709	0.49428	0.28688	0.15214	0.077727	0.039156

where $c(l_{max}, LL, [m', n'])$ is the value of the DWT coefficient, in the LL subband, that spatially corresponds to the position $(l, \theta, [m, n])$. In this case, m' and n' can be calculated as $m' = \lfloor \frac{m}{2^{l_{max}-l}} \rfloor$ and $n' = \lfloor \frac{n}{2^{l_{max}-l}} \rfloor$. The parameter a_T controls luminance masking, a value of 0.649 was used (Liu *et al.* 2006).

Contrast masking is another factor that will affect the detection threshold. It is due to the fact that the visibility of one image component changes with the presence of another image component (Chou and Li 1995). Contrast masking estimates the variation of the detection threshold in a target signal as a function of the contrast of the masker. The contrast masking effect can be framed as:

$$a_c(l, \theta, [m, n]) = a_{c\_self}(l, \theta, [m, n]) a_{c\_neigh}(l, \theta, [m, n]) \tag{4.4}$$

where $a_{c\_self}(l, \theta, [m, n])$ is the self contrast masking adjustment factor and $a_{c\_neigh}(l, \theta, [m, n])$ is the neighborhood contrast masking adjustment factor.

A sufficiently large coefficient at the location $(l, \theta, [m, n])$ increases the detection threshold. This variation in detection threshold is incorporated through self contrast masking adjustment factor $a_{c\_self}(l, \theta, [m, n])$. For the DWT coefficients, it is expressed as:

$$a_{c\_self}(l, \theta, [m, n]) = max \left\{ 1, \left(\frac{|c(l, \theta, [m, n])|}{JND_{(l,\theta)} a_l(l, \theta, [m, n])} \right)^{\varepsilon} \right\} \tag{4.5}$$

where $c(l, \theta, [m, n])$ is the DWT coefficient value at location $(l, \theta, [m, n])$. For the LL subband, contrast masking is not applied ($\varepsilon = 0$). For other subbands, ε is 0.6.

In DWT based reconstructed images, the signal formed by DWT coefficient

$c(l,\theta,[m,n])$ is superimposed on other signals formed by the neighboring wavelet coefficients. This phenomenon is taken into account through neighborhood contrast adjustment factor $a_{c\_neigh}(l,\theta,[m,n])$. So there is some masking effect contributed from spatially neighboring signals in the wavelet domain. It is expressed as (Liu *et al.* 2006):

$$a_{c\_neigh}(l,\theta,[m,n]) = max\left\{1, \sum_{k\in\ neighbors\ of\ (l,\theta,[m,n])} \frac{\left|\frac{c_k}{JND_{(l,\theta)}a_l(l,\theta,[m,n])}\right|^{\zeta}}{N_{[m,n]}}\right\} \tag{4.6}$$

where the neighborhood contains the coefficients in the same subband that lies within a window centered at the location $[m,n]$. $N_{[m,n]}$ represents the number of coefficients in that neighborhood. c_k are the neighboring wavelet transform coefficient values. $\zeta = 0.5$ is a constant that controls the influence of the amplitude of each neighboring coefficient.

4.1.3 JND dependent quantizer

This section explains the approach to eliminate the perceptual redundancies. The simplest approach of eliminating the visually redundant information from DWT coefficients is to quantize the DWT coefficients in such a way that absolute value of quantization error is below the JND value. After evaluating the image dependent JND value, each reference or original DWT coefficient $c(l,\theta,[m,n])$ is quantized to get $cd(l,\theta,[m,n])$ through truncation of $c(l,\theta,[m,n])$. So

$$cd_k(l,\theta,[m,n]) = \lfloor \frac{c(l,\theta,[m,n])}{k} \rfloor \times k \tag{4.7}$$

where $\lfloor\ \rfloor$ is the truncation function and *k* is an integer. Finally, if the quantized DWT coefficient $cd_k(l,\theta,[m,n])$ is below the JND threshold $v_{JND}(l,\theta,[m,n])$, the reference DWT coefficient $c(l,\theta,[m,n])$ at location $[m,n]$ is replaced by the corresponding quantized DWT coefficient $cd_k(l,\theta,[m,n])$. The pseudo code of this procedure is shown in Figure 4.2, where $cv(l,\theta,[m,n])$ is visually lossless DWT coefficient.

Procedure for eliminating visual redundancy:

$cv(l,\theta,[m,n]) = c(l,\theta,[m,n]);$

for k=4:2

$cd_k(l,\theta,[m,n]) = \lfloor \frac{c(l,\theta,[m,n])}{k} \rfloor \times k;$

if $\mid c(l,\theta,[m,n]) - cd_k(l,\theta,[m,n]) \mid \leqslant v_{JND}(l,\theta,[m,n])$ *then*

$cv(l,\theta,[m,n]) = cd_k(l,\theta,[m,n]);$

break

end if

end for

Figure 4.2: Pseudo code for eliminating visual redundancy

4.1.4 Inter-slice block matching:

A structural correlation exists between the stack of medical image slices because each slice generated is usually a cross section of the human body and is parallel to adjacent slices. In this stage, CR is improved by exploring the correlation in the slice direction. The inter-slice block matching is used to estimate current slice of a residual image using the previous image. This procedure is same as explained in section 3.1.4. The residual image after block matching is encoded using adaptive arithmetic coding.

4.2 IMPLEMENTATION

The proposed method has been simulated using Matlab®8.2 on an Intel® i7 Core. The performance of the wavelet based and pixel based Visually Lossless Coder (VLC) for volumetric medical image sets are compared with a few of the standard image compression codecs. The coder is developed for a viewing distance of 24 inches (approximately

arm's length) and for a display with around 35 pixels/degree display visual resolution. DWT is implemented with 9/7 wavelet filter with scale of 5. The value of parameters *a*, *k*, *f*, *r* and g_θ used in the JND model are based on the experiment carried with various models to express the threshold for gray scale DWT noise as a function of spatial frequency and orientation θ (Watson *et al.* 1997). The performance of the VLIC-4 algorithm is tested on several sets of MRI, CT, and X-ray Angiography image data-JPEG 2000 encoding with perceptual distortion control (Bilgin *et al.* 1998; Sanchez and Bartrina-Rapesta 2014; Bruylants *et al.* 2015). Details of these test image data sets are summarized in Table 2.9, Table 2.10 and Table 2.11. Results obtained with 3157 slices of CT images, 886 slices of MR images and 608 slices of X-ray Angio slices are documented.

4.3 RESULTS AND DISCUSSIONS

4.3.1 Performance of coder with and without neighborhood masking

The influence of neighborhood contrast adjustment along with self contrast adjustment with different bit rates as discussed in section 4.1.2 is shown in Figure 4.3. Table 4.3 compares quality metrics such as PSNR and VIF against the bit rate for VLC considering only self masking and VLC considering both self and neighborhood masking. For almost same quality, VLC with both maskings gives reduced bit rate. An overall improvement of 7.89 % in bit rate is obtained. VLC with neighborhood contrast adjustment increases the computation complexity, as $a_{c\_neigh}(l, \theta, [m, n])$ value has to be computed (Equation 4.6) in 5×5 neighborhood, but there is an improvement in CR. Both self and neighborhood masking factors are considered in the implementation of coder.

Simulations were carried out for $9/7$ wavelet filter and five levels of frequency decomposition. Biorthogonal $9/7$ wavelet filter set is used as it gives good compres-

sion and has been used extensively in image compression applications (Villasenor *et al.* 1995). In general, as the number of decomposition levels is increased, the coding efficiency improves upto an optimum point and then levels off. It has been shown that most of the coding efficiency is contributed by the first three to five decomposition levels (Adams and Ward 2001), hence five levels of decomposition was chosen.

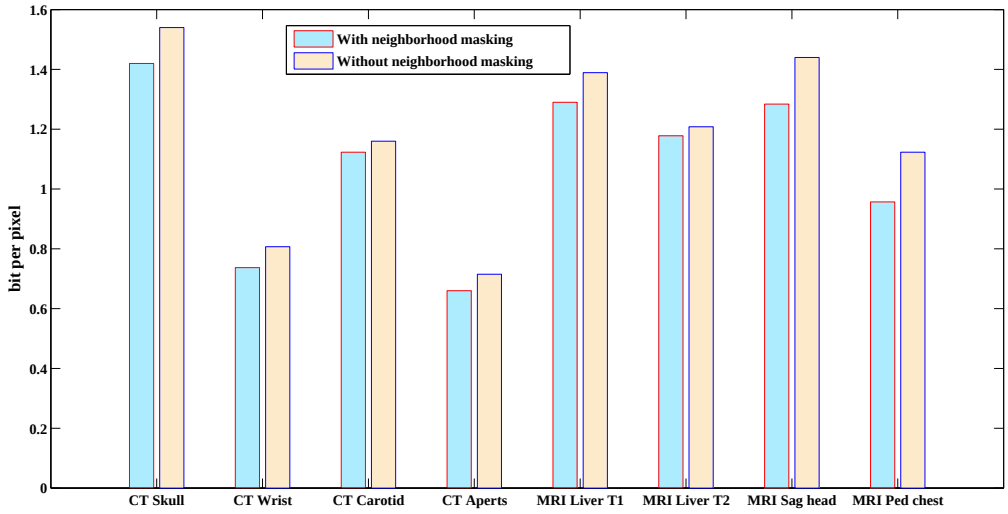

Figure 4.3: Comparison of the bit rate for the medical image data sets with and without neighborhood masking.

4.3.2 Effect of scales in DWT

It is important to check the effect of decomposition levels in DWT on visually lossless CR. Simulations were carried out for six levels of frequency decomposition. As mentioned in section 4.1.2, basis function amplitude $A_{l,\theta}$ is not same for different frequency levels of DWT and hence the JND values. The pseudo code for quantizing the DWT coefficients to get the undistorted image is given in Figure 4.2. In this case, the image is decomposed using $9/7$ wavelet filter bank. It is possible to represent the data in more redundant form by increasing the number of levels of frequency decomposition in DWT. So higher levels of decomposition should provide better CR. Figure 4.4, reconfirms this fact.

Table 4.3: Bit rate and quality metrics of the reconstructed image with and without neighborhood masking (Medical image data set 1, Table 2.9)

Label	Self masking				Self and neighborhood masking			
	bpp	PSNR (dB)	VSNR (dB)	VIF	bpp	PSNR (dB)	VSNR (dB)	VIF
CT Skull	1.540	50.85	45.51	0.945	1.420	50.76	45.69	0.943
CT Wrist	0.807	52.59	52.72	0.941	0.737	52.53	52.75	0.941
CT Carotid	1.160	52.35	49.94	0.95	1.123	52.33	49.94	0.95
CT Aperts	0.715	54.94	56.30	0.959	0.660	54.91	56.33	0.959
MRI Liver T1	1.389	49.66	45.38	0.94	1.290	49.62	45.39	0.939
MRI Liver T2	1.208	51.82	46.34	0.958	1.178	51.81	46.34	0.958
MRI Sag head	1.440	51.16	52.72	0.93	1.284	51.10	52.74	0.928
MRI Ped chest	1.123	50.03	55.60	0.913	0.957	49.94	55.68	0.911

Table 4.4: Comparison of Visually lossless bit rate (bpp) and VIF of reconstructed image for Wavelet decomposition levels 1 to 6 (Medical image data set 1, Table 2.9)

Label	Wavelet based (Daub 9/7) VLC					
	Level-1 (bpp/VIF)	Level-2 (bpp/VIF)	Level-3 (bpp/VIF)	Level-4 (bpp/VIF)	Level-5 (bpp/VIF)	Level-6 (bpp/VIF)
CT Skull	2.156/0.958	2.064/0.951	1.928/0.949	1.747/0.947	1.540/0.945	1.52/0.943
CT Wrist	1.290/0.967	1.231/0.950	1.040/0.947	0.914/ 0.943	0.807/ 0.941	0.803/ 0.940
CT Carotid	1.744/ 0.97	1.656/ 0.958	1.427/ 0.95	1.218/0.95	1.160/0.95	1.158/0.95
CT Aperts	1.173/0.978	1.190/0.970	1.032/0.966	0.833/0.960	0.715/0.959	0.708/0.957
MRI Liver T1	2.324/0.96	2.293/0.95	1.981/ 0.945	1.657/ 0.94	1.389/ 0.94	1.277/ 0.939
MRI Liver T2	1.744/0.965	1.585/0.96	1.4/0.958	1.27/ 0.958	1.208/ 0.958	1.199/ 0.958
MRI Sag head	2.187/0.95	2.259/0.944	2.092/0.94	1.829/ 0.93	1.44/ 0.93	1.435/ 0.93
MRI Ped chest	1.873/0.949	1.887/0.938	1.677/0.928	1.411/0.919	1.123/0.913	1.117/0.908

Considering all 4 sets of CT and 4 sets of MR images, the average reduction in bit rate from level 1 to level 5 is 35.46 %. Table 4.4 compares the bit rate (bpp) and VIF across the different levels. For different frequency levels, bit rate (bpp) and PSNR (dB) comparison is given in Table 4.5. Similarly, bpp and VSNR (dB) for various levels

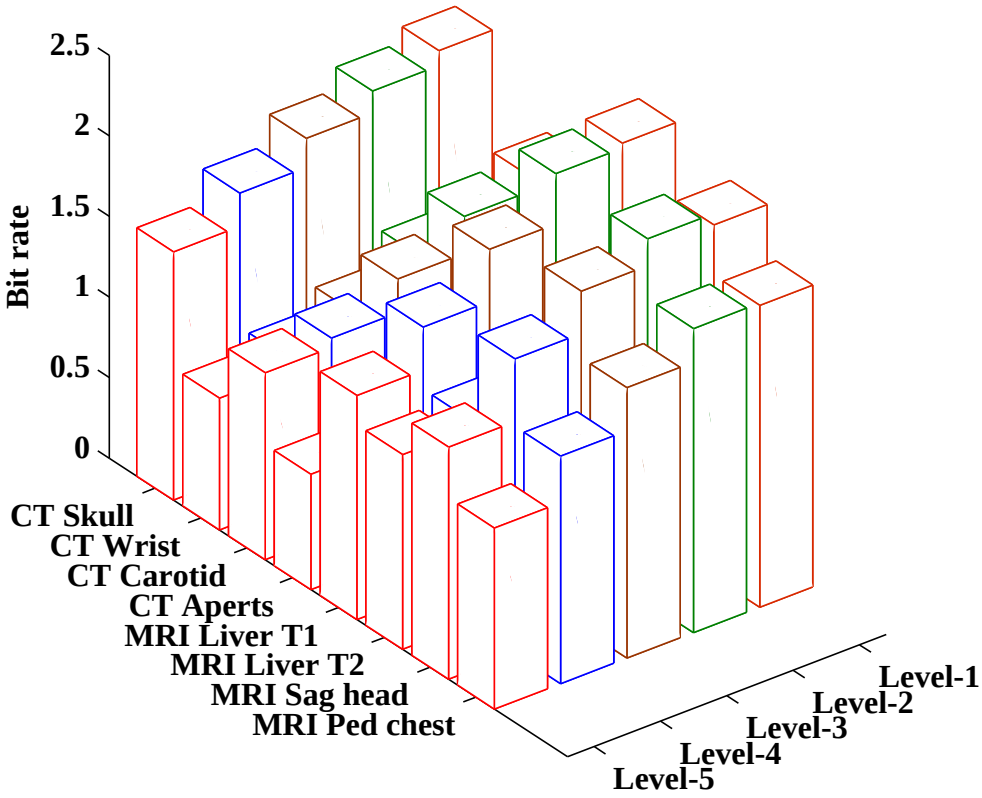

Figure 4.4: Comparison of VLC bit rate for scales from 1 to 5 with all test data sets.

are listed in Table 4.6. The maximum decrease in VIF, PSNR, and VSNR value from level-1 to level-5 across all images in the data set-1 are 3.71 %, 4.33 % and 1.06 % respectively. Tabulated PSNR, VIF, and VSNR values for levels 1 to 5 demonstrate that there is no perceivable distortion by increasing the scale since there is not much difference in quality metric values from scale 1 to 5. Since the improvement in the CR from level-5 to level-6 was only 0.671%, five levels of decomposition was chosen.

4.3.3 Effect of type of wavelet filter

The impact of wavelet filters on bit rate and visual quality of the reconstructed image is tested. Table 4.7 compares the performance of visually lossless coder with 9/7 wavelet

Table 4.5: Comparison of Visually lossless bit rate (bpp) and PSNR (in dB) of reconstructed image for Wavelet decomposition levels 1 to 6 (Medical image data set 1, Table 2.9)

Label	Wavelet based (Daub 9/7) VLC					
	Level-1 (bpp/PSNR)	Level-2 (bpp/PSNR)	Level-3 (bpp/PSNR)	Level-4 (bpp/PSNR)	Level-5 (bpp/PSNR)	Level-6 (bpp/PSNR)
CT Skull	2.156/52.07	2.064/ 51.39	1.928/ 51.28	1.747/ 51.11	1.54/50.85	1.52/50.63
CT Wrist	1.29/54.85	1.231/53.23	1.040/52.90	0.914/ 52.70	0.807/ 52.59	0.803/ 52.35
CT Carotid	1.744/54.16	1.656/ 52.96	1.427/ 52.60	1.218/52.39	1.160/52.35	1.158/52.24
CT Aperts	1.173/57.43	1.190/56.30	1.032/55.70	0.833/55.13	0.715/54.94	0.708/54.77
MRI Liver T1	2.324/51.63	2.293/50.57	1.981/50.12	1.657/ 49.82	1.389/49.66	1.277/49.54
MRI Liver T2	1.744/52.83	1.585/52.15	1.400/51.95	1.270/51.86	1.208/51.82	1.199/51.66
MRI Sag head	2.187/52.59	2.259/52.21	2.092/51.85	1.829/51.48	1.440/ 51.16	1.435/ 51.02
MRI Ped chest	1.873/52.12	1.887/51.13	1.677/50.74	1.411/50.33	1.123/50.03	1.117/49.98

Table 4.6: Comparison of Visually lossless bit rate (bpp) and VSNR (in dB) of reconstructed image for Wavelet decomposition levels 1 to 6 (Medical image data set 1, Table 2.9)

Label	Wavelet based (Daub 9/7) VLC					
	Level-1 (bpp/VSNR)	Level-2 (bpp/VSNR)	Level-3 (bpp/VSNR)	Level-4 (bpp/VSNR)	Level-5 (bpp/VSNR)	Level-6 (bpp/VSNR)
CT Skull	2.156/45.37	2.064/45.52	1.928/45.33	1.747/45.37	1.540/45.51	1.52/45.29
CT Wrist	1.290/53.29	1.231/52.72	1.040/52.67	0.914/52.68	0.807/52.72	0.803/52.61
CT Carotid	1.744/50.24	1.656/50.06	1.427/49.96	1.218/49.94	1.160/49.94	1.158/49.92
CT Aperts	1.173/56.57	1.190/56.39	1.032/56.13	0.833/56.11	0.715/56.30	0.708/56.05
MRI Liver T1	2.324/45.90	2.293/45.59	1.981/45.42	1.657/45.37	1.389/45.38	1.277/45.38
MRI Liver T2	1.744/46.73	1.585/46.58	1.400/46.36	1.270/46.37	1.208/46.34	1.199/46.29
MRI Sag head	2.187/52.41	2.259/52.54	2.092/52.43	1.829/52.59	1.440/52.72	1.435/52.25
MRI Ped chest	1.873/55.45	1.887/55.55	1.677/55.42	1.411/55.44	1.123/55.60	1.117/55.28

kernel and 5/3 wavelet kernels. For the lossy compression, 9/7 wavelet kernel performs better than 5/3 wavelet kernel. For the same image quality 9/7 wavelet kernel improves the compression by 35.16%.

Table 4.7: Comparison of visually lossless bit rate (bpp) and PSNR (dB) with 9/7 and 5/3 kernels (Medical image data set 1, Table 2.9)

Label	With wavelet 9/7 kernel	With wavelet 5/3 kernel
CT Skull	0.99 / 40.88	1.42 / 39.95
CT Wrist	0.54 / 44.05	0.84 / 41.66
CT Carotid	0.62 / 42.99	0.968 / 41.29
CT Aperts	0.64 / 44.42	1.06 / 44.42
MRI Liver T1	0.8 / 41.84	1.36 / 39.19
MRI Liver T2	0.75 / 40.81	1.02 / 40.52
MRI Sag head	0.92 / 41.66	1.29 /41.07
MRI Ped chest	0.73 / 42.32	1.29 / 40.33

4.3.4 Effect of pixel based and wavelet based JND model on VLC

The performance of visually lossless coders with pixel based visual model explained in section 3.2.1 and the wavelet based visual model of section 4.1.2 are compared. Pixel based visual model is dependent on average background luminance, spatial luminance gradient, and texture masking. It does not decompose the image into different frequency levels to represent in more redundant form like wavelet based approach. So wavelet based VLC performs better than the pixel based coder. Table 4.8 demonstrates this fact, and there is a reduction in bit rate by 30.01 % in the case of wavelet based vision model against pixel based VLC.

4.3.5 Comparison of performance of VLC and lossless codecs

Wavelet based VLC (VLIC-4) is compared with state of the art codecs, such as JPEG-LS (HP-LABS 2016), JPEG2000 (OPEN-JPEG 2016), JPEG3D (OPEN-JPEG-3D 2016), H.264/MPEG-4 AVC (Karsten 2016), DPCM (Ait Aoudia *et al.* 2006), HEVC video coding (Sanchez and Bartrina-Rapesta 2014), MILC (Pizzolante and Carpentieri 2013) and wavelet based (Bruylants *et al.* 2015) lossless compression algorithms.

JPEG-LS is a near-lossless/lossless compression standard for natural images and is based on prediction, residual modeling and context-based coding of the residuals. JPEG2000 (J2K) is the compression standard available for natural images and is used in DICOM standard. JPEG2000 employs 2D integer wavelet transform. HEVC is a standard codec for the compression of video. It employs multi-frame motion compensation and estimation.

Table 4.8: Comparison of visually lossless bit rate (bpp) and PSNR (dB) corresponding to pixel based and wavelet based visual model (Medical image data set 1, Table 2.9)

Image	Pixel based model VLIC-3	Wavelet based model VLIC-4
CT Skull	1.6529 / 50.42	1.51 / 50.79
CT Wrist	1.1377 / 49.05	0.65 / 49.46
CT Carotid	1.5087 / 52.46	1.15 / 52.31
CT Aperts	0.7777 / 50.28	0.77 / 50.51
MRI Liver T1	2.2828 / 42.67	0.81 / 42.65
MRI Liver T2	1.7918 / 51.20	1.2 / 51.79
MRI Sag head	1.5588 / 46.42	1.18 / 47.60
MRI Ped chest	1.3363 / 43.32	0.75 / 43.52

DWT coefficients are truncated for various integer values for the truncation factor k (equation 4.7). The performance of VLC VLIC-4, standard codecs and lossless compression algorithms for the test medical image data base is given in Table 4.9, Table 4.11 and Table 4.12. Comparison of CR of wavelet based VLIC-4 algorithm with lossless techniques is given in Table 4.10. It can be observed that for all the data sets mean $SSIM \approx 1$, indicating VLIC-4 is visually lossless. CR of VLIC-4 is within the acceptable compression range as suggested by Royal College of Radiologists and European Society of Radiology for almost all data volumes Table 2.7. Visually lossless bit rates given in Table 4.9 are obtained by setting value of k to 3 in the process of eliminating the visual redundancy. On 8 bit MR and CT images, wavelet based VLC improves com-

Table 4.9: Comparison of visually lossless bit rates with bit rates of lossless JPEG-2K, JPEG-LS, JPEG3D, H.264/MPEG-4 AVC, DPCM and MILC coders (Medical image data set 1, Table 2.9)

Label	VLIC-4*	JPEG2000	JPEG-LS	JPEG-3D	H.264/ MPEG-4 AVC	DPCM	MILC
CT Skull	1.42 / 1	2.955	2.728	2.120	1.967	2.119	2.030
CT Wrist	0.73 / 1	1.897	1.607	1.258	1.150	1.029	1.066
CT Carotid	1.12 / 1	2.366	1.756	1.567	1.539	1.471	1.358
CT Aperts	0.715 / 0.999	1.245	1.044	0.969	0.819	0.867	0.819
MRI Liver T1	1.29 / 0.994	3.254	3.167	2.379	2.319	2.390	2.196
MRI Liver T2	1.17 / 1	2.541	2.388	1.778	1.769	2.025	1.759
MRI Sag head	1.44 /1	3.952	2.551	2.188	2.015	2.127	2.097
MRI Ped chest	1.12 / 0.991	2.985	2.901	2.131	1.762	1.689	1.655

$*$ bit rate (bpp) / mean SSIM

pression by 60.07% compared to JPEG2000; 48.17% compared to JPEG-LS; 36.41% compared to JPEG-3D, 30.92% compared to H.264/MPEG-4 AVC, 32.20% compared to DPCM and 28.76% compared to MILC.

Visually lossless bit rates given in Table 4.11 are obtained by setting the value of k to 3 and 7 to eliminate visual redundancy. Wavelet based VLC with $k = 3$ reduces the bit rate by 20.66% compared to DPCM, 28.24% compared to HEVC, 14.60% compared to J2K and 13.28% compared to JPEG-LS. Wavelet based VLC with $k = 7$ reduces the bit rate by 61.54% compared to DPCM, 72.56% compared to HEVC, 53.85% compared to J2K and 52.1% compared to JPEG-LS. The proposed coder achieves VIF of 0.98 out of 1 and SSIM of 0.99 out of 1 which proves that the coder is indeed visually lossless at lower bit rates. Performance of VLIC-4 for the data set 3 (Bruylants *et al.* 2015) given in Table 2.11 is tabulated in Table 4.12. VLIC-4 with k=3 reduce the bit rate by 46.85%.

Table 4.10: Comparison of visually lossless CR with CR of lossless JPEG-2K, JPEG-LS, JPEG3D, H.264/MPEG-4 AVC, DPCM and MILC coders (Medical image data set 1, Table 2.9)

Label	VLIC-4*	JPEG2000	JPEG-LS	JPEG-3D	H.264/ MPEG-4 AVC	DPCM	MILC
CT Skull	5.633 / 1	2.707	2.932	3.773	4.067	3.775	3.940
CT Wrist	10.958 / 1	4.217	4.978	6.359	6.956	7.774	7.504
CT Carotid	7.142 / 1	3.381	4.555	5.105	5.198	5.438	5.891
CT Aperts	11.188 / 0.999	6.425	7.662	8.255	9.768	9.227	9.768
MRI Liver T1	6.201 / 0.994	2.458	2.526	3.362	3.449	3.347	3.642
MRI Liver T2	6.837 / 1	3.148	3.350	4.499	4.522	3.950	4.548
MRI Sag head	5.555 /1	2.024	3.136	3.656	3.970	3.761	3.814
MRI Ped chest	7.142 / 0.991	2.680	2.757	3.754	4.540	4.736	4.833

$*$ bit rate (bpp) / mean SSIM

4.3.6 Rate-distortion performance

Simulation is performed to get the quality of reconstructed image at various bit rates. Here visually lossless bit rates are computed considering only one value of k at a time (Figure 4.2). PSNR in dB, VIF values were determined as a function of bit rate. Since SSIM provides the best performance indicator and it gives the closest match to the subjective quality (Kowalik-Urbaniak *et al.* 2014), SSIM quality measure is computed.

Obtained rate-distortion performance is compared with JPEG-2K Part 1 and JPEG-2K Part 2. Kakadu 7.4 version software is used for the implementation of JPEG-2KP1 and JPEG-2KP2 (KAKADU 2016). Figure 4.5 and Figure 4.6 shows reconstructed images with the proposed VLIC for the selected image slices at different bit rates. The plot of quality metrics PSNR, SSIM, and VIF obtained with the VLIC-4 algorithm at various bit rates are shown respectively in Figure 4.7, Figure 4.12 and Figure 4.13. Figure 4.7, Figure 4.12 and Figure 4.13, show that proposed coder achieves higher quality

Table 4.11: Comparison of visually lossless bit rates (bpp) and visual quality obtained with bit rates of lossless coders- DPCM, HEVC, J2K, and JPEG-LS (Sanchez and Bartrina-Rapesta 2014). (Medical image data set 2, Table 2.10).

Image	VLIC-4								Lossless compression (Sanchez and Bartrina-Rapesta 2014)			
	Performance with $k = 3$				Performance with $k = 7$				DPCM	HEVC	J2K	JPEG-LS
	bpp	PSNR (dB)	VIF	SSIM	bpp	PSNR (dB)	VIF	SSIM	bpp	bpp	bpp	bpp
X-ray Angio-1	4.17	72.90	0.98	0.99	3.83	59.72	0.83	0.97	5.10	5.30	4.78	4.74
X-ray Angio-2	4.66	72.92	0.98	0.99	4.02	59.65	0.82	0.97	5.17	5.38	4.81	4.78
X-ray Angio-3	4.27	72.60	0.98	0.99	3.77	58.83	0.82	0.96	5.55	5.60	5.12	5.08
CT-1 Human Thorax	3.96	73.05	0.98	0.99	3.10	60.15	0.82	0.97	4.95	5.28	4.66	4.65
CT-2 Human Thorax	3.92	73.10	0.98	0.99	3.21	60.69	0.83	0.98	4.93	5.38	4.42	4.52
CT-3 Human Thorax	3.89	73.07	0.98	0.99	3.54	61.26	0.82	0.96	4.18	4.51	3.98	4.00
MRI Brain	2.75	50.00	0.97	0.99	1.34	39.38	0.75	0.95	3.29	3.44	3.46	3.30
MRI Cord	2.55	50.02	0.97	0.99	1.29	41.27	0.76	0.97	3.11	3.58	2.78	2.84
MRI Knee	1.26	53.9	0.98	0.99	1.22	41.55	0.76	0.97	1.55	1.62	1.59	1.48

measures for a reasonable range of bit rates. Visual clip of medical images for the region of acceptance are shown in Figure 4.8, Figure 4.9, Figure 4.10 and Figure 4.11.

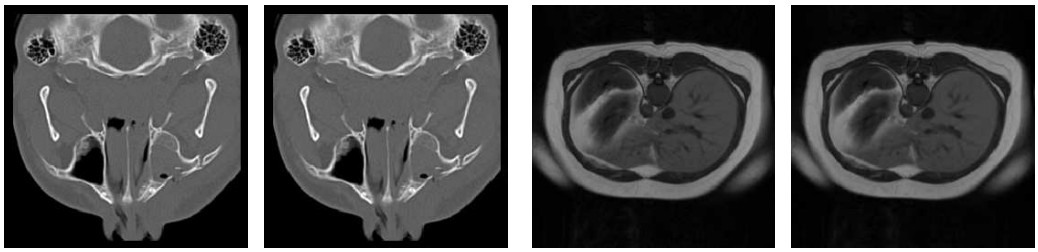

(a) CT Skull (b) CT Skull (c) MRI Liver T1 (d) MRI Liver T1

Figure 4.5: Visual clip of CT Skull (Slice number 60) and MRI Liver T1 (Slice number 20); Images are from test data set (Bilgin *et al.* 1998): (a) CT Skull at bpp of 1.89 and PSNR=51.22 dB (b) CT Skull at bpp of 1.06 and PSNR=42.47 dB (c) MRI Liver T1 at bpp of 2.06 and PSNR=49.52 dB (d) MRI Liver T1 at bpp of 0.84 and PSNR=43.63 dB.

Table 4.12: Comparison of visually lossless bit rates obtained with bit rates of lossless coders JPEG-LS, HEVC, J2K-P1, J2K-P2, and JPEG3D (Bruylants *et al.* 2015). (Medical image data set 3, Table 2.11)

Image	VLIC-4 bit rate/PSNR	JPEG-LS	HEVC	J2K-P1	J2K-P2	JPEG-3D
CT-1 Lung scan	3.16 / 75.52 dB	5.42	5.55	5.52	4.93	4.80
CT-2 Lung scan	5.86 / 76.7 dB	7.83	7.93	7.93	7.65	7.45
CT-3 Spiral Arterial scan	4.40 / 77.01 dB	5.89	6.14	5.87	5.46	5.20
CT-4 Female cadaver	2.25 / 77.48 dB	4.01	4.28	4.09	3.88	3.85
CT-5 Human cadaver	1.70 / 76.04 dB	2.99	3.07	3.20	2.87	2.84
CT-6 Chest	3.58 / 73.79 dB	4.91	5.12	5.17	5.05	5.00
MRI Brain	2.00 / 72.58 dB	3.73	3.71	3.89	3.55	3.56
MRI Brain	3.73 / 72.45 dB	4.58	4.68	4.72	4.14	4.12
MRI Brain	4.19 / 73.03 dB	6.53	6.50	6.69	6.62	6.63

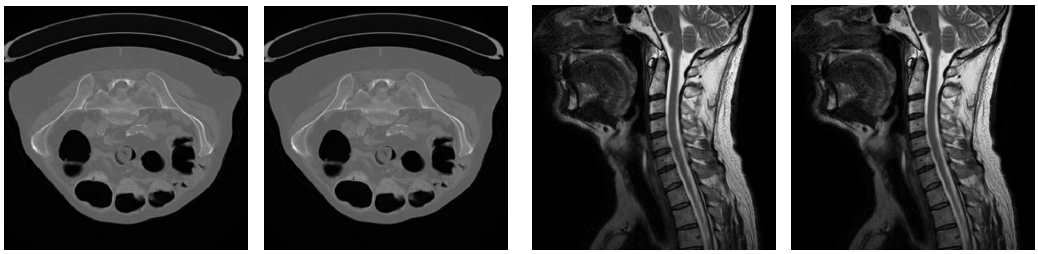

(a) CT-3 image (b) CT-3 image (c) MRI Cord image (d) MRI Cord image

Figure 4.6: Visual clip of CT-3 image (Slice number 50) and MRI Cord image (Slice number 5); Images are from test data set (Sanchez and Bartrina-Rapesta 2014): (a) CT-3 image at bpp of 3.89 and PSNR=73.07 dB (b) CT-3 image at bpp of 3.54 and PSNR=61.26 dB (c) MRI Cord image at bpp of 2.55 and PSNR=50.02 dB (d) MRI Cord image at bpp of 1.29 and PSNR=41.29 dB.

In addition to objective assessment, subjective evaluation was performed to confirm the visual quality of the reconstructed data. Six observers were from the medical field which included radiologists and radiographers. A questionnaire was prepared for all the datasets. The objective quality and the subjective score at the specified average bit

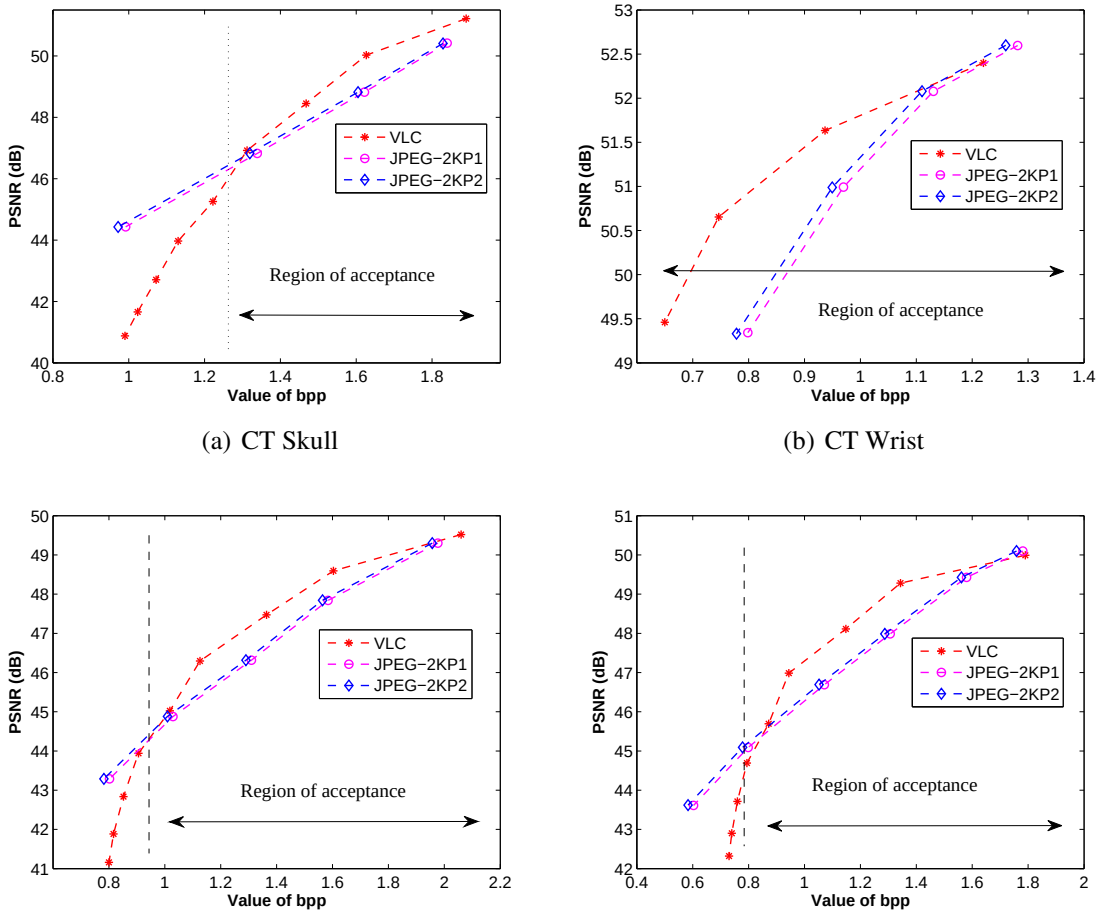

(a) CT Skull (b) CT Wrist

(c) MRI Liver T1 (d) MRI Ped chest

Figure 4.7: Comparison of PSNR (in dB) as a function of bit rate (bpp) for VLIC-4 with JPEG 2000 Part 1 (JP-2KP1) and JPEG 2000 Part 2 (JP-2KP2).

(a) CT Skull (b) CT Skull (c) CT Skull

Figure 4.8: Visual clip of CT Skull (Slice number 40); Images are from test data set 1 (Bilgin *et al.* 1998): (a) Original image (b)Image clip at bpp of 1.89 with PSNR=51.22 dB, SSIM=0.9955 and VIF=0.97 (c) Image clip at bpp of 1.06 with PSNR=42.47 dB, SSIM=0.9702 and VIF=0.76.

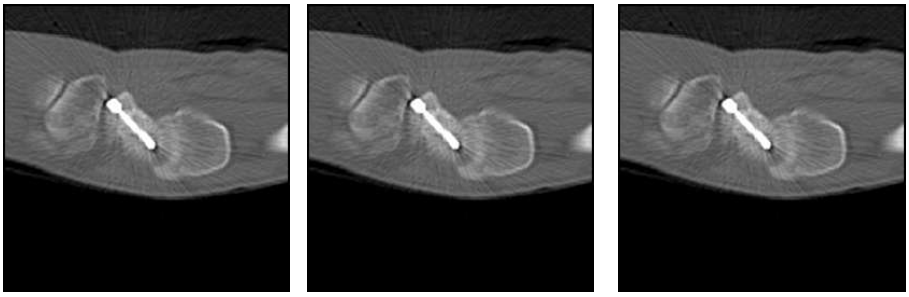

(a) CT Wrist (b) CT Wrist (c) CT Wrist

Figure 4.9: Visual clip of CT Wrist (Slice number 40); Images are from test data set 1 (Bilgin *et al.* 1998): (a) Original image (b)Image clip at bpp of 1.22 with PSNR=52.40 dB, SSIM=0.9963 and VIF=0.9623 (c) Image clip at bpp of 0.548 with PSNR=44.05 dB, SSIM=0.9774 and VIF=0.752.

(a) MRI Liver T1 (b) MRI Liver T1 (c) MRI Liver T1

Figure 4.10: Visual clip of MRI Liver T1 (Slice number 20); Images are from test data set 1 (Bilgin *et al.* 1998): (a) Original image (b) Image clip at bpp of 2.061 with PSNR=49.52 dB, SSIM=0.9932 and VIF=0.9638 (c) Image clip at bpp of 0.806 with PSNR=41.16 dB, SSIM=0.9665 and VIF=0.748

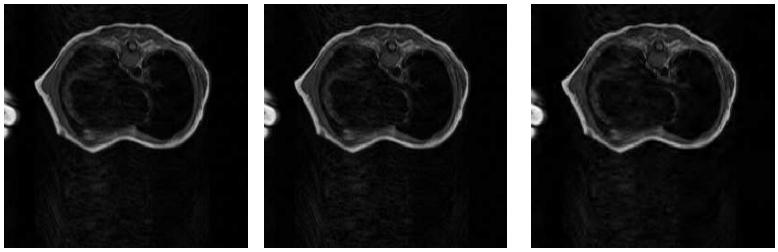

(a) MRI Ped chest (b) MRI Ped chest (c) MRI Ped chest

Figure 4.11: Visual clip of MRI Ped chest (Slice number 40); Images are from test data set 1 (Bilgin *et al.* 1998): (a) Original image (b) Image clip at bpp of 1.796 with PSNR=49.99 dB, SSIM=0.9914 and VIF=0.9697 (c) Image clip at bpp of 0.7379 with PSNR=42.32 dB, SSIM=0.9619 and VIF=0.675.

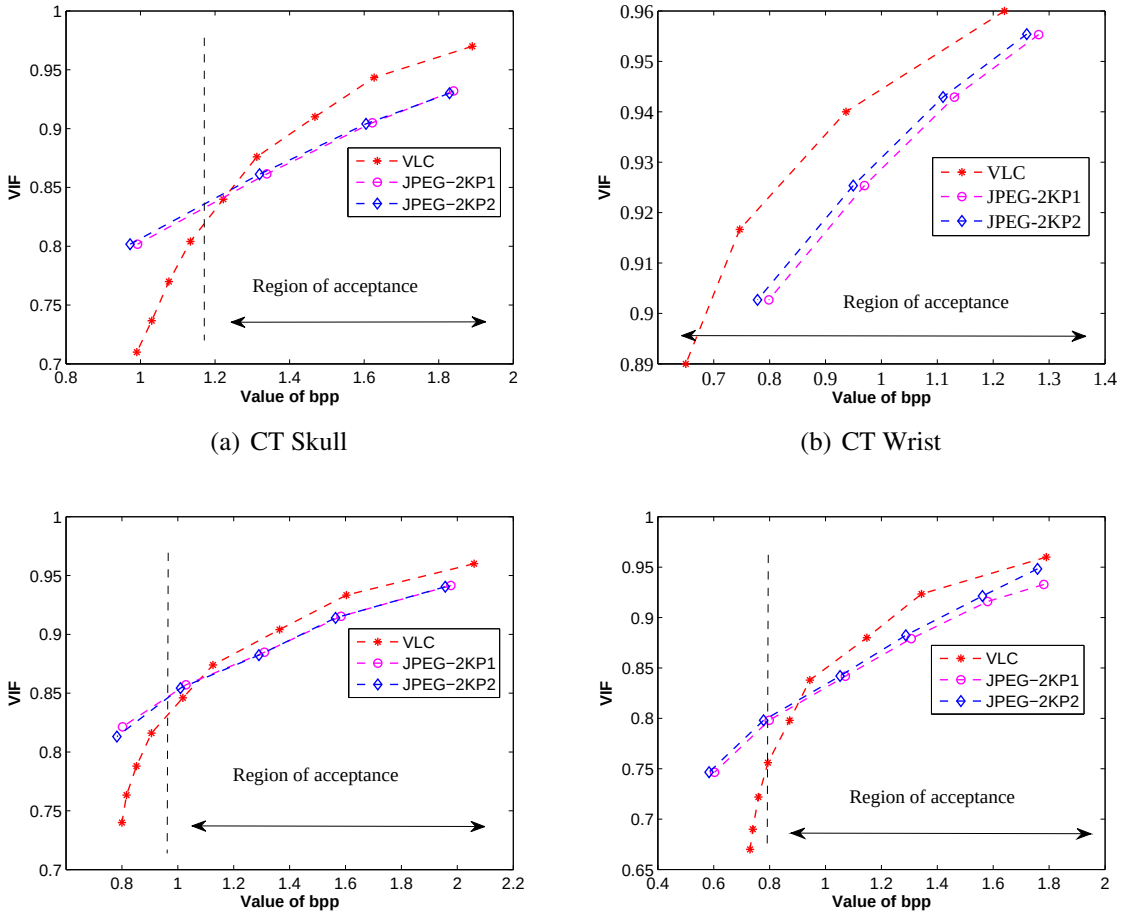

(a) CT Skull

(b) CT Wrist

(c) MRI Liver T1

(d) MRI Ped chest

Figure 4.12: Comparison of VIF as a function of bit rate (bpp) for VLIC-4 with JPEG 2000 Part 1 (JP-2KP1) and JPEG 2000 Part 2 (JP-2KP2).

rate for the data sets is listed in Table 4.13. The observers were shown the original and reconstructed image and were asked to rate the quality on a scale of 1 to 5. A score of 1 represents poor and 5 represents excellent. All the six radiologists have rated the reconstructed images with a score of 5 and assessed that the coder preserved all diagnostically significant information in the brain MRI images used.

4.4 SUMMARY

In this section, a novel wavelet based VLC (VLIC-4) is introduced. A vision model characterizing contrast sensitivity, luminance masking and light adaptation features of

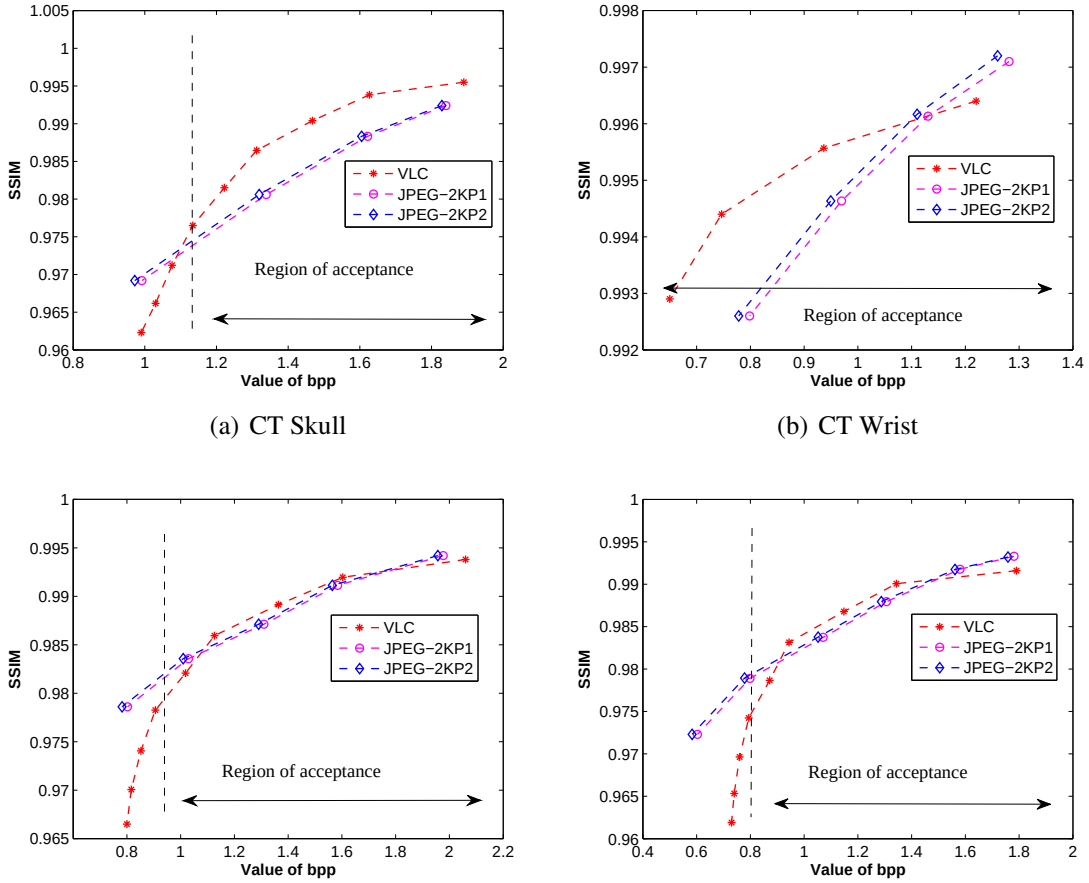

(a) CT Skull

(b) CT Wrist

(c) MRI Liver T1

(d) MRI Ped chest

Figure 4.13: Comparison of SSIM as a function of bit rate (bpp) for VLIC-4 with JPEG 2000 Part 1 (JP-2KP1) and JPEG 2000 Part 2 (JP-2KP2).

human vision represented in wavelet domain is incorporated to identify and measure visually irrelevant information. DWT coefficients are quantized based on visual threshold value to maintain visual quality in the reconstructed image. Lossless block matching algorithm is used to remove slice redundancy. Proposed VLIC-4 was tested on 12 bit and 8 bit CT and MRI standard medical test data set.

Compression performance was compared with state of the art codecs such as JPEG-LS, JPEG2000, JPEG3D image coding standard, H.264/MPEG-4 AVC video coding, DPCM, HEVC video coding, MILC and wavelet based lossless compression algorithms and found to be higher for all data sets. CR performance of VLIC-4 is within the acceptable compression range as suggested by Royal College of Radiologists and European

Table 4.13: Objective and subjective evaluation of VLIC-4 technique; Score allotted: Excellent-5; Very good-4; Good-3; Average-2; Poor-1

Image	Average bpp	Objective measure			Score	
		PSNR(dB)	VIF	SSIM	Radiologist	Radiographer
CT Skull	1.42	50	0.945	0.997	5	5
CT Wrist	0.73	49.98	0.941	0.993	5	5
MRI Liver T1	1.29	49.66	0.94	0.989	5	5
X-ray angio-1	4.17	72.90	0.98	0.99	5	5
CT-1	3.96	73.05	0.98	0.991	5	5
MRI Cord	2.55	50.02	0.97	0.99	5	5

Society of Radiology. HVS based quality metrics such as SSIM and VIF along with PSNR are used to measure the quality of the reconstructed image. Also, quality of VLIC-4 is compared with the JPEG-2K baseline at various bit rates. Rate-distortion performance is found to be better.

The assumption made in all the four algorithms discussed in chapter 3 and chapter 4 is that the entire image is diagnostically important. But the entire region of the image may not be required for the diagnosis in many cases. Hence, ROI/VOI based compression algorithm is proposed in chapter 5 to improve the performance of compression algorithm.

CHAPTER 5

VOI BASED MRI BRAIN IMAGE COMPRESSION

Visually lossless algorithms discussed in chapter 3 and chapter 4 are applied to the entire image. But usually, all the image slices acquired, and the whole region of images may not be required in the diagnosis. So diagnostically critical parts like tumor and lesions in each slice are to be compressed without loss of information, and other regions can be compressed with loss. A hybrid compression algorithm for 3D medical images involving both visually lossless and lossy techniques not only maintains the quality in VOI but also provides overall improvement in CR. However, before applying this method, there is a need to use an automatic tumor or abnormality detection algorithm to determine ROI/VOI. This chapter presents VOI based MRI image compression. After taking ROI/VOI using score function determined by Bhattacharya coefficient (Fukunaga 2013), VLIC-4 algorithm is applied. To rest of the image DCT lossy compression is applied to increase the CR.

5.1 PROPOSED VOI CODER

In this section, VOI based compression technique for MRI brain images is proposed. This algorithm identifies the ROI and applies visually lossless compression technique to this region, while rest of them are compressed with lossy technique. Symmetry based tumor segmentation algorithm is used to detect the diagnostically important region in each image slice and hence VOI is determined across all image slices. Wavelet based VLIC-4 is applied on the segmented VOI, and DCT based lossy compression technique is applied to the residual image.

Proposed VOI based coder is shown in Figure 5.1. This hybrid compression algorithm includes a segmentation algorithm to detect the region of abnormality, a wavelet

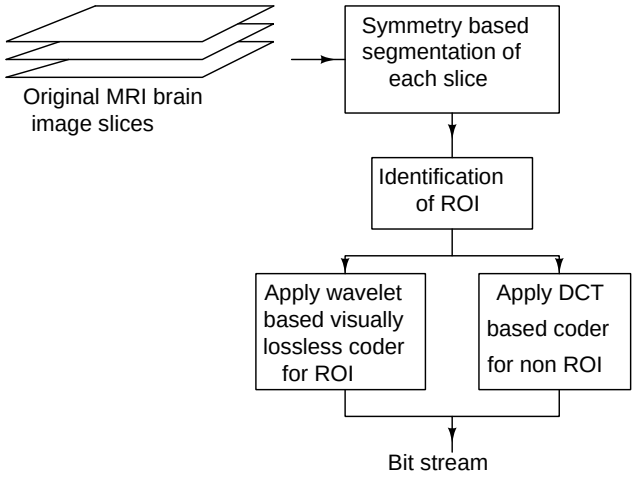

Figure 5.1: VOI based coder

based visually lossless compression algorithm and a DCT based lossy compression technique. Segmentation is carried out in the spatial domain, while the image is compressed in the transform domain.

5.2 SYMMETRY BASED BOUNDING BOX SEGMENTATION FOR TUMOR DETECTION

Segmentation is a procedure that split an image into regions. This step is necessary to identify the ROI in the image. Usually, automatic segmentation technique is used when the image has to be compressed based on the region of importance. In this section, symmetry based bounding box segmentation algorithm (Saha *et al.* 2012) used for the detection of tumor region in MRI brain images is discussed.

Many tumor segmentation methods found in literature are not fully automatic as they need user interaction to place a seed inside the tumor or edema region (Ashton *et al.* 2003; Fletcher-Heath *et al.* 2001). Region growing (Kaus *et al.* 2001) based tumor detection techniques computationally complex.

Most of the fuzzy models (Fletcher-Heath *et al.* 2001) work well only for hyper intensity (fully enhanced) tumors and exhibits poor performance in the case of non-

enhanced tumors. So an automatic and fast segmentation technique (Saha *et al.* 2012) is used to locate a bounding box around the tumor or edema on an MR slice.

Each MRI brain image slice is split along with the line of symmetry into two halves. One-half of the image is considered as reference image R and another half as the test image T. Thus the assumption made is that abnormality is located either in reference or test image. Next, the image T is compared with image R to locate the diseased area. Pointwise subtraction is the straightforward method used to compare two images. But many times pointwise subtraction of images $|T - R|$ fails to recognize the region of abnormality, since even in a healthy brain without abnormality, two halves of the brain do not match exactly (Radke *et al.* 2005). So region-based method is used.

In this segmentation technique, a score function interpreted by Bhattacharya coefficient is used (Fukunaga 2013). Image intensity histograms of T and R are used to detect the abnormality. First, line of symmetry is obtained by computing a gradient vector flow snake to find the skull boundary (Xu and Prince 1998). The vertical line passing through the centroid of the snake is considered as the axis of symmetry. Left of the axis of symmetry in the medical image is considered as test image and image right of the axis of symmetry after taking reflection is considered as the reference image.

5.2.1 Theory of detection of abnormality in medical images

In this section abnormality detection (change detection) algorithm is discussed. To explain the change detection algorithm consider two frames shown in Figure 5.2. Two rectangle regions $A(d)$ and $B(d)$ are defined in reference image R and test image T. These rectangular regions are defined as $A(d) = [0, W] \times [0, d]$ and $B(d) = [0, W] \times [d, H]$, where W and H are width and height of the image respectively and d is the distance from the top of the images. $A(d)$ and $B(d)$ denote the image domain above and below the horizontal line drawn at a distance d from the top of the image.

The score function $E(d)$ is defined as:

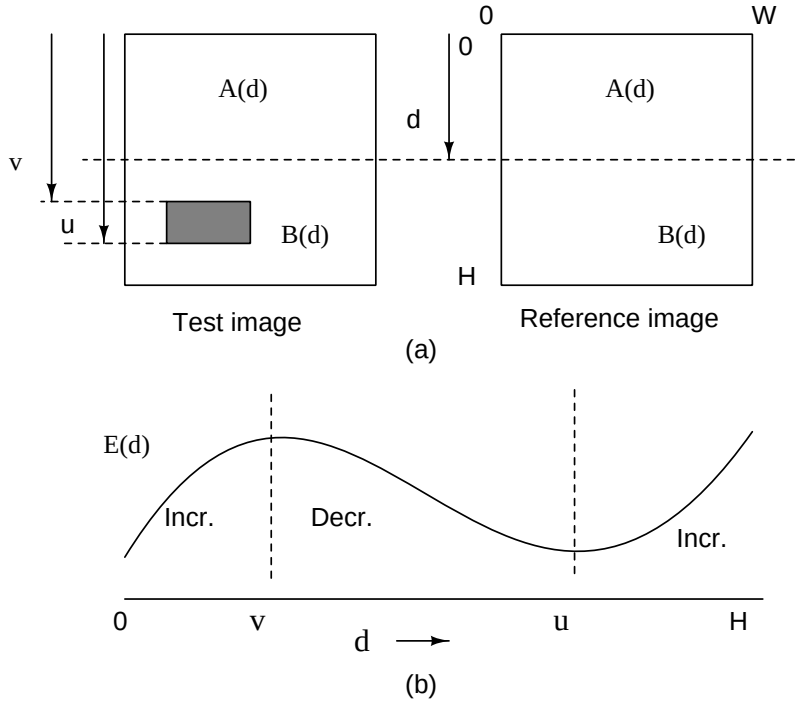

Figure 5.2: (a) Finding the region of abnormality in test image using the reference image. (b) A typical score function plot.

$$E(d) = \langle \sqrt{P_T^{A(d)}}, \sqrt{P_R^{A(d)}} \rangle - \langle \sqrt{P_T^{B(d)}}, \sqrt{P_R^{B(d)}} \rangle \tag{5.1}$$

where

$P_T^{A(d)}$ is the normalized gray level intensity histogram of image T within region $A(d)$,
$P_T^{B(d)}$ is the normalized gray level intensity histogram of image T within region $B(d)$,
$P_R^{A(d)}$ is the normalized gray level intensity histogram of image R within region $A(d)$,
$P_R^{B(d)}$ is the normalized gray level intensity histogram of image R within region $B(d)$.
$\langle \quad \rangle$ is the inner product of two vectors.

Thus, the score function is the difference of Bhattacharya coefficient between the reference and test images above and below the reference line at distance of d from the top of the image. Bhattacharya coefficient is a number between 0 and 1. When normalized gray level intensity histograms are exactly equal, Bhattacharya coefficient is 1, and normalized gray level intensity histograms are very different Bhattacharya coefficient is close to 0. Thus this score metric measures how alike are the two upper

regions and how dissimilar are the two lower regions in images T and R.

For the test image and reference image shown in Figure 5.2, score function should increase first, later decrease and then increase as d increases from 0 to H. The increasing and decreasing path meet at $d = v$ and $d = u$, the upper and lower edges of the bounding box (ROI). In a similar way left and right edges of bounding box can be obtained by rotating test image and the reference image by 90 degrees.

The same procedure is applied on the MRI brain images after finding the axis of symmetry. Axis of symmetry obtained after computing a gradient vector flow snake to find the skull boundary (Xu and Prince 1998) is shown in Figure 5.3(a). Score function plots obtained in vertical and horizontal directions for the MRI brain images are shown respectively in Figure 5.3(c) and Figure 5.3(d). Original MRI image with bounding box obtained using score functions for vertical and horizontal directions is shown in Figure 5.3(b).

5.3 WAVELET BASED VISUALLY LOSSLESS COMPRESSION

The diagnostically important region in each image slice is obtained with symmetry based bounding box segmentation algorithm. Thus VOI is obtained, after deciding the ROI in each of the slices present in one medical image data set. Wavelet based VLIC explained in Chapter 4 is used to compress image within ROI.

5.4 DCT BASED LOSSY COMPRESSION

Medical image outside the VOI is compressed using the lossy technique. DCT based compression technique is used. Image outside the ROI is divided into non-overlapping spatial blocks of size 8×8. Every block is transformed from pixel domain to the frequency domain using two dimensional DCT given by equation (2.1). The DCT co-

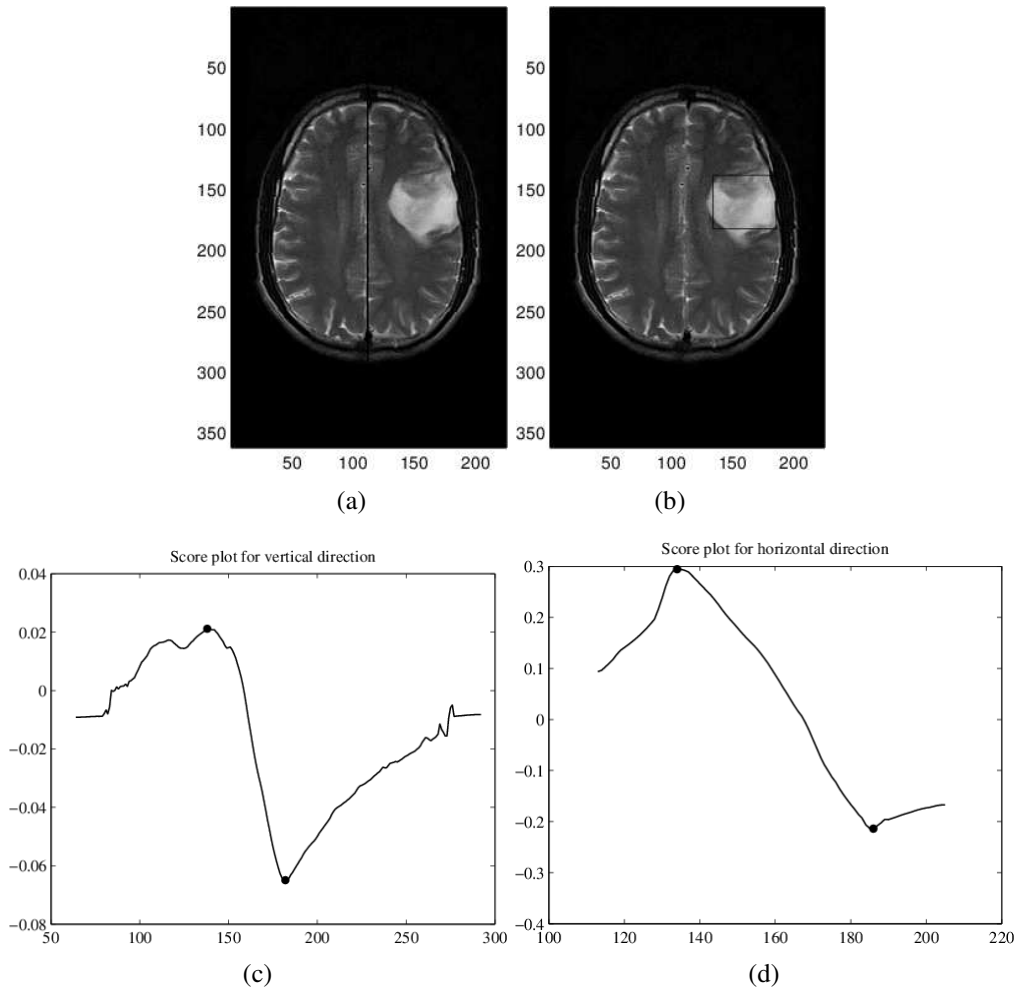

Figure 5.3: (a)MRI image with axis of symmetry, (b) MRI image with bounding box, (c) Score function plot in vertical direction, (d) Score function plot in horizontal direction

efficient will have information concentrated in few coefficients and hence can be easily compressed.

Quantization

The DCT coefficients are quantized before encoding. For the entire block, JPEG like scalar quantization (Wallace 1992) is used. Each of the DCT coefficients is divided by its corresponding quantizer followed by rounding to its nearest integer. This is given by

$$I_q(k,l) = IntegerRound\left[\frac{I(k,l)}{Q(k,l)}\right] \tag{5.2}$$

where $k, l = 0, 1, 2, ...N-1$, $I(k,l)$ represents the transformed coefficient, $I_q(k,l)$ represents the quantized coefficient, $Q(k,l)$ represents the quantizer value. The quantizer value is chosen from a standard quantization table which needs to be specified by the user. In principle, these values can be specified and fine-tuned by the user for maximum compression or quality. The approach as per the JPEG standard (Salomon 2007) is used.

After applying wavelet based VLIC (VLIC-4) for images within VOI and DCT based lossy technique to images outside VOI, a simple prediction method is applied to exploit slice (temporal) redundancy. The following prediction mode obtains the predicted quantized transform domain coefficients.

$$I_{qkr} = I_{qk} - I_{q(k-1)} \tag{5.3}$$

where I_{qkr} is the predicted quantized transform domain coefficient in k^{th} slice, I_{qk} is the quantized transform domain coefficient in k^{th} slice and $I_{q(k-1)}$ is the quantized transform domain coefficient in $(k-1)^{th}$ slice.

Zig Zag Scan

The predicted quantized DCT domain coefficients of each block are arranged in 1-D order through zig zag scan shown in Figure 5.4. Finally predicted quantized trans-

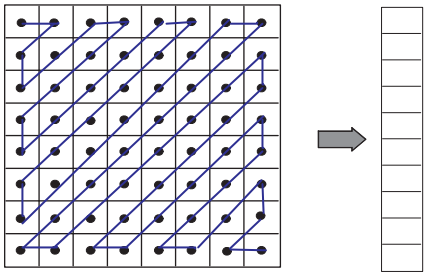

Figure 5.4: Zig-Zag Scan Order

form domain coefficients are encoded using adaptive arithmetic coder to get encoded bit stream.

5.5 SIMULATION RESULTS

VOI based compression technique with wavelet based VLIC and DCT based lossy compression is tested on 12 bit T1 and T2 weighted volumetric MRI brain images obtained with 1.5 Tesla MRI scanner from Hubli scanning center, Hubli, India. Details of these image data sets are given in Table 2.12. The performance of wavelet based compression algorithm VLIC-4 for the test medical data set 4 (Table 2.12) is given in Table 5.1. Also, simulation results of VOI based coder for the same data set are Tabulated in Table 5.2. SSIM quality metrics tabulated in Table 5.1 and Table 5.2 are almost same. Since, SSIM index value is above 0.94, there is no risk that the reconstructed image will be marked as unacceptable (Kowalik-Urbaniak *et al.* 2014). Also, SSIM is one of the best performance indicators and it gives the closest match to the subjective quality (Kowalik-Urbaniak *et al.* 2014), it can be concluded that there is no deterioration in the visual quality of image. A sample of original medical image slice from each data set and corresponding reconstructed image with VOI based coder are shown in Figure 5.5 and Figure 5.6.

In addition to objective assessment, subjective assessment is carried out with the help of radiologists asking their opinion about the presence of diagnostic information in the reconstructed image compared to the corresponding original image. The radiologists have evaluated that the coder preserved all diagnostically significant information in the brain MRI images used. Radiologists feedback report is given in Figure 5.7.

Table 5.1: Bit rate and quality metrics of reconstructed image with VLIC-4

Image	bit rate	PSNR (dB)	VIF	SSIM	VSNR (dB)
Volume-1	4.312	74.57	0.9945	0.9997	59.68
Volume-2	4.671	73.12	0.9943	0.9998	60.45
Volume-3	5.467	74.64	0.9931	0.9998	63.79
Volume-4	4.159	74.92	0.9954	0.9995	51.48
Volume-5	4.904	74.35	0.9969	0.9997	60.33
Volume-6	4.082	74.06	0.9942	0.9997	56.69
Volume-7	3.837	74.16	0.9969	0.9996	56.41
Volume-8	4.484	74.49	0.9967	0.9995	57.29
Volume-9	5.078	74.40	0.9925	0.9998	63.04
Volume-10	5.309	74.18	0.9938	0.9997	61.85
Volume-11	4.755	74.15	0.9985	0.9995	54.90
Volume-12	3.589	74.33	0.9975	0.9995	62.53
Volume-13	3.763	74.19	0.9982	0.9995	57.98
Volume-14	4.610	74.19	0.9982	0.9995	57.98
Volume-15	3.340	74.65	0.9957	0.9994	60.08
Volume-16	4.049	74.08	0.9943	0.9997	58.76
Volume-17	4.241	73.95	0.9924	0.9998	60.04
Volume-18	3.865	74.09	0.9955	0.9997	57.68
Volume-19	3.589	74.33	0.9935	0.9996	62.51
Volume-20	4.072	74.01	0.9943	0.9998	56.67

Table 5.2: Bit rate and quality metrics of reconstructed image with VOI based algorithm; Region A is VOI, Region B is Non-VOI

Image	VOI based algorithm									
	bpp	PSNR for region		VIF for region		SSIM for region		VSNR for region		% VOI
		A	B	A	B	A	B	A	B	
Volume-1	2.974	75.25	52.82	0.9998	0.9438	0.9963	0.7575	61.79	42.87	15.62
Volume-2	2.466	75.26	59.95	0.9997	0.9584	0.9961	0.7729	55.88	41.26	13.24
Volume-3	3.611	83.43	51.73	1	0.9629	0.9973	0.7847	59.72	49.17	15
Volume-4	2.387	75.84	58.49	0.9990	0.9332	0.9938	0.708	65.84	49.00	17.18
Volume-5	3.142	82.34	52.59	0.9999	0.9364	0.9970	0.7589	52.59	45.64	19.64
Volume-6	2.261	75.26	59.14	0.9995	0.9533	0.9955	0.7664	62.37	42.82	9.78
Volume-7	1.973	75.27	59.96	0.9996	0.9424	0.9957	0.7537	64.56	44.26	6.94
Volume-8	2.341	86.72	54.35	0.9999	0.9202	0.9967	0.7300	56.06	41.99	7.14
Volume-9	4.450	75.38	55.16	0.9997	0.9847	0.9959	0.7848	55.16	47.74	35.41
Volume-10	3.013	75.27	53.48	0.9997	0.9610	0.9959	0.7529	57.23	47.43	29.09
Volume-11	2.438	85.02	54.45	0.9999	0.8653	0.9953	0.7027	51.86	43.63	10.71
Volume-12	2.022	75.27	60.88	0.9995	0.9519	0.9960	0.7739	65.43	48.81	8.92
Volume-13	2.575	75.26	61.07	0.9995	0.9443	0.9958	0.7501	62.32	45.54	17.96
Volume-14	2.941	75.27	54.76	0.9998	0.9264	0.9965	0.7370	51.49	43.86	15.55
Volume-15	1.911	75.26	61.45	0.9991	0.9543	0.9951	0.7613	58.00	46.84	8.75
Volume-16	2.322	75.26	59.42	0.9994	0.9548	0.9955	0.7723	57.09	44.038	8.63
Volume-17	2.284	75.26	58.32	0.9996	0.9684	0.9958	0.7908	55.85	46.53	7.29
Volume-18	2.030	75.25	59.82	0.9994	0.9482	0.9954	0.7635	55.94	43.40	9.77
Volume-19	3.003	75.28	54.24	0.9998	0.9189	0.9965	0.7563	59.03	47.55	16.84
Volume-20	2.428	85.23	56.86	0.9996	0.9237	0.9935	0.7045	53.78	45.05	12.89

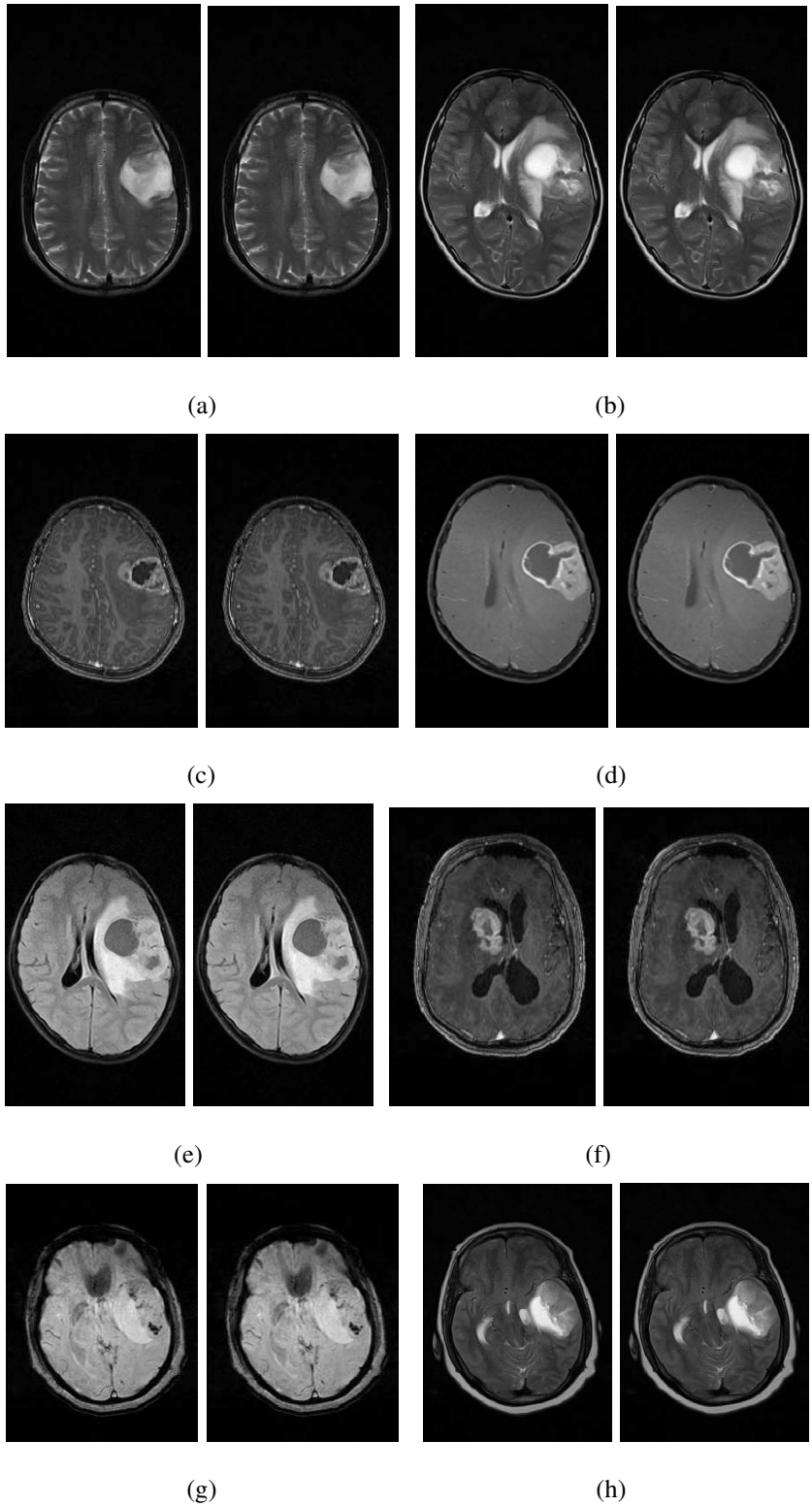

Figure 5.5: Visual clip of MRI brain images given in Table 2.12: Original and reconstructed images with axial view (reconstructed with VOI based coder)

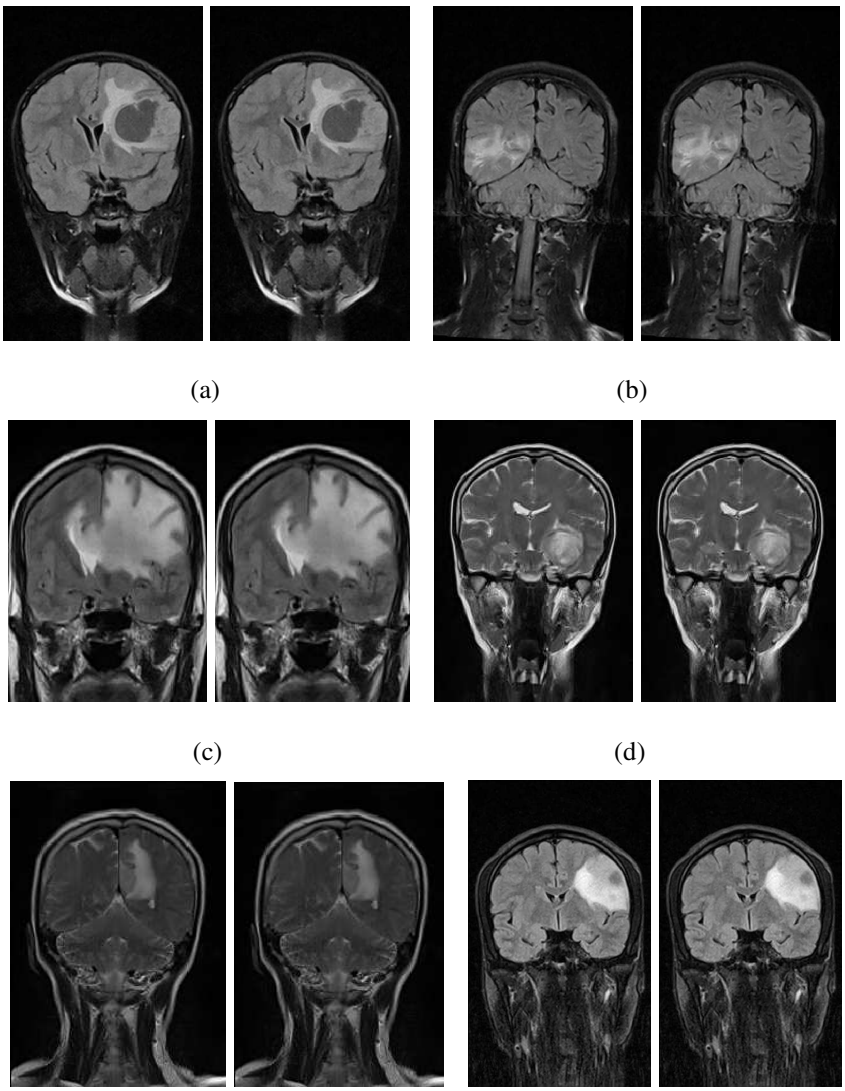

Figure 5.6: Visual clip of MRI brain images given in Table 2.12: Original and reconstructed images with coronal view (reconstructed with VOI based coder)

5.6 SUMMARY

In this chapter, VOI based compression algorithm (VLIC-5) for MRI brain images is proposed. A fast automatic symmetry based bounding box MRI brain tumor detection algorithm is used to segment the brain image. Based on the identification of the presence of an abnormality in each slice, VOI is determined for a volumetric medical image.

Radiologist's Feedback

I have gone through the work done by Chandrika B K (EC11F01) PhD student of National Institute of Technology Karnataka, Surathkal, working in "Visually Lossless Compression of Volumetric Medical Images". The reconstructed images with developed algorithm are compared with original images based on the diagnostic results. I have arrived at the following conclusions.

MRI Brain Image	Grading given by Radiologist			Remarks
	Good	Average	Poor	
Volume-1; Slice-95	✓			
Volume-2;Slice -27	✓			
Volume-3;Slice-17	✓			
Volume-4;Slice-29	✓			
Volume-5;Slice-45	✓			
Volume-6;Slice-175	✓			
Volume-7;Slice-19	✓			
Volume-8;Slice-25	✓			
Volume-9;Slice-25	✓			
Volume-10;Slice-15	✓			
Volume-11;Slice-25	✓			
Volume-12; Slice-11	✓			
Volume-13; Slice-39	✓			
Volume-14; Slice-21	✓			
Volume-15; Slice-19	✓			
Volume-16; Slice-21	✓			
Volume-17; Slice-15	✓			
Volume-18; Slice-17	✓			
Volume-19; Slice-19	✓			
Volume-20; Slice-17	✓			

Grading levels are specified after comparison of the original and reconstructed image with respect to diagnostic information.

For the given images of magnifications, the quality of processed images are good.

Regards

Prof. & Head of the
Dept. of Radio Diagnosis
KASTURBA MEDICAL COLLEGE &
KASTURBA HOSPITAL
MANIPAL

Figure 5.7: Radiologist feedback

Wavelet based visually lossless algorithm is applied on the image within VOI region. Rest of the image is compressed with lossy DCT based technique.

The performance of VLIC-5 and wavelet based algorithm VLIC-4 were compared. For almost same SSIM quality, CR performance of VLIC-5 was found to be better. CR performance of VLIC-4 and VLIC-5 is within the acceptable compression range as suggested by Royal College of Radiologists and European Society of Radiology.

HVS based quality metrics such as SSIM, VSNR, and VIF along with PSNR are used to measure the quality of the reconstructed image. Both subjective and objective evaluations are done and are found to be good. Subjective assessment is carried out with the help of radiologists asking their opinion about the presence of diagnostic information in the reconstructed image compared to the corresponding original image.

CHAPTER 6

CONCLUSIONS

Medical image compression is a process of encoding the original medical image with minimum possible bits per pixel without losing any information. It is possible by eliminating the redundant information present in the image. Image compression techniques are essential when a large volume of image data has to be stored or transmitted. Lossless compression techniques are preferred in the medical field, as there is no loss of information in spite of lower compression efficiency as compared to lossy compression techniques. VLIC techniques achieve better compression without any loss in diagnostically important information.

Visually lossless coding of volumetric medical images is a novel technique that exploits visual redundancies along with statistical and temporal redundancies to improve the performance of the coding system. The fundamental principle of visually lossless image coding is to identify and measure visually irrelevant information present in the image using vision model. Vision models are used to emulate the behavior of HVS. The function of vision model is to measure the JND threshold. In most of the VLIC, JND dependent quantizer is used to remove visually irrelevant information.

This thesis explains and implements a novel visually lossless image coder in spatial and wavelet transform domain. JND threshold is determined by incorporating vision model in the coder. Symmetric nature of human anatomy present in medical images is exploited by removing redundancy. Another hybrid coder is also implemented, where diagnostically important VOI region is coded using the visually lossless method and other regions are coded by DCT based lossy method. Compression efficiency of the proposed coders is compared with lossless coders. Also, rate-distortion performance of the proposed coders is compared with that of state of the art lossy coders. HVS based quality metrics like VSNR, VIF, and SSIM are used to evaluate the quality of

the reconstructed images. In addition to objective assessment, subjective assessment is carried out with the help of radiologist.

6.1 PRIMARY CONTRIBUTIONS

In this research, five visually lossless compression algorithms for volumetric medical images are proposed. Algorithms utilize unique characteristics of human vision and medical images. Algorithms are tested on several sets of MRI, CT, X-ray Angio images. Results obtained with 3157 slices of CT images, 886 slices of MR images, 608 slices of X-ray Angio slices and 587 slices of MRI brain images with tumor are documented to compare the performance.

First three algorithms are implemented in the spatial domain while fourth and fifth algorithms are developed in the transform domain. In the first four algorithms, block match routine is used to remove inter-slice correlation. A JND dependent quantizer is embedded into the system to convert lossless compression algorithm into visually lossless compression algorithm by removing perceptually redundant information. In VOI based compression technique, automatic brain tumor segmentation procedure is included.

In the first algorithm, symmetry detector technique for automatic detection of symmetry in each image slice is used. Block match based lossless compression scheme is added to exploit slice redundancy. Intra-slice block matching routine also is included in the system to improve the CR if there is symmetry in image slice. Further improvements in the compression ratio are achieved by making lossless algorithm into visually lossless by adding a DPCM block in which quantizer, quantizes the pixel values based on the visual threshold value. Background luminance dependent vision model integrated into DPCM block determines the threshold value. In the case of DPCM and symmetry based visually lossless compression technique (VLIC-1), average % reduction in bit per pixel is 11.8 compared to 3D CB EZW method (Bilgin *et al.* 1998). Complexity of the first algorithm is reduced by eliminating DPCM block from first technique to imple-

ment second technique (VLIC-2), and background luminance dependent vision model is embedded into symmetry based block matching lossless coder.

The performance of the algorithm is further improved in third algorithm (VLIC-3) by embedding an improved vision model. This vision model considers both luminance part of image and texture heterogeneity that reduces the visibility of distortion. Performance analysis is carried out to measure the improvement in CR in different cases such as:

- Lossless algorithm with symmetry and without symmetry.
- Visually lossless algorithm with symmetry and without symmetry.
- Visually lossless algorithm with symmetry and lossless algorithm without symmetry.

Bit rate is improved by 8.47 % on an average in the case of visually lossless compression algorithm (VLIC-3) with symmetry compared to lossless compression without symmetry. Also in the case of VLIC-3, average % reduction in bit per pixel is 6.29 compared to MILC method (Ait Aoudia *et al.* 2006).

In the fourth algorithm (VLIC-4), inter-slice, perceptual and statistical redundancies are identified and eliminated in wavelet transform domain. Wavelet based vision model suited for five levels of subband decomposition measures the perceptual redundancies and determines JND value. The performance of this wavelet based coder is compared with first three spatial based implementations. Wavelet based coder is found to perform better as it represents the image in more redundant form by decomposing image into different frequency levels. Wavelet based visually lossless coder (VLIC-4) reduces the bit rate by 20.66% compared with DPCM, 28.24% compared with HEVC (Sanchez and Bartrina-Rapesta 2014), 14.60% compared with JPEG2K, 13.28% compared with JPEG-LS and 46.85 % compared with JPEG3D (Bruylants *et al.* 2015). In all the above cases, both objective and subjective evaluations are found to be good.

The fifth implementation is VOI based medical image compression algorithm (VLIC-5). In this case, an automatic MRI brain tumor detection block is incorporated in the

compression algorithm. Fast symmetry based bounding box brain tumor segmentation technique is used to detect the region of a brain tumor in each image slice, considered as ROI. Wavelet based visually lossless algorithm is applied to ROI, and the remaining area is compressed with DCT based lossy compression technique. Here too, both subjective and objective evaluations are done. Based on radiologists opinion, it has been confirmed that there is no loss of diagnostically important information in the reconstructed image.

Developed all the five compression algorithms are compared in Table 6.1

Table 6.1: Comparison of developed medical image compression algorithms

Compression algorithm	Symmetric nature of medical image	Domain of Compression	HVS model is based on	Performance of algorithm (CR)
VLIC-1	Used	Spatial	Luminance adaptation	Low
VLIC-2	Used	Spatial	Luminance adaptation	High
VLIC-3	Used	Spatial	Luminance adaptation Texture masking	High
VLIC-4	Not used	Wavelet	Contrast sensitivity Luminance masking Contrast masking	Higher
VLIC-5	Not used	Wavelet and Cosine	Contrast sensitivity Luminance masking Contrast masking	Highest

6.2 FUTURE WORK

In the case of wavelet based visually lossless coder, only temporal and perceptual redundancies are considered. Symmetric nature retained in image slices are not considered. Study on the impact of symmetry present in medical images on the performance of wavelet based visually lossless compression algorithm can be carried out since it improves the performance of the compression algorithm. Also in wavelet based visually lossless coder, 2D DWT is used. Further analysis on the performance of coder with 3D DWT or hybrid wavelet transform can be explored.

REFERENCES

Acharya, R., **R. Wasserman**, **J. Stevens**, and **C. Hinojosa** (1995). "Biomedical imaging modalities: A tutorial". *Computerized Medical Imaging and Graphics*, **19**(1), 3–25.

Adams, M. D. and **R. Ward** (2001). "Wavelet transforms in the JPEG-2000 standard". *Proc. of IEEE Pacific Rim Conference on Communications, Computers and Signal Processing*, 160–163.

Ait Aoudia, S., **F. Z. Benhamida**, and **M. A. Yousfi** (2006). "Lossless compression of volumetric medical data". *Computer and Information Sciences*, 563–571.

A.J. Chandrasekhar, M. (2016). "Chest X-ray Atlas". `w.meddean.luc.edu/lumen/meded/medicine/pulmonar/cxr/atlas/cxratlas_f.htm`. (Accessed on May 2016).

Al-Ameen, Z. and **G. Sulong** (2015). "Deblurring computed tomography medical images using a novel amended landweber algorithm". *Interdisciplinary Sciences: Computational Life Sciences*, **7**, 319–325.

Ammari, H. (2008). "Biomedical imaging modalities". *An Introduction to Mathematics of Emerging Biomedical Imaging*, 3–13.

Amraee, S., **N. Karimi**, **S. Samavi**, and **S. Shirani** (2011). "Compression of 3D MRI images based on symmetry in prediction-error field". *IEEE International Conference on Multimedia and Expo*, 1–6.

Anastassopoulos, G. K. and **A. N. Skodras** (2002). "JPEG2000 ROI coding in medical imaging applications". *Proc. 2nd IASTED Int. Conf. on Visualisation, Imaging and Image Processing*, 783–788.

Ashton, E. A., **C. Takahashi**, **M. J. Berg**, **A. Goodman**, **S. Totterman**, and **S. Ekholm** (2003). "Accuracy and reproducibility of manual and semiautomated quantification of ms lesions by mri". *Journal of Magnetic Resonance Imaging*, 300–308.

Bilgin, A., **G. Zweig**, and **M. W. Marcellin** (1998). "Efficient lossless coding of medical image volumes using reversible integer wavelet transforms". *Data Compression Conference Proceedings*, 428–437.

Bruylants, T., **A. Munteanu**, and **P. Schelkens** (2015). "Wavelet based volumetric medical image compression". *Signal Processing: Image Communication*, **31**, 112–133.

Canadian Association of Radiologists (June 2008). "CAR Standards for irreversible compression in digital diagnostic imaging within radiology". `http://www.car.ca/uploads/standards%20guidelines/Standard_Lossy_Compression_EN.pdf`. (Accessed on May 2016).

Canny, J. (1986). "A computational approach to edge detection". *IEEE Transactions on Pattern Analysis and Machine Intelligence*, **6**, 679–698.

Chandler, D. M. and **S. S. Hemami** (2007). "VSNR: A wavelet-based visual signal-to-noise ratio for natural images". *IEEE Transactions on Image Processing,*, **16**(9), 2284–2298.

Chou, C.-H. and **Y.-C. Li** (1995). "A perceptually tuned subband image coder based on the measure of just-noticeable-distortion profile". *IEEE Transactions on Circuits and Systems for Video Technology*, **5**(6), 467–476.

Cover, T. M. and **J. A. Thomas**, *"Elements of information theory"*. John Wiley and Sons, 2012.

Czihó, A., **G. Cazuguel**, **B. Solaiman**, and **C. Roux** (1998). "Medical image compression using region-of-interest vector quantization". *Proceedings of the 20th Annual IEEE International Conference on Engineering in Medicine and Biology Society*, **3**, 1277–1280.

Dajun, W. and **T. Chong** (2000). "Lossless medical image compression algorithm exploring three dimensional space". *5th International Conference on Signal Processing Proceedings*, **2**, 1062–1064.

DICOM Library (2016). "Anonymize, share, view dicom files online". `http://www.dicomlibrary.com/dicom/study-structure/`. (Accessed on JUne 2016).

Ebrahimi Moghadam, A. and **P. Mohammadi** (2015). "Subjective and objective quality assessment of image: A survey". *Majlesi Journal of Electrcial Engineering*, **9**.

Engelke, U. and **H. J. Zepernick** (2007). "Perceptual-based quality metrics for image and video services: A survey". *3rd EuroNGI Conference on Next Generation Internet Networks*, 190–197.

European Society of Radiology (ESR and others) (2011). "Usability of irreversible image compression in radiological imaging. A position paper by the European Society of Radiology (ESR)". *Insights into Imaging*, **2**(2), 103.

Fletcher-Heath, L. M., **L. O. Hall**, **D. B. Goldgof**, and **F. R. Murtagh** (2001). "Automatic segmentation of non-enhancing brain tumors in magnetic resonance images". *Artificial intelligence in medicine*, 43–63.

Fukunaga, K., *"Introduction to statistical pattern recognition"*. Academic press, 2013.

Gaudeau, Y. and **J. Moureaux** (2009). "Lossy compression of volumetric medical images with 3D dead-zone lattice vector quantization". *Annals of Telecommunications*, **64**(5), 359–367.

Hanson, L. G. (2009). "Introduction to magnetic resonance imaging techniques", 1–48.

Hecht, M. (2008). "PACS: Picture Archiving and Communication System". *Vienna University of Technology, University of Paderborn*.

HP-LABS (2016). "LOCO-1/JPEG-LS home page:JPEG-LS reference encoder - V.1.00". `http://www.hpl.hp.com/loco`. (Accessed on May 2016).

Jain, A. K. (1989). "Fundamentals of digital image processing".

KAKADU (2016). "KAKADU Version 7.4 JPEG2000 software development tool kit". `http://kakadusoftware.com/`. (Accessed on May 2016).

Karsten, S. (2016). "H.264/AVC reference software". `http://iphome.hhi.de/suehring/tml/download/`. (Accessed on May 2016).

Kaus, M. R., **S. K. Warfield**, **A. Nabavi**, **P. M. Black**, **F. A. Jolesz**, and **R. Kikinis** (2001). "Automated segmentation of mr images of brain tumorses". *Radiology*, 586–591.

Klappenecker, A., **F. May**, and **T. Beth** (1998). "Lossless compression of 3D MRI and CT data". *Proc. SPIE, Wavelet Applications in Signal and Imaging Processing*, **3458**, 140–149.

Koff, D., **P. Bak**, **P. Brownrigg**, **D. Hosseinzadeh**, **A. Khademi**, **A. Kiss**, **L. Lepanto**, **T. Michalak**, **H. Shulman**, and **A. Volkening** (2009). "Pan-canadian evaluation of irreversible compression ratios (lossy compression) for development of national guidelines". *Journal of Digital Imaging*, **22**(6), 569–578.

Kowalik-Urbaniak, I., **D. Brunet**, **J. Wang**, **D. Koff**, **N. Smolarski-Koff**, **E. R. Vrscay**, **B. Wallace**, and **Z. Wang** (2014). "The quest for'diagnostically lossless' medical image compression: A comparative study of objective quality metrics for compressed medical images". *SPIE Medical Imaging*, 903717–903717.

Kowalik-Urbaniak, I. A., **J. Castelli**, **N. Hemmati**, **D. Koff**, **N. Smolarski-Koff**, **E. R. Vrscay**, **J. Wang**, and **Z. Wang** (2015). "Modelling of subjective radiological assessments with objective image quality measures of brain and body CT images". *Image Analysis and Recognition*, 3–13.

Lee, H., **Y. Kim**, **A. Rowberg**, and **E. Riskin** (1993). "Statistical distributions of DCT coefficients and their application to an interframe compression algorithm for 3D medical images". *IEEE Transactions on Medical Imaging,*, **12**(3), 478–485.

Lin, W. and **C.-C. J. Kuo** (2011). "Perceptual visual quality metrics: A survey". *Journal of Visual Communication and Image Representation*, **22**(4), 297–312.

Liu, Z., **L. J. Karam**, and **A. B. Watson** (2006). "JPEG 2000 encoding with perceptual distortion control". *IEEE Transactions on Image Processing,*, **15**(7), 1763–1778.

Loose, R., **R. Braunschweig**, **E. Kotter**, **P. Mildenberger**, **R. Simmler**, and **M. Wucherer** (2009). "Compression of digital images in radiology results of a consensus conference". *RoFo: Fortschritte auf dem Gebiete der Rontgenstrahlen und der Nuklearmedizin*, **181**(1), 32–37.

Lowe, D. G. (2004). "Distinctive image features from scale-invariant keypoints". *International Journal of Computer Vision*, **60**(2), 91–110.

Loy, G. and **J.-O. Eklundh** (2006). "Detecting symmetry and symmetric constellations of features". *Computer Vision*, 508–521.

Menegaz, G. and **J. Thiran** (2002). "Lossy to lossless object-based coding of 3D MRI data". *IEEE Transactions on Image Processing,*, **11**(9), 1053–1061.

Menegaz, G. and **J. Thiran** (2003). "Three-dimensional encoding/two-dimensional decoding of medical data". *IEEE Transactions on Medical Imaging,*, **22**(3), 424–440.

Mustra, M., **K. Delac**, and **M. Grgic** (2008). "Overview of the DICOM standard". *50th International Symposium ELMAR*, **1**, 39–44.

Nadenau, M. J., **S. Winkler**, **D. Alleysson**, and **M. Kunt** (2000). "Human vision models for perceptually optimized image processing–A review". *Proceedings of the IEEE*, 32.

Nait-Ali, A. and **C. Cavaro-Menard**, *"Compression of biomedical images and signals"*. John Wiley & Sons, 2008.

Nosratinia, A., **N. Mohsenian**, **M. Orchard**, and **B. Liu** (1996). "Interframe coding of magnetic resonance images". *IEEE Transactions on Medical Imaging*, **15**(5), 639–647.

NPS MedicineWise (2016). "Comparing different types of imaging". `http://www.nps.org.au/medical-tests/medical-imaging/for-individuals/imaging-compared`. (Accessed on June 2016).

OECD (2016). OECD data (2016)"Health care use". `https://data.oecd.org/health.htm#profile-Health%20equipment`. (Accessed on May 2016).

OPEN-JPEG (2016). "Openjpeg, open source c-libary for jpeg 2000". `https://code.google.com/p/openjpeg/wiki/Downloads?tm=2`. (Accessed on May 2016).

OPEN-JPEG-3D (2016). "Openjpeg, open source C-libary for JPEG 3D". `https://code.google.com/p/openjpeg/downloads/detail?name=openjpeg3d_v1_3.tar.gz&can=4&q=`. (Accessed on May 2016).

Pizzolante, R. and **B. Carpentieri** (2013). "Lossless, low-complexity, compression of three-dimensional volumetric medical images via linear prediction". *18th International Conference on Digital Signal Processing*, 1–6.

Radke, R. J., **S. Andra**, **O. Al-Kofahi**, and **B. Roysam** (2005). "Image change detection algorithms: A systematic survey". *IEEE Transactions on Image Processing*, **14**(3), 294–307.

Ramaswamy, A. and **W. Mikhael** (1996). "A mixed transform approach for efficient compression of medical images". *IEEE Transactions on Medical Imaging,*, **15**(3), 343–352.

Razaak, M., **M. G. Martini**, and **K. Savino** (2014). "A study on quality assessment for medical ultrasound video compressed via HEVC". *IEEE Journal of Biomedical and Health Informatics,*, **18**, 1552–1559.

Rontgen, W. C. (1896). "On a new kind of rays". *Science*, 227–231.

Royal College of Radiologists (2016). "The adoption of lossy data compression for the purpose of clinical interpretation". `https://www.rcr.ac.uk/sites/default/files/docs/radiology/pdf/IT_guidance_LossyApr08.pdf`. (Accessed on June 2016).

Safranek, R. J. and **J. D. Johnston** (1989). "A perceptually tuned sub-band image coder with image dependent quantization and post-quantization data compression", 1945–1948.

Saha, B. N., **N. Ray**, **R. Greiner**, **A. Murtha**, and **H. Zhang** (2012). "Quick detection of brain tumors and edemas: A bounding box method using symmetry". *Computerized Medical Imaging and Graphics*, **36**(2), 95–107.

Salomon, D., *"Data compression: The Complete Reference"*. Springer-Verlag New York Inc, 2007.

Sanchez, V., **R. Abugharbieh**, and **P. Nasiopoulos** (2009*a*). "3D scalable lossless compression of medical images based on global and local symmetries". *16th IEEE International Conference on Image Processing*, 2525–2528.

Sanchez, V., **R. Abugharbieh**, and **P. Nasiopoulos** (2009*b*). "Symmetry-based scalable lossless compression of 3D medical image data". *IEEE Transactions on Medical Imaging*, **28**(7), 1062–1072.

Sanchez, V., **R. Abugharbieh**, and **P. Nasiopoulos** (2010). "3D scalable medical image compression with optimized volume of interest coding". *IEEE Transactions on Medical Imaging*, **29**(10), 1808–1820.

Sanchez, V. and **J. Bartrina-Rapesta** (2014). "Lossless compression of medical images based on HEVC intra coding". *IEEE International Conference on Acoustics, Speech and Signal Processing*, 6622–6626.

Sanchez, V. and **P. Nasiopoulos** (2011). "3D medical image coding with optimal channel protection for wireless transmission". *IEEE International Conference on Acoustics, Speech and Signal Processing*, 561–564.

Sanchez, V., **P. Nasiopoulos**, and **R. Abugharbieh** (2006). "Lossless compression of 4D medical images using H.264/AVC". *IEEE International Conference on Acoustics, Speech and Signal Processing*, **2**, 1116–1119.

Schelkens, P., **A. Munteanu**, **J. Barbarien**, **M. Galca**, **X. Giro-Nieto**, and **J. Cornelis** (2003). "Wavelet coding of volumetric medical datasets". *IEEE Transactions on Medical Imaging*, **22**(3), 441–458.

Shapiro, J. M. (1993). "Embedded image coding using zerotrees of wavelet coefficients". *IEEE Transactions on signal processing*, **41**(12), 3445–3462.

Sheikh, H. R. and **A. C. Bovik** (2006). "Image information and visual quality". *IEEE Transactions on Image Processing*, **15**(2), 430–444.

Srikanth, R. and **A. Ramakrishnan** (2005). "Contextual encoding in uniform and adaptive mesh-based lossless compression of MR images". *IEEE Transactions on Medical Imaging*, **24**(9), 1199–1206.

Strom, J. and **P. C. Cosman** (1997). "Medical image compression with lossless regions of interest". *Signal processing*, **59**(2), 155–171.

Taquet, J. and **C. Labit** (2012). "Hierarchical oriented predictions for resolution scalable lossless and near-lossless compression of CT and MRI biomedical images". *IEEE Transactions on Image Processing,*, **21**(5), 2641–2652.

Thirumalai, V. and **R. Kanhirodan** (2006). "Image coding of 3D volume using wavelet transform for fast retrieval of 2D images". *IEEE proceedings on Vision Image and Signal Processing*, **153**, 507–511.

Tzannes, A. (2003). "Compression of 3-dimensional medical image data using part 2 of JPEG 2000". *Aware. Inc, Nov*.

Villasenor, J. D., **B. Belzer**, and **J. Liao** (1995). "Wavelet filter evaluation for image compression". *IEEE Transactions on Image Processing*, **4**(8), 1053–1060.

Wallace, G. K. (1992). "The JPEG still picture compression standard". *IEEE Transactions on Consumer Electronics*, **38**(1), 18–34.

Wang, Z. and **A. Bovik** (2009). "Mean squared error: love it or leave it? A new look at signal fidelity measures". *IEEE Signal Processing Magazine*, **26**(1), 98–117.

Wang, Z., **A. C. Bovik**, **H. R. Sheikh**, and **E. P. Simoncelli** (2004). "Image quality assessment: From error visibility to structural similarity". *IEEE Transactions on Image Processing*, **13**(4), 600–612.

Watson, A. B., **G. Y. Yang**, **J. Solomon**, **J. Villasenor**, *et al.* (1997). "Visibility of wavelet quantization noise". *IEEE Transactions on Image Processing*, **6**(8), 1164–1175.

Weinherger, M., **G. Semussi**, and **G. Sapiro** (2000). "The LOCO-1 lossless image compression algorithm: Principles and standardization into JPEG-LS". *IEEE Trans Image Proess*, **9**(8), 1309–1324.

Wong, S., **L. Zaremba**, **D. Gooden**, and **H. Huang** (1995). "Radiologic image compression-A review". *Proceedings of the IEEE*, **83**(2), 194–219.

Wu, D., **D. Tan**, **M. Baird**, **J. DeCampo**, **C. White**, and **H. Wu** (2006). "Perceptually lossless medical image coding". *IEEE Transactions on Medical Imaging*, **25**(3), 335–344.

Wu, X. and **N. Memon** (1996). "CALIC-A context based adaptive lossless image codec". *IEEE International Conference on Acoustics, Speech, and Signal Processing*, **4**, 1890–1893.

Xiong, Z., **X. Wu**, **S. Cheng**, and **J. Hua** (2003). "Lossy-to-lossless compression of medical volumetric data using three-dimensional integer wavelet transforms". *IEEE Transactions on Medical Imaging*, **22**(3), 459–470.

Xu, C. and **J. L. Prince** (1998). "Snakes, shapes, and gradient vector flow". *IEEE Transactions on Image Processing*, **7**(3), 359–369.

Yang, X., **W. Ling**, **Z. Lu**, **E. P. Ong**, and **S. Yao** (2005). "Just noticeable distortion model and its applications in video coding". *Signal Processing: Image Communication*, **20**(7), 662–680.

Yodchanan, W. (2008). "Lossless compression for 3-D MRI data using reversible KLT". *International Conference on Audio, Language and Image Processing*, 1560–1564.

LIST OF PAPERS BASED ON THESIS

Journal Papers:

1. Chandrika B.K., Aparna P. & Sumam David S., "Analysis and Comparison of Symmetry based Lossless and Perceptually Lossless Algorithms for Volumetric Compression of Medical Images ", *Journal of Medical Informatics and Technologies*, 2015, Vol. 24, pp 147-154, ISSN 1642-6037.

2. Chandrika B.K., Aparna P., Sumam David S., "Visually Lossless Coder for Volumetric MRI and CT Image Data using Wavelet Transform ", *International Journal of Computational Vision and Robotics, Inderscience Publishers*, (In press).

3. Chandrika B.K., Aparna P., Sumam David S., "Perceptually Lossless Coder for Three Dimensional MRI and CT Image Data ", *Journal of Visual Communication and Image Representation, Elsevier*, (Revised manuscript communicated on 2^{nd} January, 2017).

4. Chandrika B.K., Aparna P., Sumam David S., "A Novel Approach to Diagnostically Lossless compression of Volumetric Medical Data Based on Wavelet and Just-Noticeable-Distortion Model ", *IEEE Transactions on Medical Imaging*, **(Communicated)**.

Conference Papers:

1. Chandrika B.K., Aparna P., Sumam David S., "Symmetry Based Perceptually Lossless Compression of 3D Medical Images in Spatial Domain", *IEEE International conference on Computer, Communication and Control Technology-I4CT 2014*, Langkawi, Malaysia, pp 53-57, September 2-4, 2014, doi: 10.1109/I4CT.2014.6914144.

2. Chandrika B.K., Aparna P., Sumam David S, "Irreversible wavelet compression of radiological images based on visual threshold", *IEEE International Women in Engineering conference on Electrical and Computer Engineering 2015, Dhaka, Bangladesh*, pp 280-283, December 19-20, 2015, doi:10.1109/WIECON-ECE.2015.7443918. **(Best paper of the track in IEEE WIECON. Track name: Multimedia and signal processing)**.

CURRICULUM VITAE

Chandrika B. K.

Assistant Professor,

Department of Electrical and Electronics Engineering

Manipal Institute of Technology, Manipal, Manipal University, India-576104

Email: chandribk@gmail.com, chandrika.bk@manipal.edu

Teaching Experience: 15 Years

Academic records:

1. M.Tech (Industrial Electronics) from Department of Electronics and Communication Engineering, National Institute of Technology Karnataka, Surathkal in July 2000.
2. B.E (Electrical and Electronics Engineering) from National Institute of Technology Karnataka, Surathkal in July 1994

Research Interests:

Digital Signal Processing, FPGA based system design.

Publications:

No.of Journal Publications: 02

No.of International Conference Proceedings / Publications: 02

No.of National Conference Proceedings / Publications: 02.